

HARMONIC GENERATION IN REFLECTION FROM PLASMA MIRRORS

NICHOLAS MAURICE FASANO

A DISSERTATION
PRESENTED TO THE FACULTY
OF PRINCETON UNIVERSITY
IN CANDIDACY FOR THE DEGREE
OF DOCTOR OF PHILOSOPHY

RECOMMENDED FOR ACCEPTANCE BY
THE DEPARTMENT OF
MECHANICAL AND AEROSPACE ENGINEERING

ADVISER: PROFESSOR JULIA M. MIKHAILOVA

May 2023

© Copyright by Nicholas Maurice Fasano, 2023. All rights reserved.

Abstract

The discovery of chirped-pulse amplification in 1985 has led to the development of powerful femtosecond lasers reaching the terawatt and petawatt levels. These lasers can produce intensities capable of ionizing any gas, liquid, or solid target, including the conventional optics that control ordinary light. This rapid increase in the intensity of lasers has prompted researchers to build plasma-based optics capable of handling light of ionizing intensities, including plasma mirrors, waveplates, q-plates, beam combiners and splitters, amplifiers, lenses, and gratings. The plasma mirror, in particular, has a broad range of applications, such as specular reflection and focusing, temporal and spatial cleaning, and generating harmonic orders of the driving laser's fundamental wavelength. This thesis presents experimental and computational modeling of intense lasers interacting with plasma mirrors, focusing on the emission of harmonics driven by lasers with tailored temporal waveforms and controlled polarization states. In addition to enabling harmonic generation with favorable temporal, spatial, and spectral properties, this work shows how manipulating light in all degrees of freedom allows for experimental control of relativistic plasma dynamics at the sub-optical-cycle timescale.

Specifically, this thesis provides the first experimental demonstration of enhanced harmonic generation with a two-color laser compared to a single color alone from a multi-pass plasma mirror configuration. Additionally, a series of numerical studies using tailored light and structured plasmas is presented, revealing the emission of vortex harmonics in the specular and transmitted direction from a circularly polarized laser normally incident on an ultrathin plasma target, as well as an ellipticity-controlled harmonic source where the harmonic orders either co-rotate or counter-rotate with the reflected funda-

mental. Finally, this thesis identifies several numerical artifacts that arise when modeling high-density laser–solid interactions within the particle-in-cell framework, especially the appearance of single-cell density spikes that grow with increasing spatial resolution.

Acknowledgements

I want to thank several people who have made the work presented in this dissertation possible.

First and foremost, I thank my advisor, Professor Julia Mikhailova, for her guidance, support, and encouragement during my graduate studies. Throughout my time at Princeton, Professor Mikhailova provided me with essential feedback and direction on my thesis work, and her commitment to excellence in research was genuinely inspiring. I am honored to have had the opportunity to work in her lab.

I also owe a huge debt of gratitude to Matthew Edwards. It is safe to say that the results presented in this dissertation would not have been possible without him. From the very beginning of my graduate studies, he was always available to answer my countless questions with exceptional clarity and grace. I am incredibly grateful for his efforts in helping me overcome the many obstacles I encountered.

I also want to thank the other members of the ETOILES group, including Tim Bennet, Andreas Giakas, Vedin Dewan, Anatoli Morozov, Alec Griffith, Jesse Griff-McMahon, Isabelle Tigges-Green, and Ava Hejazi. I appreciate your hard work and several helpful suggestions during our group meetings.

I thank my PhD committee and thesis readers, Dr. Mikhail Shneider and Professor Michael Littman, for providing guidance and several stimulating discussions on my research progress. I thank Professor Nathaniel Fisch and Professor Aditya Sood for agreeing to be the FPO examiners. I also thank the rest of the MAE faculty and staff that I have had the pleasure to work with, including Theresea Russo, Katerina Zara, Jill Ray, Tina Ollwerther, Sharon McCann, Lamyaa El-Gabry, Glenn Northey, Daniel Nosenchuck, and

Luigi Martinelli.

I would also like to thank my family, Michael, Laurie, Michael, Christopher, and Danielle, for all their love and support during these last six years and the many relaxing weekends together. It was always nice knowing that the comforts of home were just a short train ride away.

Finally, I want to thank my girlfriend, Liz, whose emotional support, patience, and unwavering understanding have made graduate school manageable. Our nightly FaceTime calls and your weekend visits have always provided me with a much-needed respite from the rigors of graduate school. You have been my rock, my partner, and my best friend, and I know that I could not have achieved what I have without you.

* * *

I am grateful for the funding provided by the Program in Plasma Science and Technology (PPST). Much of the work presented in this thesis was supported by the National Science Foundation under Grant No. PHY 1806911 and the Department of Energy under grant No. DE-SC0017907. The simulations for this work were performed using the High Performance Computing Center at Princeton University. The EPOCH code was developed as part of the UK EPSRC 300 360 funded project EP/G054940/1.

This dissertation carries T#3446 in the records of the Department of Mechanical and Aerospace Engineering.

Contents

| | |
|--|-----------|
| Abstract | 3 |
| Acknowledgements | 5 |
| List of Figures | 9 |
| List of Publications | 17 |
| 1 Introduction | 19 |
| 1.1 An overview of plasma-based optics | 19 |
| 1.2 Secondary radiation from plasma mirrors | 21 |
| 1.3 Outline of this thesis | 23 |
| 1.3.1 Significant results | 24 |
| 2 Modeling of Laser-Plasma Interactions: On Density Artifacts, Collisions, and Numerical Dispersion in Particle-In-Cell Simulations | 27 |
| 2.1 Introduction | 27 |
| 2.1.1 Single electron exposed to a plane wave | 28 |
| 2.1.2 Particle-in-cell simulations | 33 |
| 2.2 Using particle-in-cell simulations for modeling relativistic harmonic generation | 35 |
| 2.2.1 Space and time discretization - numerical dispersion | 36 |
| 2.2.2 Attosecond electron bunch dynamics | 41 |
| 2.2.3 Resolution-dependent spikes of the electron density | 48 |
| 2.3 Effects of collisions on electron bunch dynamics and attosecond pulse intensity | 52 |

| | |
|--|-----------|
| 3 Plasma Optics for Ultra Intense Laser Applications | 58 |
| 3.1 Introduction | 58 |
| 3.2 Plasma mirrors for reflection and temporal contrast improvement | 59 |
| 3.2.1 Experimental set-up | 59 |
| 3.2.2 Contrast and reflectivity measurements | 61 |
| 3.2.3 Pulse envelope measurements with GRENOUILLE | 63 |
| 3.3 Plasma gratings for diffraction and temporal contrast improvement | 67 |
| 3.3.1 Experimental set-up | 68 |
| 3.3.2 Diffraction and grating stability | 69 |
| 3.3.3 Contrast and pulse envelope measurements | 70 |
| 4 A Cascaded Plasma Mirror Configuration for Enhanced Harmonic Generation | 74 |
| 4.1 Introduction | 74 |
| 4.2 Experimental set-up of a cascaded plasma mirror configuration | 76 |
| 4.3 Plasma mirror for synthesizing a terawatt two-color laser | 76 |
| 4.4 Waveform engineering for enhanced harmonic generation and sub-cycle control of electron density dynamics | 82 |
| 5 Harmonic Generation with Structured Lasers | 93 |
| 5.1 Introduction | 93 |
| 5.2 Ultrathin foil targets | 94 |
| 5.2.1 P-polarized interactions and the importance of the electron bunch width on harmonic efficiency | 94 |
| 5.2.2 Circularly polarized interactions and the emission of vortex harmonic orders | 98 |
| 5.3 Attosecond pulse interference and harmonic structure | 112 |
| 5.4 Elliptically polarized incident lasers and the emission of co- and counter-rotating harmonics | 119 |

| | |
|--|------------|
| 6 Conclusion | 129 |
| 6.1 Summary of this thesis | 129 |
| 6.2 Future work | 131 |
| References | 131 |
| A List of Abbreviations | 147 |
| B List of Symbols | 149 |
| C Coordinate Frames Used in Simulations | 152 |
| D Dispersion Calculations for a Two-Color Laser Propagating Through Glass | 155 |

List of Figures

| | | |
|------|---|----|
| 2.1 | Dynamics of a single electron exposed to a plane wave in vacuum. | 30 |
| 2.2 | Dynamics of a single electron exposed to a plane wave in vacuum including the effects of a restoring force. | 31 |
| 2.3 | A schematic diagram of the particle-in-cell algorithm | 34 |
| 2.4 | Spectrograms of the reflected electric field from PIC simulations for $C = \{0.53, 0.95\}$ and $\lambda_L/\Delta x = \{1500, 4000\}$ | 37 |
| 2.5 | Effects of spatial resolution on the attosecond pulse temporal profile for the parameters $\theta = 0^\circ$, $a_0 = 40$, $N_0 = 200$, varied $\lambda_L/\Delta x$, particles/cell = 100, and $C = 0.95$ | 38 |
| 2.6 | Analytic spectrograms calculated from the numerical dispersion equation given by the Yee scheme. | 39 |
| 2.7 | Numerical error in PIC simulations as a result of choosing a CFL number close to the stability limit ($C = 1$). | 40 |
| 2.8 | Effects of the number of particles-per-cell on the numerical error resulting from choosing the CFL number close to the stability limit. | 42 |
| 2.9 | Attosecond pulse emission and sub-cycle density dynamics of relativistic electron bunches near the surface of a plasma mirror from PIC simulations. | 44 |
| 2.10 | Dynamics of selected electrons leading up the emission of the attosecond pulse. | 45 |
| 2.11 | Spatial distributions of the electron number density (N_e) illustrating the electron bunch evolution from the time when the electron bunch has its maximum displacement from the initial plasma-vacuum interface. | 47 |

| | |
|--|----|
| 2.12 Effects of spatial resolution on the density distribution of the electron bunch modeled with and without collisions | 49 |
| 2.13 Peak density of the emitting electron bunch as a function of spatial resolution for simulations with collisions and without collisions | 50 |
| 2.14 Effects of spatial resolution on the reflected spectra and attosecond pulse temporal profile. | 52 |
| 2.15 Attosecond pulse generation efficiency (η_{atto}) simulated with and without collisions in the frequency range $80 < \omega/\omega_L < 300$ as a function of a_0/N_0 for three different initial plasma densities. | 53 |
| 2.16 Spectral efficiency (η_{spec}) simulated with and without collisions in the frequency range $120 < \omega/\omega_L < 200$ as a function of a_0/N_0 for a finite pre-plasma gradient scale length. | 54 |
| 2.17 Comparison of RHHG simulations with and without collisions for the parameters $\theta = 30^\circ$, varied a_0 , $N_0 = 500$, $\lambda_L/\Delta x = 8000$, particles/cell = 150, and $C = 0.95$ | 55 |
| 2.18 Comparison of the distribution of Lorentz factors for emitting electrons within the electron bunch for simulations with and without collisions . . | 56 |
| 3.1 Schematic set-up of a plasma mirror used to temporally clean the picosecond contrast of the laser. | 60 |
| 3.2 Measured beam profiles on the surface of PM1 as a function of the target position. | 60 |
| 3.3 Temporal contrast measurement of the laser on a picosecond timescale taken before and after reflection from the contrast cleaning plasma mirror (PM1). | 61 |
| 3.4 Reflectivity from PM1 as a function of z at fixed energy and as a function of energy at fixed z | 62 |
| 3.5 Measured spatial profiles of the beam after reflection from PM1. Measured spatial profiles of the beam after reflection from PM1 as the plasma mirror is scanned through the focus. | 63 |

| | | |
|------|--|----|
| 3.6 | Pulse duration measurement of the compressed laser entering the experimental chamber using a home-built GRENOUILLE apparatus | 65 |
| 3.7 | Recovered GRENOUILLE trace of the laser after about 1m of propagation through 2mbar of Helium gas, which induces some spectral modulation and broadening. | 66 |
| 3.8 | Pulse duration measurement of the laser after propagating through the experimental chamber along the beam diagnostics line with PM1 engaged | 66 |
| 3.9 | Pulse duration measurement of the laser after propagating through the experimental chamber along the beam diagnostics line with PM1 engaged | 67 |
| 3.10 | Reflection efficiency and pulse duration as a function of PM1z for two different incident energies from the contrast cleaning plasma mirror. . . . | 68 |
| 3.11 | Schematic diagram of a plasma grating experiment. | 69 |
| 3.12 | Normalized diffraction signal as a function of the probe delay with respect to the formation of the plasma grating. | 70 |
| 3.13 | Single-shot diffraction efficiency (normalized) recorded for over 60 minutes. | 71 |
| 3.14 | Contrast measurement of the incident (blue) and diffracted (red) laser showing that the diffracted beam improved the temporal contrast by at least a factor of 3×10^5 | 72 |
| 3.15 | Pulse duration measurement of the incident probe beam. | 72 |
| 3.16 | Pulse duration measurement of the diffracted probe beam. | 73 |
| 4.1 | Experimental set-up of the multi-pass plasma mirror configuration, showing the interaction geometries for all three plasma mirrors as well as the diagnostics for measuring the reflected harmonics. | 77 |
| 4.2 | Measured beam profile incident on the surface of PM2 as a function of z . Second harmonic reflectivity as PM2 is scanned through the focus with an incident laser energy of 60mJ. | 79 |
| 4.3 | Lineouts of the reflected fundamental and second harmonic spatial profile from PM2 for an in-focus interaction ($z = 0$) and an out-of-focus interaction ($z = 100\mu\text{m}$). | 79 |

| | | |
|------|--|----|
| 4.4 | Measured near field and far field profiles of the reflected fundamental and second harmonic from PM2 taken when the plasma mirror was at the laser's best focus. | 80 |
| 4.5 | Spatial profiles of the direct beam, the beam after PM1, and the beam after PM1 and PM2, illustrating the spatial cleaning effect of plasma mirrors in the sub-relativistic and relativistic regimes. | 81 |
| 4.6 | Near-field spatial profiles, vertical lineouts of the spatial profiles at $x = 0\text{mm}$, and the reflected visible spectrum of the reflected fundamental and second through fourth harmonic orders taken after PM3 | 83 |
| 4.7 | Third and fourth harmonic energy as a function of on-target intensity for one-color and two-color interactions. | 84 |
| 4.8 | Reflected fundamental, second harmonic, and third harmonic energy for both one-color and two-color interactions as a function of on-target intensity. | 86 |
| 4.9 | Third harmonic energy for one-color and two-color interactions plotted as a function of GDD, which was controlled using an acousto-optic modulator. | 87 |
| 4.10 | Reflected fields and particle trajectories extracted from one-dimensional particle-in-cell simulations of one and two-color interactions. | 88 |
| 4.11 | Evolution of the electron bunches from a time when the electron bunch is at its maximum displacement from the initial vacuum-plasma interface through the time of attosecond pulse emission. | 88 |
| 4.12 | Third harmonic energy as a function of PM3's target position, z , with respect to the incident laser's best focus | 90 |
| 4.13 | Propagation effects on the intensity and phase for a Gaussian laser beam evolving according to the paraxial equation. | 90 |
| 4.14 | Spatial profiles of the third harmonic and measured on target profile of the incident laser for both in-focus and out-of-focus interactions | 91 |
| 5.1 | Spectral efficiency of the reflected and transmitted radiation for various plasma thicknesses and laser amplitudes. | 95 |

| | | |
|------|---|-----|
| 5.2 | The dynamics of the emitting electrons within the electron bunch and the fields they emit when an intense laser interacts with an ultrathin foil. | 96 |
| 5.3 | Reconstruction of the total reflected spectrum by progressively incorporating more electrons from the leading edge of the electron bunch | 97 |
| 5.4 | The emitting electron bunch and reflected spectra for both an ultrathin foil and a semi-infinite target. | 98 |
| 5.5 | A schematic diagram of the proposed geometry for generating high-power ultraviolet and extreme ultraviolet vortex beams | 101 |
| 5.6 | One-dimensional PIC simulation of harmonic generation from an ultrathin foil irradiated at normal incidence by a circularly polarized laser and a linearly polarized laser. | 101 |
| 5.7 | Three dimensional PIC simulations presenting the electron density evolution when a circularly polarized laser interacts with an ultrathin foil. | 103 |
| 5.8 | 3D PIC results of the reflected and transmitted harmonic radiation when a circularly polarized laser interacts with an ultrathin foil. | 103 |
| 5.9 | The evolution of the electron number density and the longitudinal electron current density in the transverse plane when a circularly polarized laser is normally incident on an ultrathin foil | 104 |
| 5.10 | Third harmonic efficiency in the transmitted and reflected direction as a function of ND/a_0 | 107 |
| 5.11 | Two dimensional PIC simulations of the third harmonic efficiency in the (a) transmitted and (b) reflected directions as a function of τ/T_L for a circularly polarized laser normally incident on an ultrathin foil. | 108 |
| 5.12 | Spectral lineout plot from a 2D PIC simulation with parameters $N = 100$, $a_o = 80$, and $D = 0.18$ | 108 |
| 5.13 | Second harmonic intensity summed along the propagation axis for four different angles of incidences. | 110 |

| | |
|---|-----|
| 5.14 The transverse laser profile of the emitted second harmonic for various polarization states of a relativistically intense laser normally incident on an ultrathin foil. | 111 |
| 5.15 Variation in emission timing of attosecond pulses for a multi cycle driving laser and varied laser amplitude. | 113 |
| 5.16 Illustration of harmonic broadening as a result of non periodic emission timing between attosecond pulses. | 115 |
| 5.17 Effect of chirped driving lasers on the harmonic width and the harmonic intensity. | 116 |
| 5.18 Comparison of the reflected spectrum for the cases of an unchirped and negatively chirped incident laser | 117 |
| 5.19 Broadening of harmonic orders as a function of the pre-plasma gradient length scale. | 117 |
| 5.20 The appearance of half integer harmonics as a result of attosecond pulses with spacing at twice the incident laser's period. | 118 |
| 5.21 Two-dimensional particle-in-cell simulations characterizing the polarization state of the reflected harmonics as a function of the fraction of energy contained in the S-polarized component of the driving laser, I_s/I_L | 122 |
| 5.22 One-dimensional particle-in-cell simulation of the attosecond pulse train, space-time electron number density contours, and the electron current density at the front surface of the electron number density for $I_s/I_L = 1.0$, 0.99, and 0.50. | 123 |
| 5.23 Attosecond pulse efficiency and attosecond pulse ellipticity in the spectral range $10 < \omega/\omega_L < 60$ as a function of the phase difference between the S and P-polarized components of the incident laser, ϕ_{sp} , for different values of I_s/I_L | 125 |
| 5.24 One-dimensional particle-in-cell simulations of attosecond pulse efficiency and ellipticity as a function of I_s/I_L for different values of a_0/N | 126 |

| | |
|---|-----|
| 5.25 One-dimensional particle-in-cell simulations of the ellipticity and reflected energy contained in the fundamental and second harmonic as a function of a_0/N for different values of I_s/I_L . | 127 |
| 6.1 Proposed changes to the experimental set-up of the multi-pass plasma mirror configuration to include elliptically polarized driving lasers. | 132 |
| C.1 Common coordinate systems used throughout this thesis to model laser-solid interactions. | 153 |
| D.1 Geometry of the fused silica wafer used to control the waveform of the two-color laser after PM2. | 157 |
| D.2 Calculated relative phase delay and relative group delay between the fundamental and second harmonic as a function of the wafer angle. | 157 |

List of Publications

This dissertation presents work from the following list of published articles and conference proceedings. Manuscripts that are under review or in preparation at the time of this dissertation's publication are indicated.

Published Manuscripts and Conference Proceedings

1. **N. M. Fasano**, M. R. Edwards, and J. M. Mikhailova, *Electron bunch dynamics and emission in particle-in-cell simulations of relativistic laser-solid interactions: on density artifacts, collisions, and numerical dispersions*, Under Review.
2. **N. M. Fasano**, M. R. Edwards, V. Dewan, A. Giakas, and J. M. Mikhailova, *Enhanced relativistic harmonic generation using plasma-mirror-shaped laser waveforms*, to be submitted.
3. **N. M. Fasano** and J. M. Mikhailova, *High-power ultraviolet vortex beams generated from a relativistic laser interacting with an ultrathin foil*, CLEO: QELS Fundamental Science. Optica Publishing Group, (2021).
4. **N. M. Fasano**, M. R. Edwards, J. M. Mikhailova, *Effects of electron bunch width on the efficiency of high-order harmonic generation from ultrathin solid targets*, CLEO: QELS Fundamental Science. Optica Publishing Group, (2020).
5. M. R. Edwards, **N. M. Fasano**, T. Bennett, A. Griffith, N. Turley, B. M. O'Brien, and J. M. Mikhailova, *A multi-terawatt two-color beam for high-power field-controlled nonlinear optics*, Optics Letters **45**, 6542 (2020).
6. M. R. Edwards, **N. M. Fasano**, and J. M. Mikhailova, *Electron-nanobunch-width-dominated spectral power law for relativistic harmonic generation from ultrathin foils*, Physical Review Letters **124**, 185004 (2020).
7. **N. M. Fasano**, M. R. Edwards, J. M. Mikhailova, *Modeling the formation of nanometer-scale high-density electron bunches in relativistic laser-solid interaction: effects of numerical resolution*, Frontiers in Optics, (2018).
8. **N. M. Fasano** and J. M. Mikhailova, *Plasma mirrors for generating co- and counter-rotating harmonics*, In preparation.
9. M. R. Edwards, **N. M. Fasano**, et al., *Greater than five-order-of-magnitude post-compression temporal contrast improvement with an ionization plasma grating*, In preparation.

Conference Presentations

1. **N. M. Fasano**, M. R. Edwards, A. Giakas, A. Morozov, T. Bennett, J. M. Mikhailova. *Low-order harmonics emitted from relativistic plasma mirrors driven by two-color and elliptically polarized lasers*, APS DPP meeting, Bulletin of the American Physical Society, (2021). Oral.
2. **N. M. Fasano**, M. R. Edwards, and J. M. Mikhailova, *Particle-in-cell simulations of harmonic generation from relativistic plasma mirrors: effects of collisions on the emitting electron bunch width*, APS DPP meeting, Bulletin of the American Physical Society, (2020). Oral.
3. **N. M. Fasano** and J. M. Mikhailova, *Numerical Modeling of relativistic harmonic structure from plasma mirrors: insights into relativistic plasma dynamics*, APS DPP meeting, Bulletin of the American Physical Society, (2020). Poster.
4. **N. M. Fasano**, M. R. Edwards, J. M. Mikhailova, *Sub-optical-cycle dynamics of electron nano-bunches in relativistic laser-plasma interactions: insights from numerical simulations*, APS DPP meeting, Bulletin of the American Physical Society, (2018). Poster.

Chapter 1

Introduction

1.1 An overview of plasma-based optics

In the last 40 years the peak power of ultrafast lasers have been improved by more than six orders of magnitude (from Gigawatt to Petawatt [1]). Today, multi-petawatt lasers are currently in operation and systems with up to 100PW peak powers are under construction. This dramatic rise in peak power was made possible by chirped-pulse amplification [2], a discovery which was awarded the 2018 Nobel prize in physics. To meet the unique demands of high-power, ultrafast light-matter experiments the manufacturing of conventional solid-state optics, including mirrors, lenses, gratings, waveplates, and crystals, have advanced considerably in recent decades. For example, specialized dielectric coatings for mirrors are routinely available to researchers which can reflect broadband light (e.g. 720nm-900nm) with greater than 99% reflectivity while introducing a group delay dispersion (GDD) less than 30 fs^2 ¹. However, these advanced solid-state optics are only viable for high-power experiments if the laser light is not of ionizing intensity, a problem which can be averted to some extent by expanding the size of the beam and the optic. For a laser pulse with 10PW, the beam would have to be expanded to one-meter to avoid damaging conventional solid-state optics. Manufacturing these optics at the meter-scale, especially the more intricate ones such as diffraction gratings and harmonic crystals, can be prohibitively expensive, so new avenues are needed if experiments beyond

¹See https://www.thorlabs.com/navigation.cfm?guide_id=2042 for some examples

the few petawatt level are to be performed.

To address this problem, a collection of plasma-based optics have been developed or proposed [3]. Since plasma is an already ionized medium, they can support intensities orders of magnitude higher than solid-state optics. Furthermore, under the right conditions, these plasma optics can even have superior light-manipulating properties compared to conventional optics, since plasmas can exhibit ultrafast (femtosecond to picosecond), spectrally broadband, and highly nonlinear responses to intense light. To date, several plasma-based optics have been investigated experimentally or theoretically, including plasma mirrors [4, 5], waveplates [6], q-plates [7], beam combiners and splitters, amplifiers [8], lenses [9], and gratings [10].

Constructing each of these plasma-based optics requires a different geometry of light-matter interactions. For example, to create a plasma grating [10, 11], two lasers with the same wavelength are crossed at a finite angle with sufficient intensity to ionize the gas only in regions where there is constructive interference, leading to a spatially varying index of refraction between the plasma and unionized gas. These gratings have several applications such as focusing [9] and compressing [12] intense light. On the other hand, to create a plasma waveplate or polarizer [6, 13, 14], two co-propagating lasers are crossed in a plasma which creates a refractive index perturbation and theoretically allows for full control of a probe beams polarization state. To create a plasma amplifier [8, 15–18], the parametric processes of Raman and Brillouin scattering are proposed to simultaneously amplify and compress short-pulse laser beams by five or six orders of magnitude beyond the achievable limits of CPA-based laser systems, although experimental campaigns have yet to realize these gains.

The plasma mirror, which is the primary focus of this dissertation, was one of the first plasma-based optics developed and has proven to be indispensable for manipulating high-intensity lasers on the femtosecond to picosecond timescale. They are formed when high-power lasers are focused to micron-scale spot-sizes yielding intensities high enough to ionize the surface of a solid target, such as Aluminum or glass, leading to an opaque, high-density plasma. Plasma mirrors are useful for several high-power light-matter ap-

plications, including redirection and focusing [19–21], temporal and spatial cleaning [4, 22–24], and creating highly energetic secondary particle [25] and light sources [26, 27]. In particular, for driving intensities exceeding 10^{18} W/cm^2 , harmonic radiation extending to the extreme ultraviolet wavelength regime are emitted by relativistically driven electron bunches at the surface of a plasma mirror.

1.2 Secondary radiation from plasma mirrors

High harmonic generation (HHG) from plasma mirrors was first demonstrated experimentally in 1977 using CO₂ class lasers with nanosecond pulse duration [28], where harmonics up to the 11th order were detected. Soon after, harmonic orders extending to the 46th order were experimentally measured [29, 30], and appeared to agree with initial simulation and theoretical work which predicted a spectral cut-off at the plasma frequency [31]. After these initial experimental and theoretical works, harmonic generation from solid targets declined in favor of gas-based mechanisms which were better suited to the laser technology of the time [32, 33]. Harmonic generation from gasses launched the age of attosecond science, where for the first time pulse durations shorter than an optical cycle were measured [34]. These attosecond lightsources have advanced considerably in the last few decades, including synthesizing pulses with durations of 53as [35], controlled polarization state [36], and spatial structure [37]. Despite the dramatic success of HHG from gas-based media, this mechanism is not able to take advantage of the terawatt and petawatt class lasers now available to researchers, which motivates plasma-based mechanisms for obtaining more intense harmonics and attosecond pulses. A rekindling of HHG from plasma mirrors was generated in 1996 by Gibbon who used particle-in-cell simulations to show that harmonics extending beyond the plasma frequency spectral cut-off can be generated [38], suggesting a route to creating attosecond pulses orders of magnitude more intense than those from gasses.

Harmonic generation from plasma mirrors can be broken up into two regimes depending on the laser intensity. For sub-relativistic laser intensities ($I < 10^{18} \text{ W/cm}^2$ for

800nm light), the coherent wake emission (CWE) mechanism dominates [39]. In this mechanism, dense electron bunches are accelerated by the laser field and then ejected up the plasma gradient, where plasma oscillations are excited and coherently emit radiation up until a spectral cut-off at the plasma frequency. The attosecond pulses synthesized from this mechanism are naturally chirped and possess large spatial divergence [40, 41], limiting there applicability as a secondary radiation source but can still provide valuable information on the conditions of the laser-plasma interaction.

As the laser intensity is increased beyond the relativistic threshold ($I \gtrsim 10^{18} W/cm^2$ for 800nm light) harmonics extending beyond the plasma frequency cut-off can be observed [38, 42]. In this regime several theoretical models have been proposed to explain the harmonic emission. In the relativistic oscillating mirror (ROM) model [43–45], the harmonic emission is attributed to the relativistic Doppler upshift of the incident laser due to longitudinal plasma surface oscillations. The ROM model successfully predicts the so-called selection rules of harmonic generation [44], which predicts the polarization state of radiated harmonics given the polarization state of the driving laser. However, the ROM model assumes that the plasma mirror only induces a phase modulation on the reflected beam, which simulations have shown fails across a broad range of laser and plasma parameters, particularly for p-polarized oblique interactions [26, 46–48]. Therefore, a new model which takes a microscopic point of view was developed, namely the Coherent Synchrotron Emission (CSE) model [27, 47, 49]. The CSE model attributes the harmonic emission to dense, nanometer-scaled electron bunches whose individual electrons exhibit instantaneously circular trajectories, emitting radiation described by the simple laws of synchrotron radiation [49]. Theoretical analysis coupled with particle dynamics extracted from particle-in-cell simulations predict that the radiated harmonics follow a power-law scaling ($I(\omega) \sim \omega^{-p}$), followed by a steeper power-law of ($I(\omega) \sim \omega^{-p-2}$) at a frequency given by the width of the emitting electron bunch [27], and finally an exponential roll-over at a frequency proportional to the peak relativistic Lorentz factors of emitting electrons. An extensive analysis of one-dimensional particle-in-cell simulations have shown a limiting value of $p = 4/3$, which can theoretically produce 1TW/harmonic for 1keV photons

when using a 20PW driving laser [27].

Experimental efforts on RHHG from plasma mirrors have advanced considerably within the last two decades, with early experiments measuring thousands of harmonics using the Vulcan petawatt laser at Rutherford Appleton Laboratories [50–52]. Further experiments made ground breaking measurements of the efficiency [53, 54] or divergence [41, 52, 54–56] as a function of laser intensity or pre-plasma gradient scale length. Further experiments sought to optimize the harmonic yield through tuning of the pre-plasma gradient scale length [41, 53, 57]. The early success of these experiments have prompted research into controlling the properties of the reflected light using structured lasers and targets, such as interactions with ultrathin foils [58, 59], two-color lasers [60, 61], polarization-controlled lasers [62], or vortex harmonics [63, 64].

1.3 Outline of this thesis

This thesis is organized into six chapters. The present chapter serves to motivate the core work of the thesis and also provide a roadmap to the reader on where the novel significant results are presented. Chapter two begins with a discussion on analytical and numerical modeling of laser-plasma interactions, beginning with the single electron and advancing toward particle-in-cell simulations. Novel results are presented in sections 2.2 and 2.3 where we report on the appearance of numerical artifacts and the importance of modeling collisions in PIC codes.

Chapter three and four contain experimental results on using plasma optics for manipulating intense light (chapter 3) and generating harmonics from plasma mirrors (chapter 4). In chapter 3, we present measurements of the spatial and temporal profile (on a picosecond and femtosecond timescale) of the laser before and after interacting with plasma mirrors operating in the sub-relativistic and relativistic regimes. Additionally, we discuss the implementation of a plasma grating which can be used to diffract high power light and improve the contrast of the incident laser by over 5 orders of magnitude. In chapter 4, We demonstrate the construction of a two-color, multi-terawatt laser waveform using a

plasma mirror which has high spatial quality and good focusability. The two-color waveform is then used to measure enhanced harmonic efficiency from a subsequent plasma mirror, showing a factor of 1.6 enhancement of the third and fourth harmonic orders compared to a single-color alone. Promising scaling of the third and fourth harmonics with intensity suggest that enhancement of higher orders is also possible. Additionally, measurements on the effect of beam propagation in free space on the two-color waveform which evolves as a result of the Gouy phase shift is presented, where it is shown that the enhancement factor of the third harmonic energy changes as the plasma mirror is scanned through the laser's focus.

In chapter five, we return to modeling the harmonic generation from plasma mirrors using particle-in-cell simulations, but this time turn our attention to modeling structured plasma targets and elliptically polarized driving lasers. In section 5.2, three dimensional particle-in-cell simulations are used to show that ultrathin foils irradiated with a circularly polarized laser at normal incidence emit harmonics with an azimuthally-dependent spatial wavefront characteristic of vortex beams. Additionally, in section 5.4 one and two dimensional particle-in-cell simulations are used to show that plasma mirrors driven by single-color elliptically polarized lasers emit circularly polarized harmonics that either co-rotate or counter-rotate with the reflected fundamental, depending on if the driving laser is nearly circularly polarized or nearly s-polarized, respectively. Plasma mirrors are proposed as a medium for generating two-color co- and counter-rotating high-power lasers with up to 11% and 4% conversion efficiencies, respectively, into the second harmonic. Finally, in chapter six a summary of the contributions of this thesis is provided and future work is proposed which is motivated by the results of chapters three and four.

1.3.1 Significant results

1. Experimentally used harmonic generation from a plasma mirror to construct a two-color terawatt beam, with up to 15% conversion efficiency into the second harmonic. Both colors have good spatial quality and can be simultaneously focused to the same spot.

2. Implemented a multi-pass plasma mirror configuration to show that harmonic generation from a plasma mirror using a phase-controlled, two-color driver will enhance the radiated third and fourth harmonic energy compared to a one-color driver. We found an enhancement factor 1.6 at an intensity of 1×10^{19} W/cm² with 10% of the incident laser's energy is second harmonic.
3. Experimentally demonstrated control of the two-color waveform incident on the target's surface using either a dispersive element placed in the unfocused beam path or by adjusting the target's position with respect to the incident laser's focus, showing that a two-color laser can either suppress or enhance harmonic energy compared to a one-color driving laser. Coupled with particle-in-cell simulations, this result suggests the control of electron bunches on an attosecond timescale.
4. The spatial quality of radiated harmonics, specifically the second harmonic produced from interactions when the plasma mirror positioned outside the Rayleigh range, is substantially improved after a multi-pass plasma mirror configuration when compared to a single plasma mirror.
5. The pulse duration of the laser is the same before and after interacting with a plasma mirror, but the pre-pulses on a picosecond timescale are reduced by two orders of magnitude after the interaction.
6. Plasma gratings, formed by crossing two 400nm pump lasers at an angle inside a gas, are used to diffract a 800nm probe beam, improving the temporal contrast of the probe by at least five orders of magnitude. The gratings are shown to be stable for at least one hour of continuous operation.
7. In collisionless particle-in-cell simulations, there exists a spatial resolution dependent growth in the peak density of the electron bunch, which does not plateau even at extremely high resolutions. When binary collisions are added to the particle-in-cell model, the peak electron bunch density initially exhibits the same growth, but eventually converges to a fixed value as the spatial resolution is increased.

8. Modeling collisions in particle-in-cell simulations lowers the attosecond pulse intensity as a consequence of the increased spread in time of the peak Lorentz factors of the emitting electrons, which leads to an earlier frequency cut-off than that obtained in collisionless simulations.
9. The numerical dispersion present in particle-in-cell codes based on the Yee solver is shown to have negligible effect on the temporal profiles of emitted attosecond pulses over significant propagation lengths at a required spatial resolution of ten cells per the shortest harmonic wavelength under study.
10. One and two dimensional particle-in-cell simulations show that plasma mirrors emit circularly polarized harmonics that either co-rotate or counter-rotate with the reflected fundamental, depending on if the driving laser is nearly circularly polarized or nearly s-polarized, respectively. Plasma mirrors are then proposed to generate two-color co- and counter-rotating high-power lasers with up to 11% and 4% conversion efficiencies into the second harmonic, respectively.
11. One dimensional particle-in-cell simulations are used to relate the temporal spacing of attosecond pulses to different observed harmonic structure, including harmonic broadening, harmonic splitting, and the appearance of integer and half-integer harmonics. It is demonstrated that a small amount of temporal chirp applied to the driving laser can compensate for the non-periodic emission time of attosecond pulses which results in narrower, more intense individual harmonic orders.
12. Three dimensional particle-in-cell simulations show that ultrathin foils irradiated by relativistic circularly polarized lasers emit harmonics that contain orbital angular momentum in both the transmitted and reflected directions.

Chapter 2

Modeling of Laser-Plasma Interactions: On Density Artifacts, Collisions, and Numerical Dispersion in Particle-In-Cell Simulations

2.1 Introduction

In this work, the laser field strengths are sufficiently intense that the media of interest will be fully ionized well before the arrival of the central peak of the laser. Therefore, we can largely ignore the effects of ionization in our models and focus entirely on the laser interacting with charged particles. In this chapter, we first outline the physics of high-power light-matter interactions by analytically and numerically solving the problem of a single electron exposed to a plane wave. We then introduce the fundamentals of particle-in-cell (PIC) simulations which are instrumental when moving beyond the single particle problem. Throughout this discussion we introduce key parameters and introduce the nomenclature that will be used throughout the entire text. Finally, in sections 2.2 and 2.3, we perform a thorough benchmark of using PIC simulations to model harmonic generation from plasma mirrors, outlining best practices and identifying numerical artifacts.

2.1.1 Single electron exposed to a plane wave

Here we consider the dynamics of a single electron exposed to a plane wave in vacuum. This problem is interesting in part because it lends itself to an analytic expression [65, 66] that can be used to validate simulation results, but also because straightforward extensions to the model can yield insights behind the more complicated laser-plasma interaction. Although most of results presented in this section are well known, see [67] for a comprehensive review, the results presented here are useful for introducing key parameters and nomenclature used throughout the thesis.

Consider a single electron in vacuum exposed to a linearly polarized plane wave. The governing equations for the electron's dynamics are the Lorentz force equation coupled with the energy relation:

$$\vec{F} = \frac{d\vec{p}}{dt} = -e(\vec{E} + \frac{\vec{V}}{c} \times \vec{B}) \quad (2.1)$$

$$\frac{dU}{dt} = \vec{F} \cdot \vec{V} = -e(\vec{V} \cdot \vec{E}) \quad (2.2)$$

where $\vec{p} = \gamma m \vec{V}$ is the particles momentum, e is the electrons charge, m is the electron's rest mass, \vec{V} is the electron's velocity, c is the speed of light, $U = \gamma mc^2$ is the electron's total energy, $\gamma = 1/\sqrt{1 - V^2/c^2} = \sqrt{1 + p^2/m^2c^2}$ is the relativistic Lorentz factor, t is time, and \vec{E} and \vec{B} are the electric and magnetic fields, respectively.

Assuming that the particle has negligible contribution to the electric and magnetic fields, we can solve Maxwell's equations for the electric and magnetic field of a plane wave which is expressed as follows:

$$E_y = E_L \sin(\omega_L t - k_L x) \quad (2.3)$$

$$B_z = \frac{E_L}{c} \sin(\omega_L t - k_L x) \quad (2.4)$$

where we have chosen the propagation direction of the laser to be in the x direction and the polarization direction to be in the y direction¹. Here, ω_L is the fundamental frequency

¹Throughout the thesis we will use the $x-y$ plane as the plane of incidence and z will be perpendicular to the plane of incidence. Refer to Appendix C for a complete discussion of the coordinate axes and reference frames used throughout this document.

of the laser and $k_L = \omega_L/c$ is the wavenumber.

To solve equations 2.1 and 2.2 for the electron dynamics, we introduce the vector potential, \vec{A} , defined so that $\vec{E} = \frac{-1}{c} \frac{\partial \vec{A}}{\partial t}$ and $\vec{B} = \vec{\nabla} \times \vec{A}$. Using these relations, equations 2.1 and 2.2 can be rewritten in component form as follows:

$$\frac{dp_z}{dt} = 0 \quad (2.5)$$

$$\frac{dp_y}{dt} = \frac{e}{c} \left(\frac{\partial A_y}{\partial t} + v_x \frac{\partial A_y}{\partial x} \right) = \frac{dA_y}{dt} \quad (2.6)$$

$$\frac{dp_x}{dt} = -\frac{e}{c} v_y \frac{\partial A_y}{\partial x} \quad (2.7)$$

$$\frac{dU}{dt} = -\frac{e}{c} v_y \frac{\partial A_y}{\partial t} \quad (2.8)$$

The transverse momenta can be found by integrating equations 2.5 and 2.6 directly. To find the longitudinal momentum and energy of the electron, we can subtract equation 2.8 from 2.7, which equates to zero since A_y is a function of $x-ct$ only. This allows for us to find a relation between the longitudinal momentum and energy of the electron, which can be combined with the energy relation $U = \gamma mc^2$ to find the momenta and energy as a function of the vector potential and the initial conditions:

$$p_z = p_{z0} \quad (2.9)$$

$$p_y = p_{y0} + \frac{e}{c} A_y \quad (2.10)$$

$$p_x = p_{x0} + \frac{e^2 A_y^2 + 2ce p_{y0} A_y}{2c(U_0 - cp_{x0})} \quad (2.11)$$

$$U = U_0 + \frac{e^2 A_y^2 + 2ce p_{y0} A_y}{2(U_0 - cp_{x0})} \quad (2.12)$$

Inspection of equation 2.12 shows that $U = U_0$ whenever $A_y = 0$, for example after a laser pulse has travelled passed the electron. This relation tells us that a plane wave in vacuum cannot transfer energy to the electron, a result known as the Lawson-Woodward theorem [68, 69]. We now specialize to the special case for which the electron is at rest before the arrival of the main pulse. We obtain this solution by setting $\vec{p}_0 = 0$ and

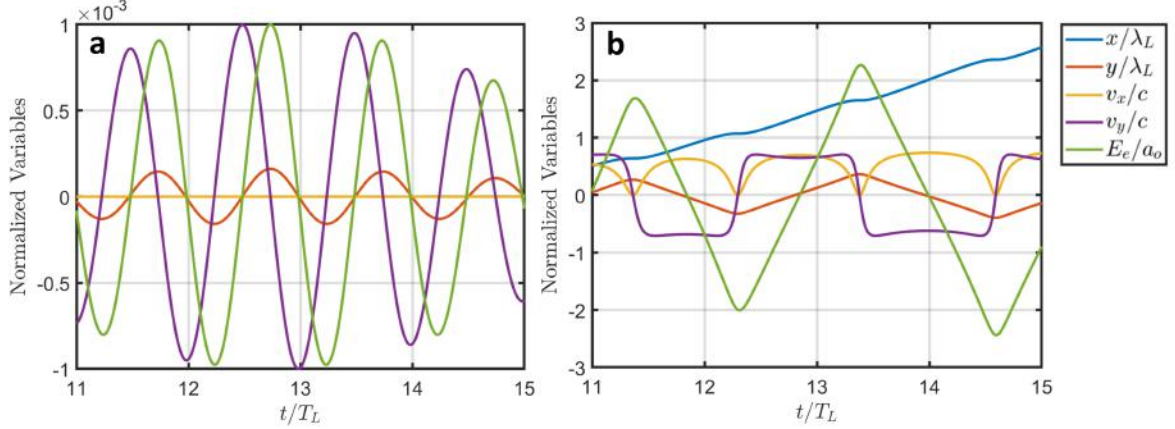


Figure 2.1: Dynamics of a single electron exposed to a plane wave in vacuum for the normalized amplitudes (a) $a_0 = 0.001$ and (b) $a_0 = 2.5$. E_e denotes the electric field strength at the position of the electron, which is stretched out in time for the relativistic case where the electron travels with the laser.

$U_0 = mc^2$ in equations 2.9 - 2.12. The resulting kinetic energy, $KE = U - mc^2$, for the electron is found to be

$$KE = \frac{e^2 A_y^2}{2mc^2} = \frac{mc^2}{2} \left(\frac{e^2 E_L^2}{m^2 \omega^2 c^2} \right) \cos^2(\omega_L t - k_L x) = \frac{mc^2}{2} (a_0^2) \cos^2(\omega_L t - k_L x) \quad (2.13)$$

Where we have inserted the equation for A_y for a plane wave, which is calculated using equation 2.3 along with the relation $E_y = \frac{-1}{c} \frac{\partial A_y}{\partial t}$. In addition, we have introduced the normalized laser amplitude, $a_0 = eE_L/m\omega_L c$. The normalized laser amplitude separates laser-particle interactions into two regimes. For nonrelativistic interactions $a_0 \ll 1$ and for relativistic interactions $a_0 \gtrsim 1$. We can see this from the kinetic energy equation since if $a_0 \ll 1$, then the kinetic energy of the electron $\ll mc^2$ and we expect relativistic effects to be negligible. As a_0 is increased toward one, the kinetic energy of the electron becomes comparable to the rest mass energy of an electron which means that relativistic effects will play a significant role in the dynamics. The normalized laser amplitude can be calculated from the specified laser intensity using the following equation:

$$a_0 = 0.85 \times 10^{-9} \sqrt{\lambda_{L,\mu m}^2 I_{L,W/cm^2}} \quad (2.14)$$

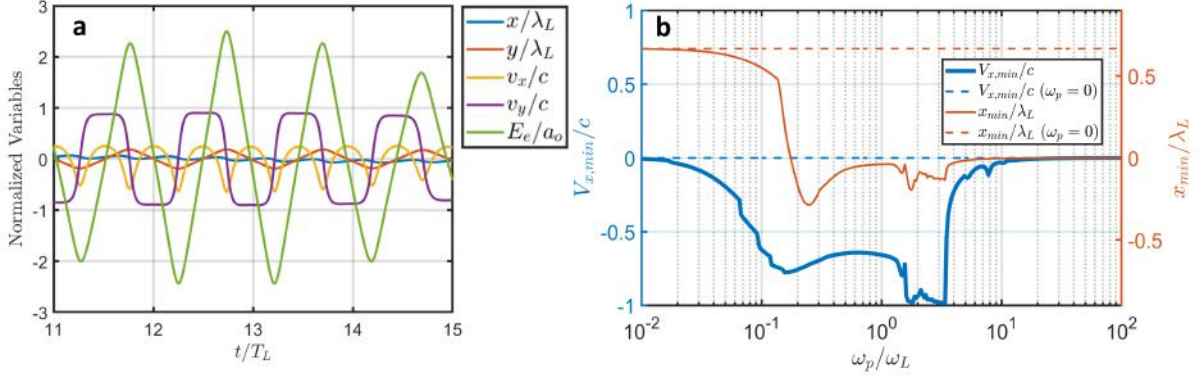


Figure 2.2: (a) Dynamics of a single electron exposed to a plane wave in vacuum with the addition of a restoring force ($\omega_p/\omega_L=1$) for the normalized laser amplitude $a_0 = 2.5$. In (b) we plot the minimum value of x and v_x that the electron experiences while interacting with the incident laser pulse as a function of ω_p/ω_L for a normalized laser amplitude of $a_0 = 2.5$.

To distinguish the electron dynamics in these two regimes, we plot the electron dynamics in figure 2.1 for the case when $a_0 = 0.001$ (non-relativistic) and for the case when $a_0 = 2.5$ (relativistic). The electron is taken to be at rest before the arrival of the plane wave. Each case shows the electrons position and velocity as a function of time. In addition, the electric field as seen by the electron is plotted as a function of time. In the sub-relativistic case, the electron simply oscillates with electric field in the y direction. The displacement of the electron in the x direction is negligible and, consequently, the electric field seen by the electron looks identical to the incident pulse. In contrast, for the relativistic case, The electron's motion is highly nonlinear where both components of the electron's velocity are non-sinusoidal. The displacement of the electron in the x direction exceeds $2\lambda_L$ and, as a result, we see that the electric field as seen by the electron is stretched in time, extending the interaction to times much greater than the initial pulse duration.

In a laser-solid interactions, the significant displacement of the electron surface from the ion background in the x direction will lead to a built up electrostatic restoring force (see section 2.2.2 for a complete discussion of the plasma dynamics of the plasma surface in laser-solid interactions). We can extend the simple model of a single electron to include the effects ions acting on electrons by introducing a restoring force, $F_{rx} = -M\omega_p^2 x$ to

the equation of motion [49]. Here, M is the total mass of the uncompensated slab of charge and $\omega_p^2 = 4\pi e^2 n_e / m$ denotes the plasma frequency, where n_e is the electron number density of the uncompensated slab of charge. This is the frequency at which the displaced electron surface would oscillate at in the absence of any external electric or magnetic fields. It is useful at this point to introduce another normalized quantity, $N_0 = \omega_p^2 / \omega_L^2 = n_e / n_c$, where $n_c = m\omega_L^2 / (4\pi e^2)$ is the plasma critical density. When $N_0 < 1$, the plasma is said to be underdense which means that an incident laser with frequency ω_L will propagate through the plasma. On the other hand, when $N_0 > 1$, the plasma is said to be overdense which means that a laser with frequency ω_L will primarily be reflected in the specular direction.

In figure 2.2(a), the dynamics of an electron at rest before the arrival of the laser pulse are plotted. In this calculation, the strength of the restoring force (ω_p / ω_L) was set to one. The most significant difference between the electron dynamics with the restoring force and without the restoring force is that negative v_x values are obtained with a restoring force. This means that the electron will have times for which it is propagating in a direction opposite that of the incident laser.

In figure 2.2(b), the minimum value of x and v_x that the electron experiences while interacting with the incident laser pulse as a function of ω_p / ω_L is plotted for a normalized laser amplitude of $a_0 = 2.5$. Here, we see that any amount of restoring force results in $v_{x,min} < 0$. However, a larger restoring force is required in order to get the electron to return to its original position (i.e. $x_{min} \leq 0$). For $a_0 = 2.5$, a value of $\omega_p / \omega_L > 0.15$ results in the electron returning to its initial location after being displaced by the laser. At this value of N_0 , the laser force, which is governed by a_0 , and the plasma restoring force, which is governed by N_0 , are close to balanced. As ω_p / ω_L is increased further, the restoring force is too great for the laser to displace the electron at all, so the electron simply oscillates in the transverse plane at $x = 0$.

2.1.2 Particle-in-cell simulations

To model the complex interaction of relativistically intense lasers incident on solid density plasmas, the single particle model described above is not sufficient as we need to extend the model to more than one particle and apply the Lorentz force law to each pairs of particles, which is impractical both analytically and numerically. For these reasons, we turn to a kinetic description of a plasma for which we have the Vlasov-Maxwell system defined as follows:

$$\frac{\partial f}{\partial t} + \vec{v} \cdot \frac{\partial f}{\partial \vec{x}} + \vec{F} \cdot \frac{\partial f}{\partial \vec{p}} = 0 \quad (2.15)$$

$$\vec{\nabla} \cdot \vec{E} = 4\pi\rho \quad (2.16)$$

$$\vec{\nabla} \cdot \vec{B} = 0 \quad (2.17)$$

$$\vec{\nabla} \times \vec{E} = -\frac{1}{c} \frac{\partial \vec{B}}{\partial t} \quad (2.18)$$

$$\vec{\nabla} \times \vec{B} = \frac{4\pi}{c} \vec{J} + \frac{1}{c} \frac{\partial \vec{E}}{\partial t} \quad (2.19)$$

where $f = f(\vec{r}, \vec{v})$ is the six dimensional single particle distribution function, \vec{F} is the Lorentz force law, ρ is the charge density distribution, and \vec{J} is the current density.

Although this is a complete description of the laser-plasma interactions we are interested in studying, the Vlasov-Maxwell system is, in general, too complex for analytical solutions. Numerically solving the Vlasov equation directly is also challenging since it is six dimensional (three spatial and three velocity) and would therefore require enormous computational power. Even for problems that can be modeled in a reduced geometry of one spatial dimension, at least two velocity dimensions are generally required to capture the motion of particles in the electromagnetic fields, which would still be challenging to simulate. Despite these drawbacks, direct Vlasov codes have been developed and applied to intense laser-solid interactions [70], which shows promise in obtaining smoother solutions (less computational noise) than simulations using particles.

The particle-in-cell (PIC) scheme, developed over 60 years ago [71–73], is a more practical approach for solving this system of equations. In the PIC scheme, the distribution

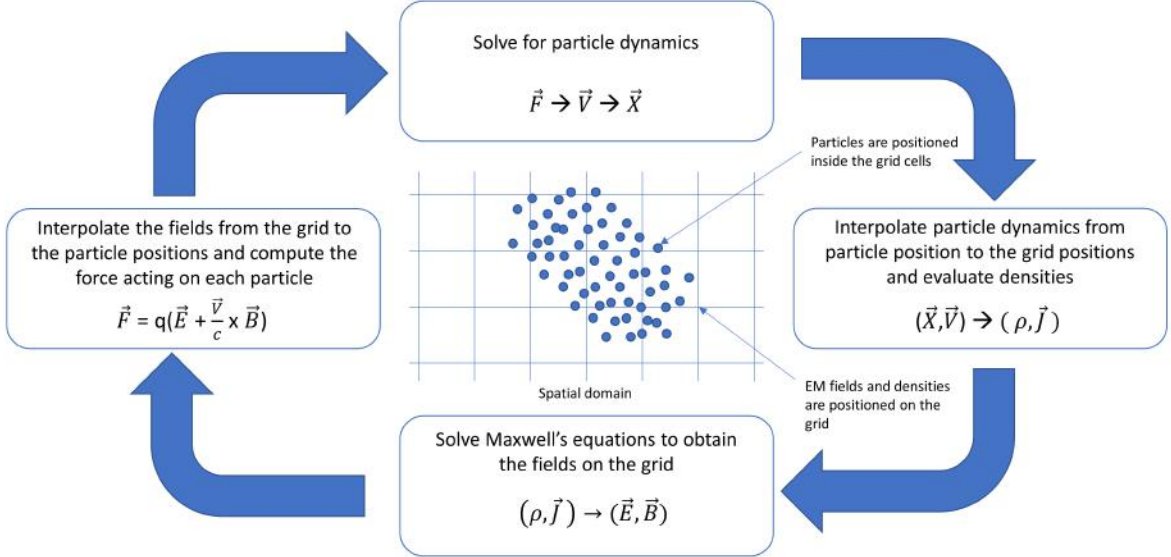


Figure 2.3: A schematic diagram of the particle-in-cell algorithm

function is represented with finite-sized macroparticles. The macroparticles themselves are physically thought of as representing a number, N , of real particles, so that the charge and mass of each macroparticle is $Q = Nq_s$ and $M = Nm_s$ for species s, respectively. Each of these macroparticles interact with each other in the self-consistent electric and magnetic fields that they produce or that is externally applied. These finite-sized particles in PIC are good for modeling long-range, collective plasma phenomena, but reduce the effects of short-range, collisional interactions since the force between two overlapping particles goes to zero [72].

The PIC algorithm is schematically shown in figure 2.3. The simulations are initialized with the particle positions and velocities located anywhere in the simulation domain. The electric and magnetic fields, though, are initialized on a grid. To complete one iteration of the PIC loop we first need to map the particles position and velocity to the grid in order to calculate the charge and current density. This can be done as follows:

$$\rho_s(\vec{r}) = \sum_j q_{js} S(\vec{r}_j - \vec{r}) \quad (2.20)$$

$$\vec{J}_s(\vec{r}) = \sum_j q_{js} \vec{v}_{js} S(\vec{r}_j - \vec{r}) \quad (2.21)$$

where S is the function which defines the particle shape. The simplest particle shape is a top-hat function (zeroth order weighting), in which the particles are assigned to their nearest grid point. However, this results in a high level of numerical noise which is impractical for most applications. A triangular particle shape (first order (linear) weighting), is the standard choice for doing this interpolation, although higher-order shape functions are sometimes used to reduce the effects of numerical heating [74].

With the charge and current densities now known on the grid, the actual updating of the fields via solving Maxwell's equations can be done in several ways. The standard approach used in several PIC codes is the Yee scheme [75], which is an explicit second order (in space and time) finite-difference time-domain (FDTD) algorithm. The Yee scheme as it is straightforward to implement and is highly scalable, allowing for the use of millions of cores. However, the Yee scheme has drawbacks, namely that it introduces numerical dispersion as a result of being a FDTD scheme. full discussion of the effects of numerical dispersion on propagating attosecond pulses in vacuum is presented in section 2.2.1.

In the next step of the PIC algorithm the updated fields are interpolated back to the particle positions using the same weighting function, S , used to map the particle positions and velocities to the grid. Knowing the fields at the particle position lets us evaluate the Lorentz force via equation 2.1. Finally, knowing the force acting on all particles, we can solve for the updated particle positions and velocities, which completes one iteration of the particle-in-cell loop depicted in figure 2.3.

2.2 Using particle-in-cell simulations for modeling relativistic harmonic generation

The particle-in-cell (PIC) method, extensively used to numerically simulate laser-plasma interactions [74, 76–78], employs physical approximations and introduces numerical artifacts. To solve Maxwell's equations on a grid, conventional PIC codes utilize a finite-difference time-domain (FDTD) method, the Yee solver [75], which is subject to numerical

dispersion [79–87]. Numerical dispersion poses a significant challenge for modeling high-order harmonics that comprise a broad range of frequencies. Recently, pseudo-spectral Maxwell solvers based on fast Fourier transforms have been implemented to mitigate numerical dispersion and noise[88–93], and dispersion-free propagation of harmonics has been demonstrated [90]. The PIC method also employs finite-sized macroparticles which represent a number of real particles in the system. Macroparticles accurately model long-range, collective plasma phenomena, but reduce the magnitude of the electromagnetic fields for short-range, collisional interactions [72]. To restore these short-range interactions, Monte-Carlo-based algorithms for modeling binary collisions between macroparticles have been developed [94–100], and have been applied to short-pulse laser-solid interaction studies [101–103]. In this section we investigate the implications of these approximations and numerical artifacts within the context of simulating harmonic generation from plasma mirrors.

2.2.1 Space and time discretization - numerical dispersion

Relativistic high harmonic generation experiments are performed in vacuum to avoid the nonlinear effects of high intensity laser propagation in air. In vacuum, the dispersion relation of electromagnetic waves is independent of wavelength, but the algorithm used in conventional PIC simulations to advance the fields is the FDTD-based Yee scheme, which has a numerical dispersion relation and associated group velocity that can be expressed as follows [77, 78]

$$\omega = \frac{2}{\Delta t} \sin^{-1} (C \sin (k\Delta x/2)) \quad (2.22)$$

$$\frac{v_g}{c} = \frac{1}{c} \frac{d\omega}{dk} = \frac{\cos (k\Delta x/2)}{\sqrt{1 - C^2 \sin^2 (k\Delta x/2)}} \quad (2.23)$$

Inspection of Eq. (2.23) shows that, for fixed temporal and spatial resolution, the speed of light in vacuum decreases as the frequency of the radiation increases. In this section, we show that the frequency-dependent group velocity present in the FDTD-based Yee scheme

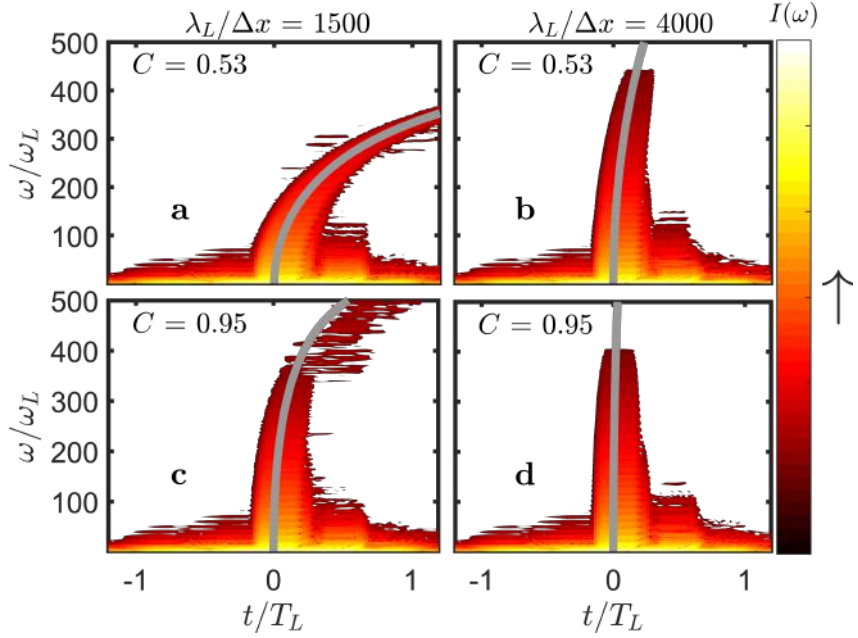


Figure 2.4: Spectrograms of the reflected electric field from PIC simulations for $C = \{0.53, 0.95\}$ and $\lambda_L/\Delta x = \{1500, 4000\}$. The other parameters of the simulation are $\theta = 0^\circ$, $a_0 = 40$, $N_0 = 200$, and particles/cell = 50. The reflected electric field propagated for four laser wavelengths before being recorded in time at a fixed spatial location. The gray line is calculated using equation 2.23 and assumes that all frequencies were emitted at the same time.

has negligible effect on the propagation of attosecond pulses for significant propagation lengths as a result of needing high spatial resolution to resolve the attosecond pulses at the time of emission.

To illustrate the effects of numerical dispersion on the propagation of attosecond pulses, we analyze the reflected electric field using spectrograms, where each spectrogram is constructed using a Gaussian-shaped gating window with a full width half maximum of $0.5T_L$. In Fig. 2.4, spectrograms of the reflected electric field from four PIC simulations are plotted, where each simulation was performed using a spatial resolution of either $\lambda_L/\Delta x = 1500$ or $\lambda_L/\Delta x = 4000$ and a CFL number of either $C = 0.53$ or $C = 0.95$. For $\lambda_L/\Delta x = 4000$ and $C = 0.95$ [Fig. 2.4(d)], the spectrogram consists of a vertical line centered at $t = 0$ which indicates that all frequencies were emitted at the same time. As $\lambda_L/\Delta x$ is decreased to 1500 and C is decreased to 0.53, the high frequency radiation of the spectrogram bends toward later times, reflecting the fact that higher frequencies are traveling slower than the speed of light.

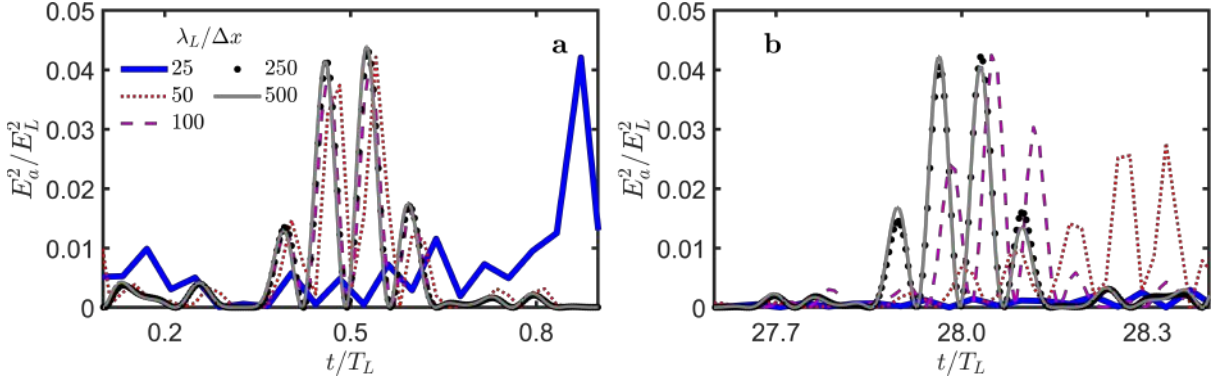


Figure 2.5: Effects of spatial resolution on the attosecond pulse temporal profile for the parameters $\theta = 0^\circ$, $a_0 = 40$, $N_0 = 200$, varied $\lambda_L/\Delta x$, particles/cell = 100, and $C = 0.95$. (a) Attosecond pulses immediately after emission for five different spatial resolutions. The attosecond pulses are constructed using radiation in the frequency range $4 < \omega/\omega_L < 10$. (b) The same five attosecond pulses, but after they have propagated for 28 laser periods.

Numerical dispersion causes a temporal chirp in the propagating attosecond pulse as a result of the frequency-dependent propagation speeds. However, we emphasize here that, at the high resolutions needed to resolve the emission of the attosecond pulse at all, the deleterious effects of group velocity mismatch on the attosecond propagation are negligible for significant propagation lengths. Figure 2.5 illustrates the difference between poorly resolved attosecond pulses immediately after the time of emission [Fig. 2.5(a)] and attosecond pulses that have become temporally chirped as a result of numerical dispersion after propagating in vacuum for 28 laser periods [Fig. 2.5(b)]. For the frequency range used to construct the attosecond pulses in figure 2.5 ($4 < \omega/\omega_L < 10$), a spatial resolution of $\lambda_L/\Delta x \gtrsim 50$ is needed to accurately resolve the attosecond pulse at the time of emission. After propagating for 28 laser periods, the intensity of the attosecond pulse drops by only a factor of two for $\lambda_L/\Delta x = 50$, and not at all for $\lambda_L/\Delta x \gtrsim 100$.

Since we have an analytic expression for the numerical dispersion of electromagnetic waves in vacuum (gray lines in Fig. 2.4), we can define a criterion that specifies the smallest wavelength for which the effects of numerical dispersion are negligible based on a given C , Δx , and propagation length. Here, the effects of numerical dispersion are considered significant when radiation at a wavelength, λ_n , has traveled a distance $\lambda_n/2$ less than it would have if it propagated according to the continuous dispersion equation. At this point, the numerically propagated wavelengths greater than or equal

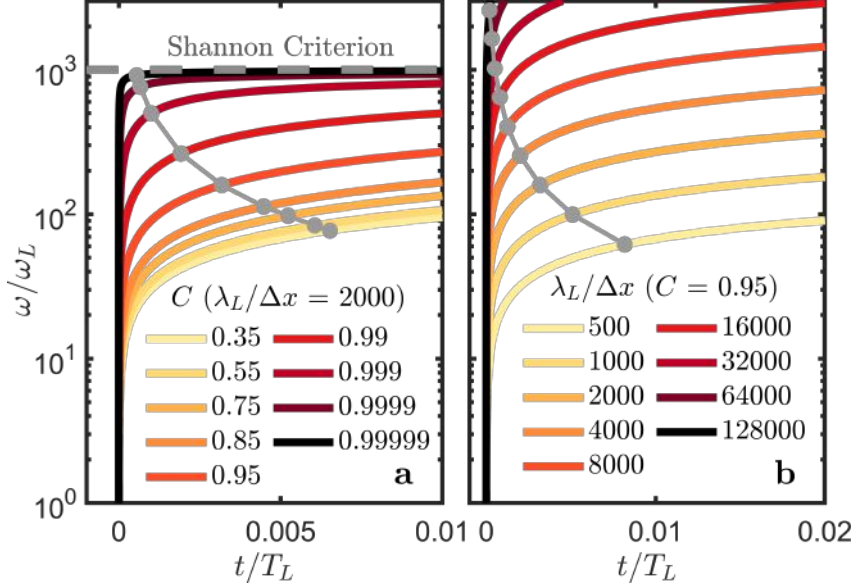


Figure 2.6: Analytic spectrograms calculated from equation 2.23. The calculation assumes all frequencies are emitted at the same time and have propagated for one laser period. (a) Spectrograms for varied spatial resolution and $C = 0.95$. (b) Spectrograms for varied CFL number and $\lambda_L/\Delta x = 2000$. The gray dots are located at a frequency (ω_n) such that $t/T_L = \omega_L/(2\omega_n)$.

to λ_n would have completely destructively interfered with the continuum versions of themselves. According to this criterion, only the cases in Fig. 2.5(b) with $\lambda_L/\Delta x > 150$ will have suppressed the effects of numerical dispersion.

To get an intuitive feeling for this criterion, we construct analytic spectrograms across a wide range of CFL numbers [Fig. 2.6(a)] and spatial resolutions [Fig. 2.6(b)]. As illustrated in Fig. 2.6(a), the highest resolved frequency approaches the Nyquist-Shannon criterion ($\omega/\omega_L = \lambda_L/2\Delta x$) as the CFL number approaches 1. Theoretically, setting $C = 1$ will allow for dispersion-free propagation, but the simulation will only be marginally stable. Increasing the CFL number from $C = 0.95$ to $C = 0.999$ will suppress numerical dispersion from harmonic order $\omega/\omega_L = 100$ to $\omega/\omega_L = 300$ when $\lambda_L/\Delta x = 1000$ and a propagation distance of $1\lambda_L$ is used. Increasing the spatial resolution will also suppress numerical dispersion [Fig. 2.6(b)], but the computational expense (memory and time) will increase considerably. For comparison, to suppress numerical dispersion from harmonic order $\omega/\omega_L = 100$ to $\omega/\omega_L = 300$ would require increasing the spatial resolution from $\lambda_L/\Delta x = 1000$ to $\lambda_L/\Delta x = 6000$ when $C = 0.95$ and a propagation distance of $1\lambda_L$ is used. For these reasons, it is desirable to choose C close to one for a particular spatial

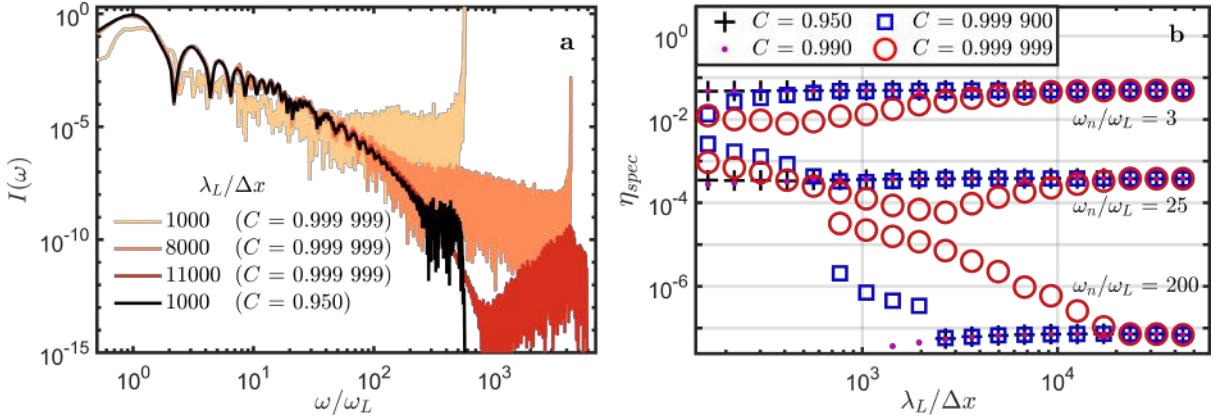


Figure 2.7: Numerical error in PIC simulations as a result of choosing a CFL number close to the stability limit ($C = 1$) for the parameters $\theta = 0^\circ$, $a_0 = 40$, $N_0 = 200$, particles/cell = 50, varied $\lambda_L/\Delta x$, and varied C . (a) Spectral intensity of the total reflected field for $C = 0.999\ 999$ and $\lambda_L/\Delta x = 1000$, 8000, and 11000 as well as for $C = 0.95$ and $\lambda_L/\Delta x = 1000$. (b) Spectral efficiency contained in the frequency range $-0.5 + \omega_n/\omega_L < \omega/\omega_L < 0.5 + \omega_n/\omega_L$ for the n^{th} harmonic order as a function of $\lambda_L/\Delta x$ for four different CFL numbers.

resolution without resulting in an instability.

We performed a set of simulations with varying spatial and temporal resolution with C in the range of 0.95 - 0.999 999 and $\lambda_L/\Delta x$ in the range of 100 - 50000 (Fig. 2.7). Fig. 2.7(a) shows the reflected field's spectrum for three different spatial resolutions and $C = 0.999\ 999$. For simulations with $\lambda_L/\Delta x < 10000$, an instability develops which has the fastest growth rate at the Nyquist frequency. To achieve convergence in spectral intensity at $\omega/\omega_L = 100$ requires using a spatial resolution of $\lambda_L/\Delta x > 10000$, which is an order of magnitude higher than if a lower CFL number of $C = 0.95$ was used. For comparison, the spectrum obtained from a simulation with $C = 0.95$ and $\lambda_L/\Delta x = 1000$ is plotted in black in Fig. 2.7(a).

In Fig. 2.7(b) the spectral efficiency is plotted as a function of $\lambda_L/\Delta x$ for three different harmonic orders ($\omega_n/\omega_L = 3$, 25, 200) and four different CFL numbers. For C values between 0.95 and 0.99, the numerical error resulting from the instability is negligible for all $\lambda_L/\Delta x$. However, for $C > 0.99$ the instability affects the spectral energy for both low ($\omega_n/\omega_L = 3$) and high ($\omega_n/\omega_L = 200$) harmonic orders and requires at least an order of magnitude higher spatial resolution for the spectral efficiency to converge to a fixed value. These results suggest there is no advantage to using a CFL number greater

than 0.99 to mitigate numerical dispersion since a higher CFL number requires increased spatial resolution to suppress the induced numerical instabilities.

Increasing the number of particles/cell present at the start of the simulation does not suppress the instability in PIC that is present when the CFL number approaches the stability limit (Fig. 2.8). In Fig. 2.8 (a), the spectral efficiency for the frequency range $10 < \omega/\omega_L < 40$ is plotted as a function of the number of particles/cell present at the start of the simulation for different values of C . For all values of C , the spectral energy converges to a fixed value as the number of particles/cell is increased. Here we see that the spectral efficiency approaches a fixed value as the number of particles/cell is increased for all cases of C , but only for the cases where $C < 0.9999$ does the spectral efficiency converge to the same value independent of the chosen C . In Fig. 2.8 (b), we plot the reflected spectra for simulations with $C = 0.9999$ and particles/cell = 2, 80, 850, and 4000 (colored lines) and for simulations with $C = 0.95$ and particles/cell = 4000 (black line). Here we see that an instability has taken place for all simulations with $C = 0.9999$, even though the spectral intensity seems to converge to a fixed value at all harmonic orders with increasing particles/cell.

In conclusion, we showed that the minimum spatial resolution needed to resolve attosecond pulse emission is also sufficient to suppress numerical dispersion for significant propagation lengths. In addition, although choosing CFL numbers close to one is a promising way to achieve dispersion-free propagation of harmonics, it leads to numerical errors as it is close to the stability limit. These numerical errors can be corrected only by increasing the spatial resolution, which requires more computational expense and, therefore, largely offsets the advantages for choosing a higher CFL number.

2.2.2 Attosecond electron bunch dynamics

At relativistic laser intensities, solid surfaces turn into fully-ionized plasmas that reflect the incident light and emit high-order harmonics extending well into the x-ray range and forming attosecond pulses [26, 38, 44, 50, 53, 54, 57, 104–107]. On a microscopic level, the process of relativistic high-order harmonic generation is well described by the coherent

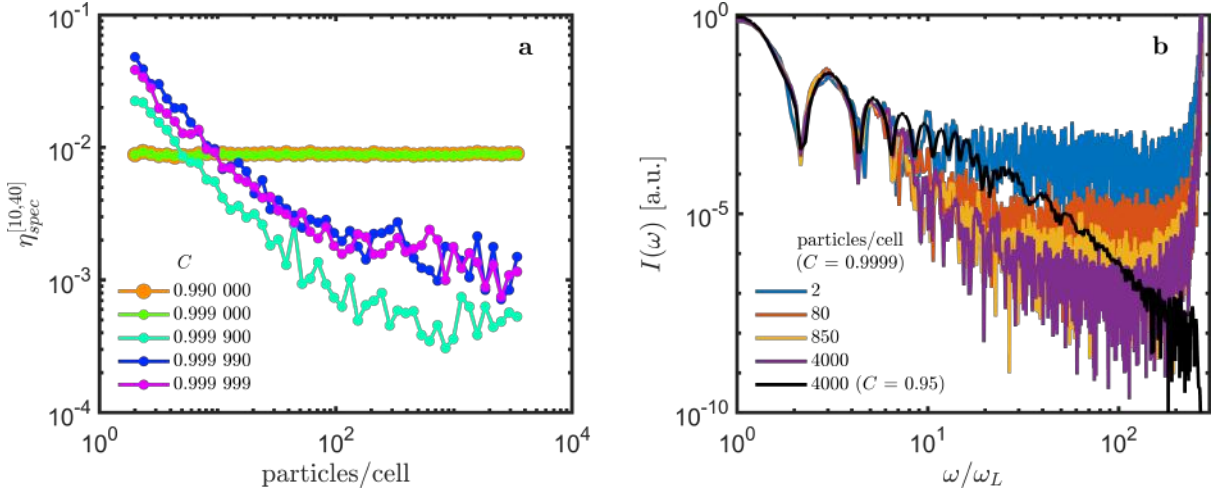


Figure 2.8: Effects of particles/cell present at the start of the simulation on the numerical error resulting from choosing a CFL number close to the stability limit. (a) Spectral efficiency for the frequency range $10 < \omega/\omega_L < 40$ as a function of particles/cell for various C values. (b) Reflected spectra for simulations with $C = 0.9999$ and particles/cell = 2, 80, 850, and 4000 and for simulations with $C = 0.95$ and particles/cell = 4000, showing that reducing particle noise does not remove the instability when $C = 0.9999$. Relevant simulation parameters: $a_0 = 40$, $N = 200$, $\tau/T_L = 1$, $\phi_{CEP} = 90^\circ$, $D = 0.50$, $L = 0$, $\lambda_L/\Delta x = 500$, $\theta = 0$.

synchrotron emission (CSE) model that explains harmonic emission as a result of the sub-laser-cycle formation and acceleration of dense, nanometer-sized electron bunches [27, 49, 58, 108, 109]. The distribution of electrons in an emitting bunch plays a critical role in the efficiency as well as the temporal and spectral profiles of the emitted radiation, whether the density distribution is viewed as a function of space at a fixed time [108–111] or as a function of the advanced time coordinate [27, 112]. Previous work has shown that the electron bunches can be controlled by tailoring the driving laser’s waveform to achieve enhanced harmonic efficiency [60, 113–116]. Manipulating the electron bunches to control the properties of the harmonic radiation requires a detailed understanding of how the electron bunch evolution depends on the laser and plasma parameters.

Here we aim to examine the characteristic features in the spatial distributions of electron densities at times before and near the time of attosecond pulse emission and understand the effect of spatial resolution, and collisions in conventional PIC simulations on the properties of accelerated electron bunches and their emission. Using the EPOCH PIC code [74], we provide a detailed analysis of the electron bunch evolution for different

relativistic laser–solid interaction scenarios in collisionless and collisional simulations. We demonstrate the appearance of unphysical density spikes with the peak density growing with increasing spatial resolution in collisionless simulations. We show, however, that these density spikes have no effect on the intensity of emitted harmonic radiation. We then analyze the effects of collisions on the electron bunches, showing that the unphysical density spikes disappear with collisions and, in addition, collisions are shown to increase the spread in time of the peak Lorentz factors of emitting electrons within the electron bunch, which reduces attosecond pulse intensity compared to collisionless simulations.

Since the formation of individual electron bunches in relativistic laser-solid interactions occurs on a sub-laser-cycle timescale, we consider single-cycle laser pulses interacting with semi-infinite plasma slabs, which result in the continuous spectra of plasma emission analyzed below. We model normal and oblique incidence interactions in a one-dimensional geometry, where a relativistic transform to a boosted reference frame is used for oblique incidence [117, 118]. The incident laser’s wave vector is at an angle θ with respect to the x-axis in the $x - y$ plane, where the target’s normal vector points in the negative x direction. The laser pulse strength is given by the relativistic amplitude $a_0 = eE_L/(m\omega_L c)$, where c is the speed of light, e and m are the electron’s charge and mass, E_L is the maximum of the electric field envelope, and ω_L is the driving laser’s angular frequency. For all simulations, the laser was p-polarized with a wavelength of $\lambda_L = 800\text{nm}$. The plasma slab has a step-like density profile with an initial electron number density of N_0 , where N_0 is normalized by the critical density ($n_c = m\omega_L^2/(4\pi e^2)$). The simulations use a second-order FDTD scheme to solve Maxwell’s equations, for which the time step, Δt , is determined by the Courant-Friedrichs-Lowy (CFL) number, $C = c\Delta t/\Delta x$, where Δx is the size of the spatial cell of the numerical grid. The simulations presented here use a spatial resolution between 100 and 100,000 cells per laser wavelength and a CFL number between 0.50 and 1.0.

In this work, we are interested in the evolution of the electron number density (N_e , which is normalized by n_c), the distribution of electron relativistic Lorentz factors (γ) at the time of attosecond pulse emission, and the attosecond pulse generation efficiency.

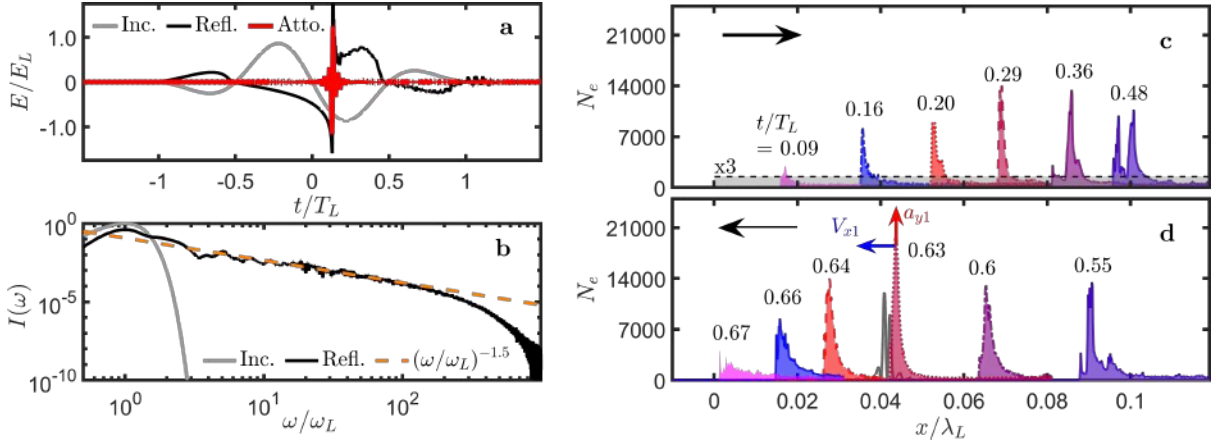


Figure 2.9: Attosecond pulse emission (a,b) and sub-cycle density dynamics (c,d) of relativistic electron bunches near the surface of a plasma mirror from PIC simulations. Simulation parameters are: $\theta = 30^\circ$, $a_0 = 175$, $N_0 = 500$, $\lambda_L/\Delta x = 8000$, particles/cell = 50, and $C = 0.95$. (a) The electric fields of incident (gray), reflected (black), and filtered attosecond pulse (red) as a function of time. (b) Spectral intensity of the incident (gray) and reflected (black) laser pulse, and a power-law fit of the reflected spectrum in the frequency range $1 < \omega/\omega_L < 10$ (dashed). (c,d) Spatial distribution of the electron density (N_e) for different times within a single cycle of the incident laser field. (c) Electron bunch is moving to the right into the bulk of the plasma pushed by the laser field. (d) Electron bunch is moving to the left toward vacuum. The attosecond pulse is emitted at $t/T_L = 0.63$, when the velocity and acceleration are perpendicular to each other.

The electric fields of attosecond pulses, E_a , are obtained by filtering the reflected electric field in the frequency range $\omega_{LF} < \omega/\omega_L < \omega_{UF}$. The attosecond pulse generation efficiency, η_{atto} , is defined as the peak value of E_a^2/E_L^2 . The spectral efficiency of frequency upconversion, η_{spec} , is calculated by integrating the spectral intensity of the reflected laser, $I(\omega)$, in the frequency range $\omega_{LF} < \omega/\omega_L < \omega_{UF}$ and then dividing by the integrated spectral intensity of the incident laser. The incident and reflected spectra have been normalized by the peak value of the incident laser's spectral intensity.

The attosecond pulse emission and the sub-cycle plasma dynamics in relativistic laser-solid interactions are shown in Fig. 2.9. In the time domain [Fig. 2.9(a)], the reflected waveform is substantially distorted compared to the incident one, indicating the presence of high frequency radiation. Transforming to the frequency domain [Fig. 2.9(b)], we observe a broadband, continuous spectrum which follows a power-law scaling up to a frequency cut-off ($\omega/\omega_L \approx 200$) after which a steeper decline in spectral intensity is observed. The dashed orange line in Fig. 2.9(b) represents a power-law fit ($I(\omega) \propto$

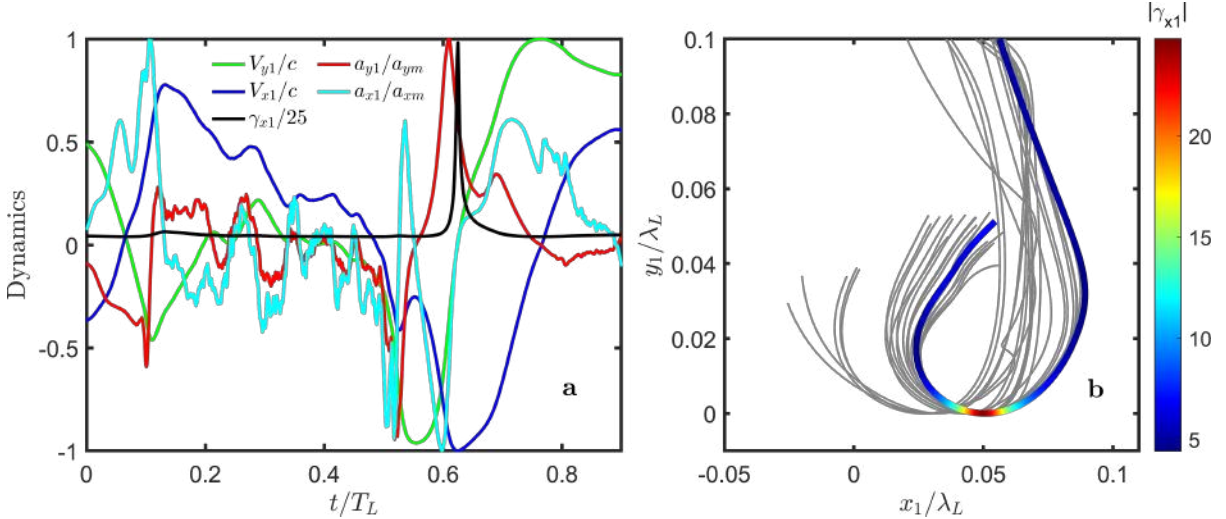


Figure 2.10: (a) Dynamics of a selected electron leading up the emission of the attosecond pulse. The dynamics are plotted in a coordinate system (x_1, y_1) that is parallel and perpendicular to the specular direction. The two components of acceleration have been normalized to their maximum values. (b) Selected electron trajectories that contribute to the emitted attosecond pulse. The colormap indicates the magnitude of the relativistic Lorentz factor of the electron from (a). The simulation parameters are the same as those from the simulation from figure 2.9

$(\omega/\omega_L)^{-p}$) in the frequency range $1 < \omega/\omega_L < 10$. Filtering out the low harmonic orders ($\omega/\omega_L < 30$) and transforming back to the time domain results in an attosecond pulse, as shown by the red line in Fig. 2.9(a).

The spatial distributions of the electron density for particular instants of time during the interaction are presented in Fig. 2.9(c,d). The time $t/T_L = 0$ corresponds to the instant when the laser's electric field node (the node that precedes the attosecond pulse emission) first meets the plasma surface, where the electric field nodes are defined as the points in space where the incident electric field is zero. As the laser starts interacting with the plasma, the $v \times B$ force and the force from the component of the laser's transverse electric field that acts in the target's normal direction combine to displace the electrons from their initial location, forming a dense electron nanobunch [Fig. 2.9(c)]. The displacement of the electron surface results in a built-up electrostatic restoring force which subsequently accelerates the electron bunch toward the specular direction where it narrows in space and increases in peak density, emitting an attosecond pulse at $t/T_L = 0.63$ [Fig. 2.9(d)].

The dynamics of a single emitting electron within the bunch are shown in Fig. 2.10(a), where the particle data is plotted in the reference frame (x_1, y_1) , which is rotated by an angle θ with respect to (x, y) , so that x_1 is parallel to the direction of specular reflection. The time of emission corresponds to the spike in the relativistic Lorentz factor, γ_{x1} , when the electron's velocity is along the specular direction and the acceleration is perpendicular to the velocity, which is in agreement with the CSE model [49]. In Fig. 2.10(b), shows the trajectories of emitting electrons within the electron bunch in the x_1 - y_1 plane. The false color on one of the electrons represents the value of the relativistic Lorentz factor. The time of emission occurs when γ_{x1} has its maximum value, which happens when the electron is at $x_1/\lambda_L \approx 0.05$.

The efficiency of attosecond pulse generation is highest when the laser force, which is a function of a_0 , and the plasma restoring force, which is a function of N_0 , are of similar magnitude, and not necessarily at exactly the same time [27, 116]. This balance can be characterized by the similarity parameter $S = N_0/a_0$, or $1/S = a_0/N_0$, which arises from the similarity analysis of laser-plasma interactions in the ultra-relativistic limit [119]. The brightest attosecond pulses occur when $a_0/N_0 \approx 0.3$ for normal incidence interactions and for $a_0/N_0 \approx 0.5$ for oblique incidence interactions [27]. In Fig. 2.11, we show the evolution of the electron density spatial distribution and the emitted attosecond pulses for normal ($\theta = 0^\circ$) and oblique ($\theta = 30^\circ$) incidences and various ratios of a_0/N_0 . In each subplot, the electron bunch evolves from the time when the electron bunch has its maximum displacement from the initial plasma-vacuum interface (T_{MaxDisp}) through the time when the attosecond pulse is emitted (T_{Emission}). The dashed line indicates the peak density of the electron bunch at different points in time.

For $a_0/N_0 \lesssim 0.1$ [Fig. 2.11(a,b)], the electron bunch evolution in normal and oblique incidence simulations are similar: the peak density of the electron bunch slowly drops, while its width remains roughly the same. The attosecond pulse is emitted at $t/T_L \approx 0.5$, at which point the electron bunch has expanded close to the original density, resulting in inefficient attosecond pulse generation. In contrast, for $a_0/N_0 \gtrsim 0.2$ [Fig. 2.11(d–k)], the electron bunch is compressed in space as it accelerates toward vacuum for both

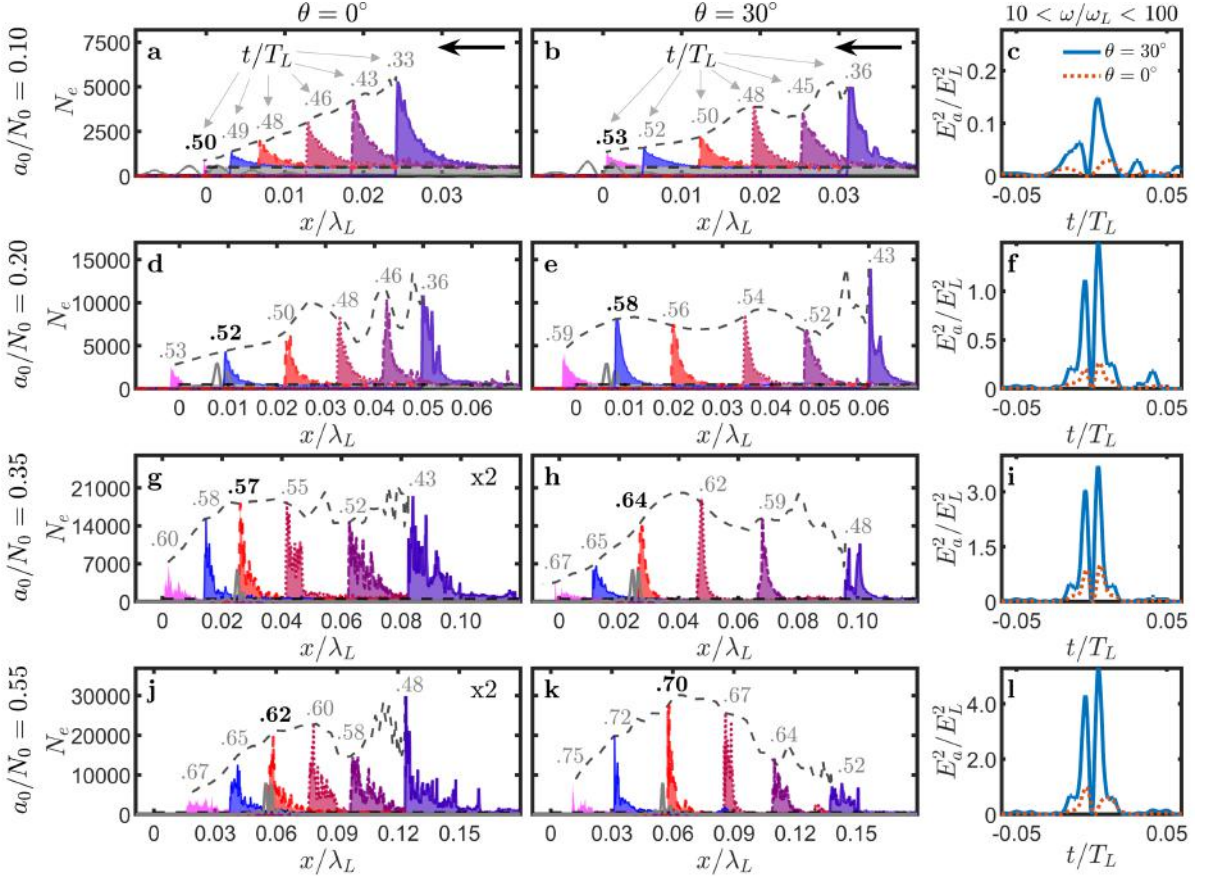


Figure 2.11: Spatial distributions of the electron number density (N_e) illustrating the electron bunch evolution from the time when the electron bunch has its maximum displacement from the initial plasma-vacuum interface (T_{MaxDisp}) through the time when the attosecond pulse is emitted (T_{Emission}). The simulation parameters are $N_0 = 500$, particles/cell = 50, $\lambda_L/\Delta x = 8000$, $C = 0.95$, and $a_0/N_0 = 0.10$ (a-c), $a_0/N_0 = 0.20$ (d-f), $a_0/N_0 = 0.35$ (g-i), and $a_0/N_0 = 0.55$ (j-l). The dashed gray line marks the electron bunch's peak density as it evolves from right to left and emits the attosecond pulse. The bold times within each subplot indicate the time of emission. The density distributions in subplots (g) and (j) have been scaled by a factor of two, as indicated in the upper right corner, so that the distribution of the electron density is easier to visualize at this scale. The attosecond pulses were constructed using radiation in the frequency range $10 < \omega/\omega_L < 100$.

the normal and obliquely incident cases. For normal incidence interactions, the electron bunch never reaches a peak density higher than what is obtained at T_{MaxDisp} , but rather maintains its peak density through the time of attosecond pulse emission. For oblique incidence interactions, emission occurs when the electron bunch has a peak density higher than that obtained at T_{MaxDisp} [Fig. 2.11(h,k)]. This results in more efficient attosecond pulse generation than that obtained for values of $a_0/N_0 \lesssim 0.1$. Note that the times of the attosecond pulse emission extend beyond one-half of a laser period in the interactions with $a_0/N_0 \gtrsim 0.2$ as a result of the increased displacement of the electron bunches from the initial plasma-vacuum interface.

2.2.3 Resolution-dependent spikes of the electron density

As the intensity, spectra, and duration of the emitted radiation critically depend on the electron density distribution at the time of emission and on the temporal distribution of individual electron Lorentz-factors in an emitting electron bunch, the capacity of PIC simulations to accurately model electron density dynamics is essential for the prediction of the emission properties. This brings up questions regarding the effects of the spatial resolution and number of particles/cell present at the start of the simulation on the electron density dynamics. To address these questions, we first examine the dependence of the peak density of electron bunches on the spatial cell size of the numerical grid. The peak electron density (N_{peak}) at the times T_{MaxDisp} and T_{Emission} is plotted as a function of $\lambda_L/\Delta x$ in Fig. 2.12(i) for different sets of simulation parameters: (a) $\theta = 0^\circ$, $a_0 = 40$, $N_0 = 200$; (b) $\theta = 30^\circ$, $a_0 = 175$, $N_0 = 500$; (c) $\theta = 30^\circ$, $a_0 = 325$, $N_0 = 500$. As is shown in Fig. 2.12(i), the peak electron density exhibits a power-law growth as a function of $\lambda_L/\Delta x$, and does not converge to a fixed value even at an extremely high resolution of $\lambda_L/\Delta x > 35000$.

The spatial distributions of the electron density at the times T_{MaxDisp} and T_{Emission} are plotted in Figs. 2.12(ii) and 2.12(iii), respectively. For each instant of time, the distributions are plotted with a dotted blue line for simulations with $\lambda_L/\Delta x = 4000$ and with a solid cyan line for simulations with $\lambda_L/\Delta x = 35000$. In these collisionless PIC

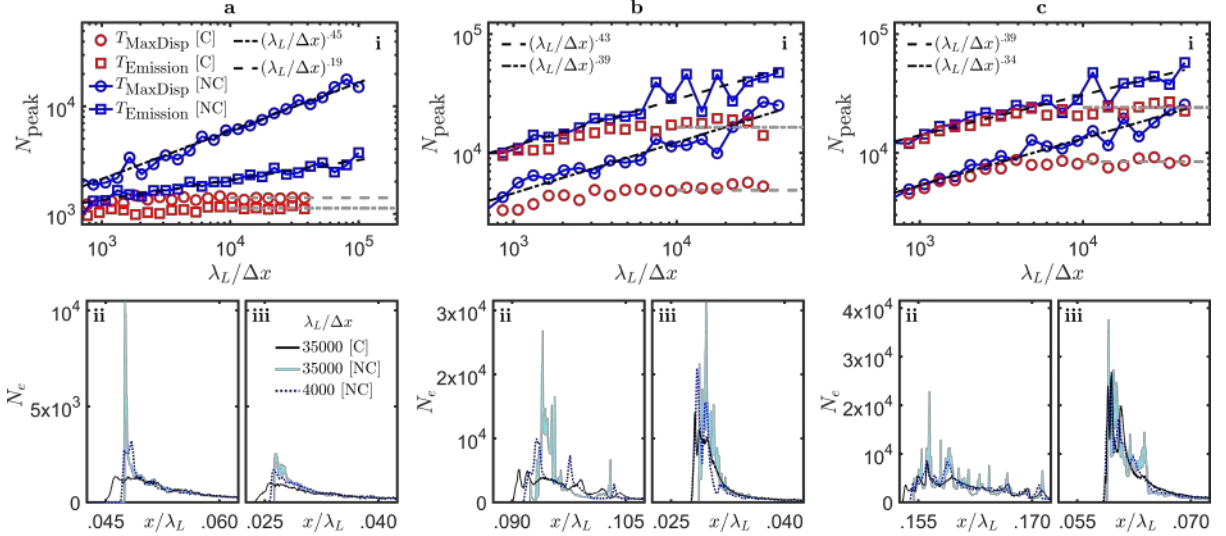


Figure 2.12: Effects of spatial resolution on the density distribution of the electron bunch modeled with and without collisions for (a) $\theta = 0^\circ$, $a_0 = 40$, $N_0 = 200$; (b) $\theta = 30^\circ$, $a_0 = 175$, $N_0 = 500$; (c) $\theta = 30^\circ$, $a_0 = 325$, $N_0 = 500$. For all simulations $C = 0.95$ and particles/cell = 50. (i) The peak density, N_{peak} , in collisionless [NC] (blue circles and squares) and collisional [C] (red circles and squares) simulations as a function of $\lambda_L/\Delta x$. For the collisionless cases, the black dashed lines show power-law fits to the peak density. For the collisional cases, a horizontal gray dashed line is plotted at the average value of N_{peak} for $\lambda_L/\Delta x > 10000$. (ii) The electron density spatial distribution near the time when the electron bunch has its maximum displacement from the plasma-vacuum interface (T_{MaxDisp}). Distributions from collisionless simulations are plotted in dark blue for $\lambda_L/\Delta x = 4000$ and cyan for $\lambda_L/\Delta x = 35000$. Distributions from collisional simulations are plotted in black at $\lambda_L/\Delta x = 35000$. (iii) Same as (ii) but the distribution is plotted at the time when the attosecond pulse is emitted (T_{Emission}).

simulations, we observe the presence of narrow density spikes contained within a single-cell of the numerical grid. The number of density spikes, as well as the peak density of those spikes, increase with higher spatial resolution. At the highest resolutions considered here, a large number of electrons ($N_0 > 20,000$) is compressed into a single cell of a width $\Delta x \approx 0.08 \text{ \AA}$. The peak density in the spikes is about an order of magnitude higher than the average density in the bunch. The appearance of these single-cell density spikes and the corresponding growth of the peak electron density results from the fact that closely spaced particles tend to accumulate in a single cell of the numerical grid.

To eliminate this unphysical effect, we consider collisional PIC model using the Monte-Carlo-based binary collision algorithm [95, 96, 98] incorporated in the EPOCH code. Monte Carlo binary collisions were first implemented into the particle in cell scheme by Takizuka and Abe in 1977 [94]. The Monte Carlo binary collision algorithm works by

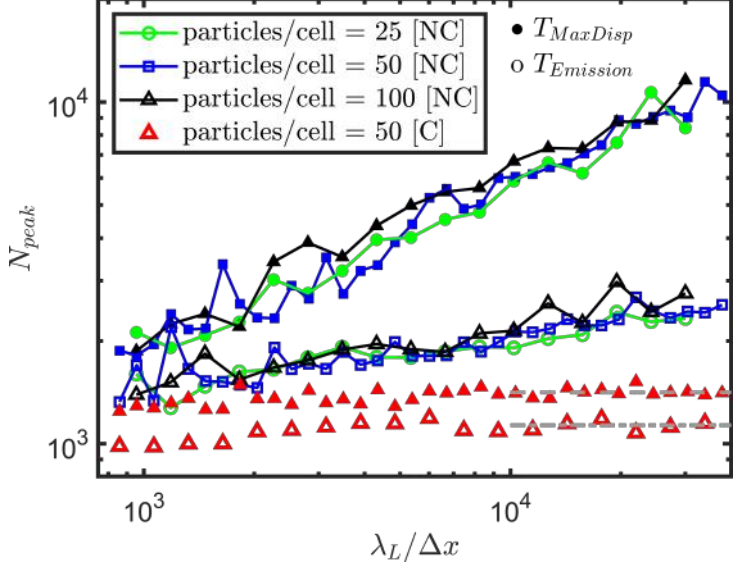


Figure 2.13: Peak density of the emitting electron bunch as a function of spatial resolution for simulations with collisions [C] and particles/cell = 50 (red triangles) and for simulations without collisions [NC] and particles/cell = 25 (green circles), 50 (blue squares), and 100 (black triangles). Shaded symbols denote the peak density at T_{MaxDisp} and open symbols denote the peak density at T_{Emission} . For all simulations $\theta = 0^\circ$, $a_0 = 40$, $N_0 = 200$, and $C = 0.95$. For the collisional cases, a horizontal gray dashed line is plotted at the average value of N_{peak} for $\lambda_L/\Delta x > 10000$.

randomly pairing all the particles within a cell and stochastically scattering the particles by randomly choosing a scattering angle from a Gaussian distribution function with variance determined from the Coulomb cross-section. Later work by Nanbu introduced an alternative distribution function to be used for the scattering [95, 96], which allows for much larger time steps than Takizuka and Abe's method. In the limit of small time step, both distribution functions have the same variance and have been shown to yield similar results [120].

In the last 15 years, several works have appeared that have extended the applicability of the collision algorithm within the PIC framework. In particular, these works studied collisions in the relativistic limit [97, 98, 121], self-consistently handling large angle scattering events [122], collisional ionization [98], and collisions between particles of different numerical weights [96, 99]. Today, many large scale PIC codes contain an algorithm for incorporating binary collisions, including EPOCH [74], Chicago [99], Calder [98], OSIRIS 2.0 [123], PICLS [97], SMILEI [124], and WarpX [102].

The results of collisional simulations are shown by red circles and squares in Fig.

2.12(i). With collisions, the peak density of the electron bunch initially follows the same power-law growth as a function of $\lambda_L/\Delta x$ as in the simulations without collisions, but eventually it converges to a fixed value at a spatial resolution which depends on the laser and plasma parameters, but is less than 10000 cells per fundamental wavelength in all cases. Additionally, in contrast to collisionless simulations where the increased spatial resolution leads to the appearance of multiple density spikes confined within single cells, collisional model yields smoother density distributions (solid black line in Figs. 2.12(ii) and 2.12(iii)) without the single-cell density spikes even at a high spatial resolution of $\lambda_L/\Delta x = 35000$.

The unphysical growth in the peak density of the electron bunch present in collisionless simulations does not change with the number of particles/cell present at the start of the simulation. In Fig. 2.13, the peak density of the electron bunch is plotted as a function $\lambda_L/\Delta x$ for simulations with collisions and particles/cell = 50 (red triangles) and for simulations without collisions and particles/cell = 25 (green circles), 50 (blue squares), and 100 (black triangles). All other parameters are the same as those used for the simulations presented in Fig. 2.12(a). Here we see that at T_{MaxDisp} and T_{Emission} the peak density of the electron bunch follows the same power-law growth independent of the number of particles/cell.

Remarkably, the single-cell density spikes in collisionless simulations do not affect the attosecond pulse intensities and harmonic spectra. The convergence of harmonic spectra, temporal intensity profiles, and attosecond pulse efficiency with increasing spatial resolution are shown in Fig. 2.14(a), 2.14(b), and 2.14(c), respectively. Note that the differences between the pulse profiles in Fig. 2.14(b) at low spatial resolutions are due to the fact that the harmonics are under-resolved and numerical dispersion has an effect on the pulse shape. However, we find that the attosecond pulse does not change with increasing resolution so long as there are at least ten cells per the shortest harmonic wavelength used to construct the attosecond pulse.

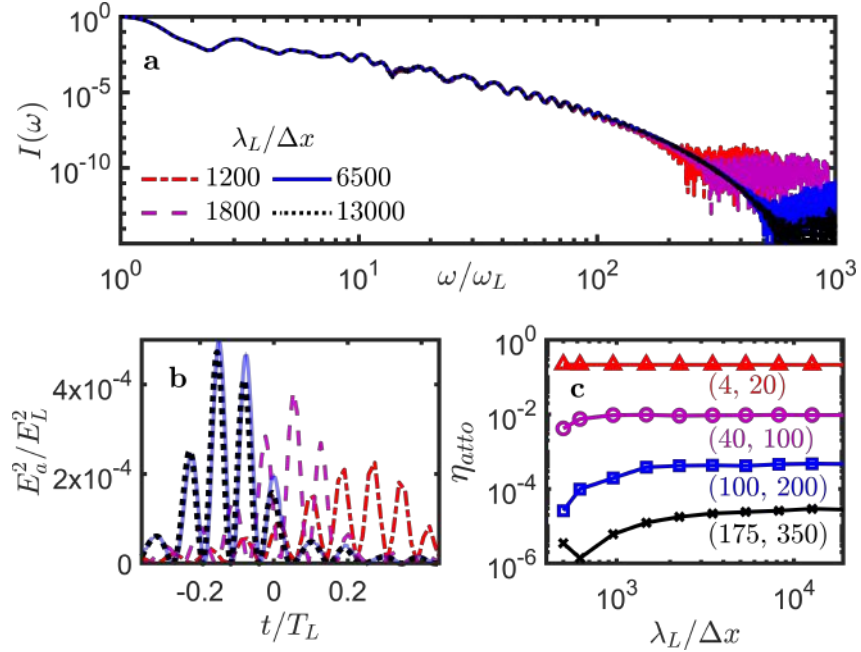


Figure 2.14: Effects of the spatial resolution on the (a) reflected spectra, (b) the attosecond pulse temporal profile, and (c) the attosecond pulse efficiency in collisionless simulations for the parameters $\theta = 0^\circ$, $a_0 = 20$, $N_0 = 100$, particles/cell = 100, and $C = 0.95$. In (b) the attosecond pulses were constructed using radiation in the frequency range $100 < \omega/\omega_L < 200$. In (c) the attosecond pulse efficiency was computed using radiation in the frequency range $(\omega_{LF}, \omega_{UF})$ where $\omega_{LF} < \omega/\omega_L < \omega_{UF}$.

2.3 Effects of collisions on electron bunch dynamics and attosecond pulse intensity

The attosecond pulse intensity is determined by the distribution of electrons near the time of emission, where we have shown differences between collisional and collisionless simulations. To understand the extent to which collisions impact the emitted attosecond pulses, the attosecond pulse generation efficiency with and without collisions is plotted in Fig. 2.15(a) for a frequency range of $80 < \omega/\omega_L < 300$ as a function of a_0/N_0 for different initial plasma densities. There are two regimes where simulations with and without collisions have the same attosecond pulse efficiency. The first is in the limit where $a_0/N_0 \approx 1$ for a fixed N_0 and the second is when $N_0 > 500$ for a fixed a_0/N_0 . Both of these limits require $a_0 > 100$, which is a higher laser field strength than that currently achievable in ongoing experiments. For parameter regimes away from these two limits, collisions lower the attosecond pulse efficiency, where the greatest reduction occurs for

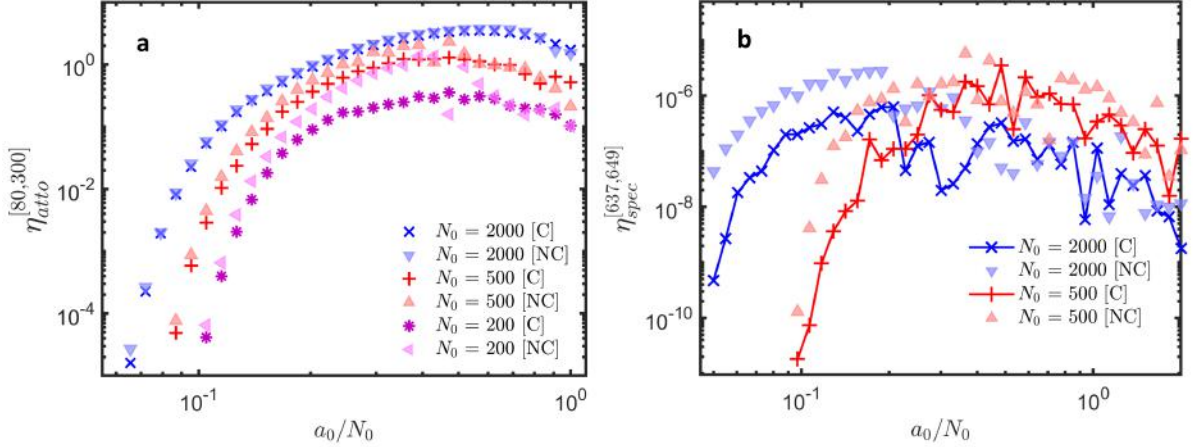


Figure 2.15: Attosecond pulse generation efficiency, η_{atto} , as a function of a_0/N_0 for three different values of N_0 , where the attosecond pulses were constructed using radiation in the frequency range (a) $80 < \omega/\omega_L < 300$ and (b) $637 < \omega/\omega_L < 649$. Shaded triangles indicate simulations without collisions [NC]. The other symbols indicate simulations with collisions [C]. For all simulations $\theta = 30^\circ$, particles/cell = 100, and $C = 0.95$. For (a) $\lambda_L/\Delta x = 4000$ and for (b) $\lambda_L/\Delta x = 8000$.

a_0/N_0 greater than 0.2, but less than 0.6. To understand these observations, we return to modeling the electron bunch dynamics prior to the attosecond pulse emission. In Fig. 2.15(b), the spectral efficiency in the frequency range $637 < \omega/\omega_L < 649$ is similarly plotted as a function of a_0/N_0 for $N_0 = 500$ and 2000 , where we see larger discrepancies than that observed in Fig. 2.15(a) between simulations with and without collisions for $a_0/N_0 < 0.2$, even for $N_0 = 2000$. However, as a_0/N_0 approaches 1, the spectral efficiency for simulations with and without collisions is identical.

In Fig. 2.16, the spectral efficiency for the frequency range $120 < \omega/\omega_L < 200$ is plotted as a function of a_0/N_0 for $N_0 = 500$ and $L = 0.10$. For $a_0/N_0 \lesssim 0.06$, the simulations with collisions have lower spectral efficiency compared to collisionless simulations. For $a_0/N_0 \gtrsim 0.06$, the spectral efficiency with and without collisions is the same. For simulations with an exponential pre-plasma gradient, the most efficient interactions take place for values of $a_0/N_0 < 0.1$ since the laser effectively interacts with an electron number density value lower than N_0 [27, 54, 125], which represents the upper shelf density [$N_e = N_0 e^{x/L}$ for $x \leq 0$]. This is in contrast to interactions with a steep plasma surface, for which the most efficient interactions require $a_0/N_0 \approx 0.5$ at $\theta = 30^\circ$.

In Fig. 2.17, the spatial distribution of the electron density at particular times before

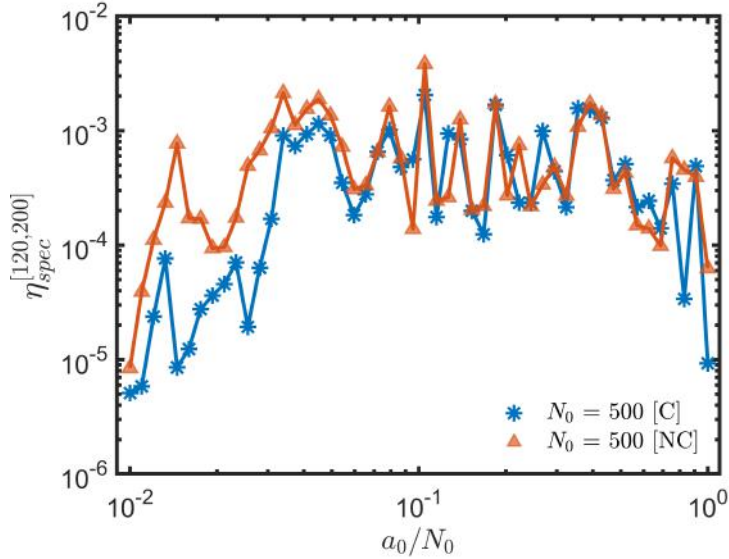


Figure 2.16: Spectral efficiency (η_{spec}) simulated with collisions [C] and with no collisions [NC] in the frequency range $120 < \omega/\omega_L < 200$ as a function of a_0/N for a finite pre-plasma gradient scale length. Relevant simulation parameters: $\lambda_L/\Delta x = 1500$, particles/cell = 5000, $D = 0.10$, $L = 0.10$, $\theta = 30^\circ$, $N_0 = 500$, $C = 0.95$, $\tau/T_L = 1$, $\phi_{CEP} = 90^\circ$.

the emission of the attosecond pulse is plotted for simulations with and without collisions at four different values of a_0/N_0 . For $a_0/N_0 < 0.35$, collisions have the effect of lowering the peak density of the electron bunch, especially near the time when the electron bunch is at its maximum displacement from the initial plasma-vacuum interface. As a_0/N_0 is increased to values $\gtrsim 0.35$, the electron density spatial distributions become identical at all instants of time, apart from the single-cell density spikes present in collisionless simulations for which we have already shown have negligible effect on the emitted attosecond pulses. Also shown in Fig. 2.17 are the spectra and attosecond pulses of the reflected electric field. For all values of a_0/N_0 , the simulations with and without collisions produce identical harmonic intensity for low frequencies. However, for $a_0/N_0 \lesssim 0.50$, the spectra produced from simulations with collisions have a lower frequency cut-off compared to collisionless simulations, which corresponds to a reduction in attosecond pulse intensity.

Within the framework of the CSE model, the location of the frequency cut-off can be determined by analyzing the distribution of the relativistic Lorentz factors of the emitting electrons within the electron bunch [27, 112]. Analytically, the reflected spectral intensity

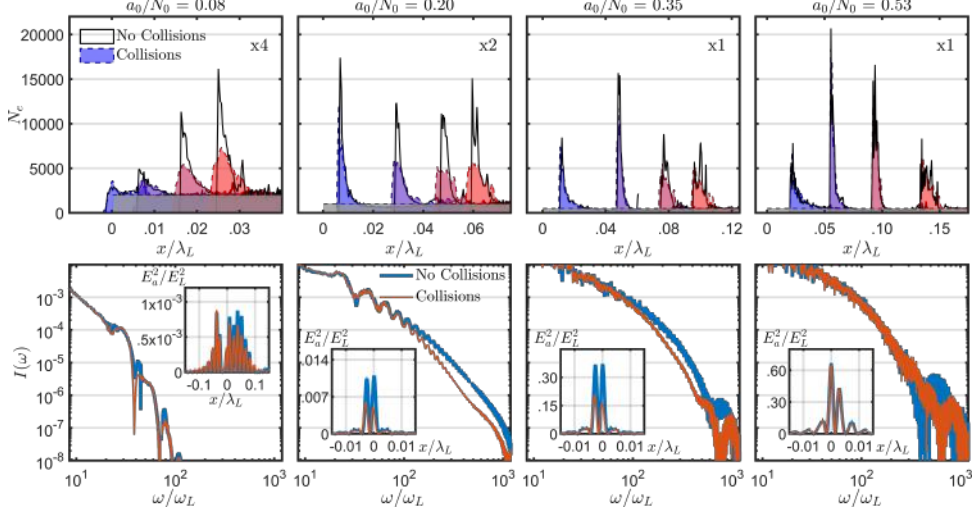


Figure 2.17: Comparison of the electron density spatial distribution, the reflected spectral intensity, and the emitted attosecond pulse for simulations with and without collisions for the parameters $\theta = 30^\circ$, $N_0 = 500$, $\lambda_L/\Delta x = 8000$, particles/cell = 150, $C = 0.95$, and varied a_0 . The top row shows the evolution of the electron bunches from T_{MaxDisp} through T_{Emission} . The distributions in the left two plots have been scaled up by the factor listed in the upper right corner of the plot to allow for comparison of the profiles across all four values of a_0/N_0 . The bottom row plots the reflected spectral intensity for both the collisional and collisionless cases. The inset plots on the bottom row compare the attosecond pulses which were constructed using radiation in the frequency range $30 < \omega/\omega_L < 100$ for $a_0/N_0 = 0.08$ and $100 < \omega/\omega_L < 300$ for all other cases.

can be calculated with the following equation [108]:

$$I(\omega) \propto |\tilde{f}(\omega)|^2 \omega^{-4/3} \left\{ \text{Ai}' \left[(\omega/\omega_\gamma)^{2/3} \right] \right\}^2 \quad (2.24)$$

In equation 2.24, $\omega_\gamma = \sqrt{8\alpha}\gamma^3$, where α is a constant calculated from the electron trajectories, $\gamma = 1/\sqrt{1-v^2/c^2}$ is the Lorentz factor of the electrons at the time of emission, Ai' is the derivative of the Airy function of the first kind, and $\tilde{f}(\omega)$ is the Fourier transform of the electron bunch shape function. It has been shown, across a wide range of laser and plasma parameters, that the shape of the electron bunch can be approximated as a step function since the peak Lorentz factors of the electrons abruptly jump to their maximum value at the leading edge of the distribution [27]. As a consequence, when the emitted wavelengths have a comparable size to the emitting electron bunch width, a transition of spectral scaling from the original ω^{-p} power-law to ω^{-p-2} takes place as a result of destructive interference between radiation emitted from different electrons

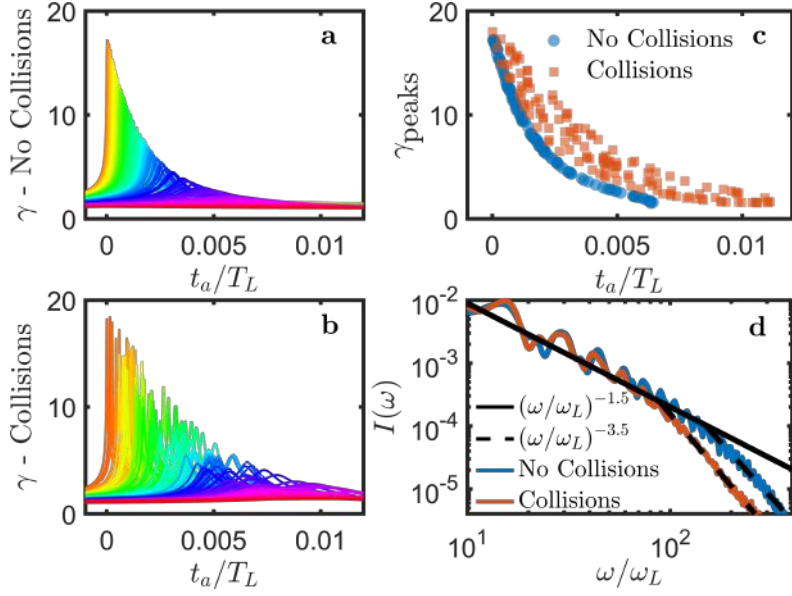


Figure 2.18: Comparison of the distribution of Lorentz factors for emitting electrons within the electron bunch for simulations with and without collisions (a) Distribution of the relativistic Lorentz factors of emitting electrons as a function of the advanced time coordinate for a collisionless simulation. (b) Same as (a) but with collisions simulated. (c) Shows only the peak value of the Lorentz factors from (a) and (b) illustrating the spread of the emitting electron bunch when collisions are simulated. (d) Reflected spectra of the two cases showing the earlier bunch width-induced frequency cut-off when collisions are simulated. The simulation parameters are $\theta = 45^\circ$, $a_0 = 80$, $N_0 = 200$, $\lambda_L/\Delta x = 10000$, particles/cell = 100, and $C = 0.95$.

within the electron bunch.

In Fig. 2.18, the distribution of Lorentz factors for individually emitting electrons within the electron bunch are plotted as a function of the advanced time coordinate for a collisionless [Fig. 2.18(a)] and collisional [Fig. 2.18(b)] simulation. Here we see that, although the electrons within the emitting electron bunch have similar peak Lorentz factors in both cases, the overall spread in time of the peak Lorentz factors is greater when collisions are modeled [Fig. 2.18(c)]. This increased spread in the peak of the Lorentz factors results in an earlier frequency cut-off for the case with collisions as illustrated in Fig. 2.18(d). If we define the bunch width induced frequency cut-off (ω_b) to be the frequency at which the spectral intensity drops by a factor of $1/e$ below its initial power-law scaling, then $\omega_b/\omega_L \approx 250$ in the collisionless simulation and $\omega_b/\omega_L \approx 150$ in the collisional simulation.

In summary, we present results from one-dimensional particle-in-cell simulations of

relativistic laser-solid interactions, concentrating on the sub-cycle dynamics of electron bunches and the emitted attosecond pulses as a function of the laser intensity, plasma density, laser angle of incidence, and spatial and temporal resolution of the simulations. Specifically, we show that for initial conditions of the laser and plasma parameters which yield inefficient attosecond pulses, the time of attosecond pulse emission occurs at $t/T_L \approx 0.5$, at which point the electron bunch has expanded close to the original density of the plasma, resulting in weak attosecond pulse intensities. In contrast, in parameter regimes where the highest attosecond pulse efficiencies are obtained, the attosecond pulses are emitted at a point in time when the electron bunch has its highest peak density, which occurs at times exceeding $0.5T_L$ as a result of the increased displacement of the electron bunch from the initial plasma-vacuum interface.

We find that in collisionless particle-in-cell simulations, there exists a spatial resolution dependent growth in the peak density of the electron bunch, which does not plateau even at extremely high resolutions. Despite the appearance of these sharp density spikes confined to be within a single-cell of the numerical grid, the attosecond pulses and spectra converge with increasing spatial resolution for a given frequency range.

When binary collisions are added to the PIC model, the peak electron bunch density initially exhibits the same growth, but eventually converges to a fixed value as the spatial resolution is increased. In general, modeling collisions lowers the attosecond pulse intensity except in regimes where $a_0/N_0 \gtrsim 0.6$ at a fixed N_0 and where $N_0 \gtrsim 500$ at a fixed a_0/N_0 . The reduction in attosecond pulse intensity for collisional simulations is a consequence of the increased spread in time of the peak Lorentz factors of the emitting electrons, which leads to an earlier frequency cut-off than that obtained in collisionless simulations.

Chapter 3

Plasma Optics for Ultra Intense Laser Applications

3.1 Introduction

The primary focus of this work is on harmonic generation from plasma mirrors, for which the most efficient interactions require relativistic intensities incident on a nearly flat surface. These requirements place stringent requirements on the laser's temporal envelope and picosecond contrast as we need a short pulse to get high intensity and sufficiently high contrast to ensure that the surface of the target is not spoiled before the main pulse arrives. In this chapter we demonstrate the application of two plasma-based optics for manipulating intense light, focusing on measuring the temporal envelope and contrast of the laser before and after the optic. In section 3.2, we show that a plasma mirror irradiated at near-normal incidence at $1 \times 10^{16} \text{ W/cm}^2$ reflects the laser in the specular direction with up to 80% efficiency and reduces any prepulse intensity by two-orders of magnitude. We find that the plasma mirror has negligible effect on the pulse duration and envelope shape of the main laser. In section 3.3, we show that a plasma gratings [10, 126], formed by crossing two 400nm pump beams inside a gas cell filled with air, will diffract an 800nm probe laser for several picoseconds after the formation of the grating. The diffraction process enhances the temporal contrast by over 5 orders of magnitude

and has only a slight effect on the temporal pulse envelope and pulse duration.

3.2 Plasma mirrors for reflection and temporal contrast improvement

3.2.1 Experimental set-up

The schematic set-up for realizing a contrast cleaning plasma mirror is depicted in figure 3.1. The laser (800nm, 10Hz, 25fs, 10-400mJ) enters the vacuum chamber after compression at the upper right. It is then focused using a 1m focal length ($f/25$) spherical mirror onto the surface of a glass target (BK7), reaching high enough intensities so that the laser will ionize the front surface of the target. The resulting overdense plasma target then specularly reflects the laser, which is subsequently recollimated with a second spherical mirror, and then sent outside of the experimental chamber to a series of diagnostics. We take images of the near-field and far-field beam profiles as well as make autocorrelation and pulse duration measurements. Data is collected in a 'single-shot' mode, where the target is rotated between shots to provide a fresh surface.

Since we are using spherical mirrors at an oblique angle of incidence, we will introduce some astigmatism into the laser beam [127]. In figure 3.2, we plot the measured beam profiles incident on PM1's surface as a function of the target position, z . The measurements were done in air at alignment power using a camera placed inside the experimental chamber. The horizontal and vertical astigmatic foci are apparent as z passes through the laser's best focus, which occurs at $z \approx 42\text{mm}$. These images were used to calculate the average intensity on the surface of PM1 as a function of z for a given incident pulse energy. In principle, we could remove the astigmatism by using an off-axis parabolic (OAP) mirror instead of spherical mirrors. However, these OAPs are generally more expensive and debry ejected from PM1 limits their lifetime.

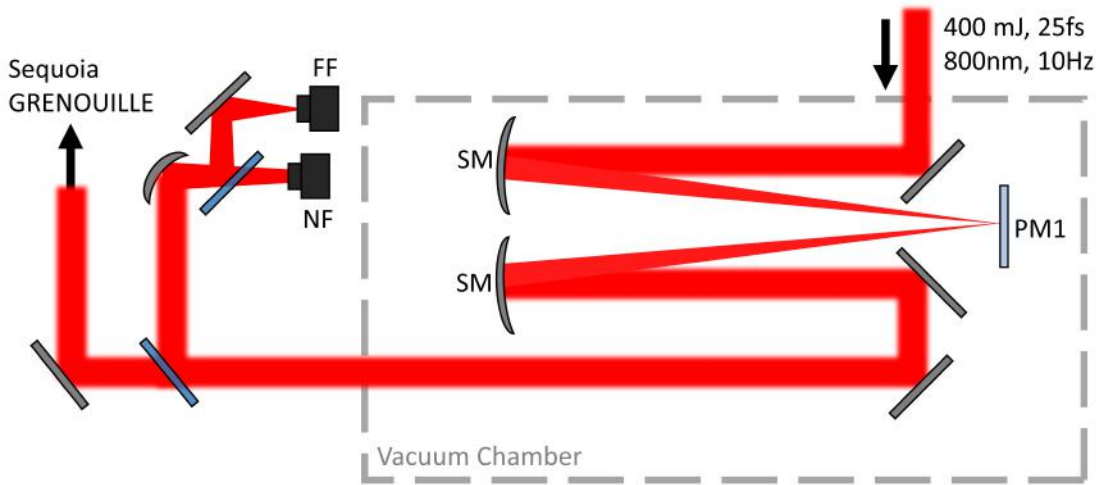


Figure 3.1: Schematic set-up of a plasma mirror used to temporally clean the picosecond contrast of the laser. The laser enters the vacuum chamber from the upper right and is subsequently focused onto a piece of BK7 glass using a spherical mirror with a 1m focal length. After specularly reflecting from PM1, the laser is recollimated with a second spherical mirror and sent outside of the experimental chamber for several diagnostic measurements, including near-field and far-field imaging, autocorrelation (Sequoia - Amplitude Technologies), and pulse duration (GRENOUILLE - home-built). Key: FF = far-field, NF = near-field, SM = spherical mirror, PM = plasma mirror.

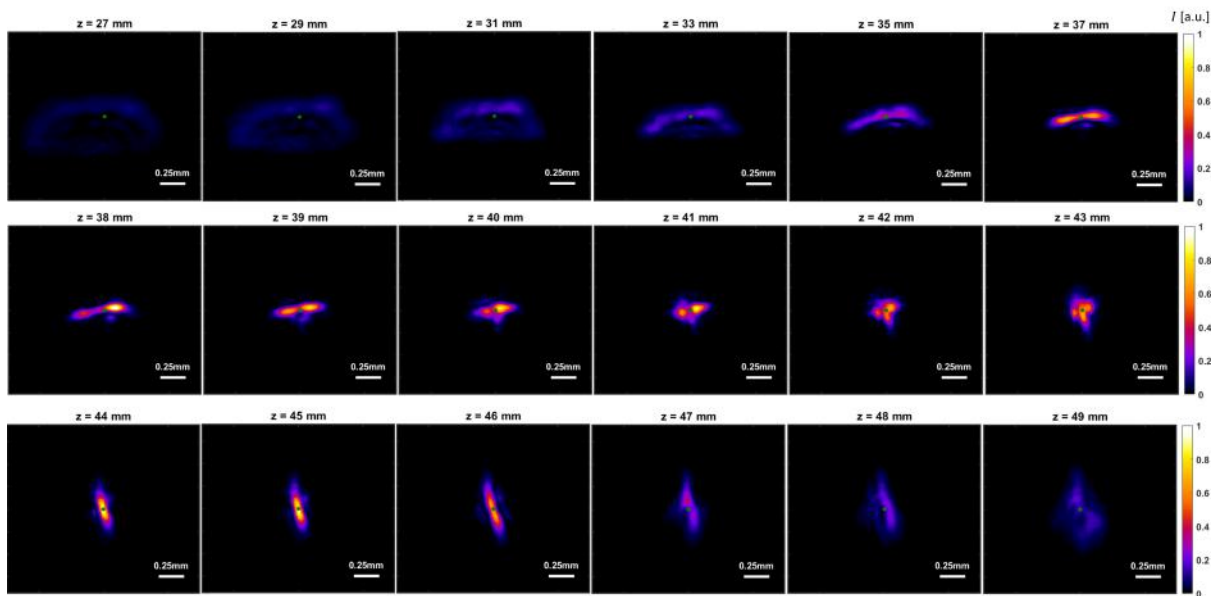


Figure 3.2: Measured beam profiles on the surface of PM1 as a function of the target position, z . The astigmatic profile at focus arises because the beam is being focused by a spherical mirror at oblique incidences. The green dot denotes the energy weighted midpoint of the profile.

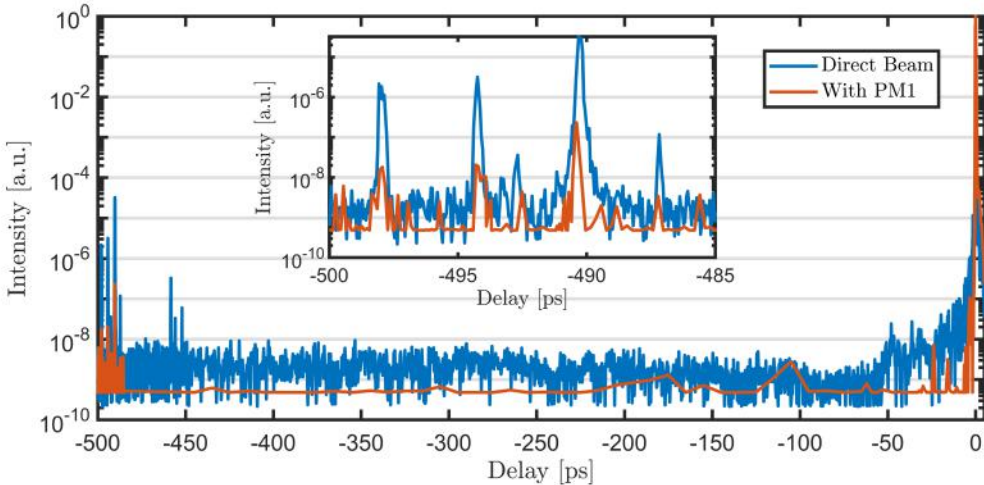


Figure 3.3: Temporal contrast measurement of the laser on a picosecond timescale taken before and after reflection from PM1. (inset) A group of prepulses located at 500ps which are seen to drop by 2 orders of magnitude after reflection from PM1.

3.2.2 Contrast and reflectivity measurements

The primary goal of PM1 is to clean the laser of unwanted pre-pulses and amplified stimulated emission so that the intensity of the pre-pulses are not sufficiently high as to spoil the surface of subsequent targets before the arrival of the main pulse. To get rid of the pre-pulses, the incident laser is focused to an intensity such that the prepulses are too weak to efficiently ionize the surface of PM1, and so pass right through the glass, while the main pulse fully ionizes the surface of PM1 and will be efficiently reflected. In figure 3.3, the temporal contrast of the laser before (blue curve) and after (red curve) reflection from PM1 is shown for up to 500ps before the arrival of the main pulse. The inset shows a group of prepulses at -500ps. After reflection from PM1, the contrast of the laser system is improved by at least two orders of magnitude [128].

In principle, the contrast of the laser system can be increased by including additional plasma mirrors. However, each reflection means a loss in energy of the main beam. In figure 3.4(a), we plot the percent reflectivity of the laser as a function of z at a fixed energy of 63mJ (blue dots) and 125mJ (red dots). Initially, as the plasma mirror is brought closer to best focus the reflected energy increases until about $z = 31\text{mm}$, where up to 70% reflectivity is obtained. After this peak, the reflected energy rapidly drops as the plasma mirror is brought even closer to best focus ($z \approx 42\text{mm}$), where the reflected

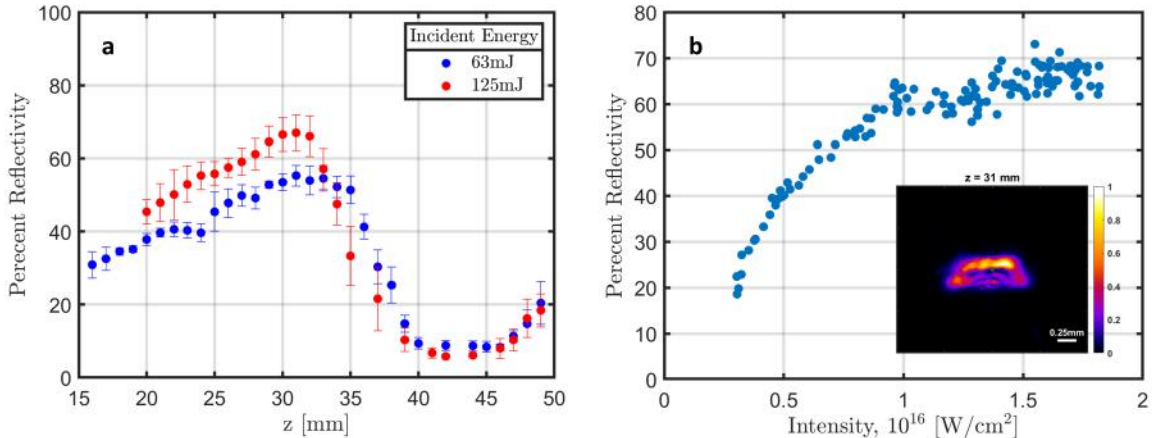


Figure 3.4: Reflectivity from PM1 as a function of z at fixed energy and as a function of energy at fixed z . (a) The incident energy was set to 63mJ and 125mJ and the position of the plasma mirror was scanned through the focus. (b) The plasma mirror was set to $z = 31$ mm and the energy was scanned from 20mJ through 400mJ. The inset shows the measured focal spot at $z = 31$ mm. The reflected energy takes into account the losses from the four additional mirrors used to focus the beam on PM1 and to recollimate the beam. The reflectivity from PM1 itself can reach up to 80% [128].

energy is less than 10%. At these intensities, the pre-pulses are intense enough to ionize the surface and the resulting plasma expansion spoils the optical-quality surface well before the main pulse arrives. Finally, as z is increased further past 45mm, we see the reflected energy begin to increase again since the laser has passed the focal spot and begins to expand again.

In figure 3.4(b), the reflected energy from PM1 as a function of intensity at fixed $z = 31$ mm is plotted. To change the intensity on target, the energy entering the chamber was varied from 60mJ to 400mJ. The inset shows the on target beam profile. At this z position, the reflectivity varies from 20% at 60mJ up to 70% at 400mJ. Although we can in principle vary z and energy simultaneously to get maximum reflectivity for all incident energies, adjusting z affects the downstream alignment which cannot be easily fixed when the chamber is at vacuum. Therefore, for all remaining experiments, we will fix the z position of PM1 at 31mm and use the curve from figure 3.4(b) as a calibration curve. Note that in both figure 3.4(a) and 3.4(b), the reflected energy takes into account the losses from the four additional mirrors used to focus the beam on PM1 and to recollimate the beam. The reflectivity from PM1 itself can reach up to 80% [128].

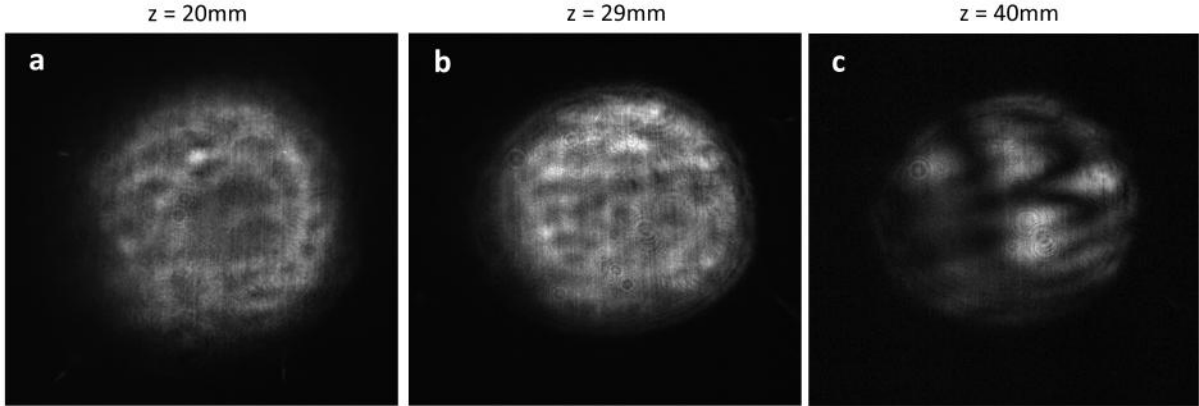


Figure 3.5: Measured spatial profiles of the beam after reflection from PM1 as the plasma mirror is scanned through the focus. The incident laser energy was 125mJ.

In figure 3.5, the spatial profile of the beam after interacting with PM1 at $z = 20\text{mm}$, 29mm , and 40mm is shown. Here we see that the profiles at $z = 20$ and 29mm look similar but the reflected energy is higher when $z = 29\text{mm}$. In contrast, the reflected spatial profile of the beam when the plasma mirror is near the best focus is substantially distorted, resulting in the drop in reflectivity that was observed in figure 3.4.

3.2.3 Pulse envelope measurements with GRENOUILLE

We have showed that the contrast cleaning plasma mirror can reflect intense light with 80% efficiency, reduce unwanted prepulse intensity by at least two orders of magnitude, and preserve (or even improve, see section 4.3) the spatial quality of the laser. However, it is also important that the plasma mirror does not substantially distort the temporal profile of the main driving laser. For the remainder of this section we characterize the temporal profile of the laser after reflection from PM1, showing that a contrast cleaning plasma mirror does not dramatically change the temporal profile or pulse width of the laser.

To measure the temporal profile of the laser, we use a home-built GRENOUILLE apparatus [129]. GRENOUILLE, which is an acronym standing for GRating-Eliminated No-nonsense Obeservation of Ultrafast Incident Laser Light E-fields, is a second harmonic generation variant of Frequency Resolved Optical Gating (FROG), a class of techniques used to fully characterize ultrashort laser profiles [130]. The main idea behind a FROG

measurement is to first split the laser into two beams, and then recombine the beams in a nonlinear crystal with an adjustable delay. The resulting spectrum is recorded for several different delays of the two pulses, which yields a spectrogram (also called a FROG trace). The major breakthrough with the FROG technique is that this trace (which is essentially a spectrally resolved autocorrelator signal) allows you to back out the intensity and phase of the original pulse, something that an autocorrelation alone cannot do. See chapter 5 of reference [130] for a complete discussion on the history of measuring ultrafast events and how the FROG trace recovers the complete pulse information. GRENOUILLE is a single-shot variant of FROG, which is particularly convenient when working with plasma mirrors. Furthermore, GRENOUILLE also provides measurements of certain classes of spatial aberrations that plague many high-power laser systems, such as pulse-front tilt [131], or spatial chirp [132].

In figure 3.6, we show an example of the recovered temporal profile and phase [figure 3.6(a)], spectral intensity and phase [figure 3.6(b)], and GRENOUILLE trace [figure 3.6(c)] from a GRENOUILLE measurement of the laser entering the experimental chamber. This measurement ensures that the laser entering the experimental chamber is unchirped and nearly Fourier transform limited. Additionally, the symmetric trace indicates that there is no measurable spatial chirp or pulse front tilt after compression, as these aberrations would appear as a shear in the trace.

There are some limitations to the GRENOUILLE apparatus which the researcher should be aware of. For example, our GRENOUILLE device can theoretically measure pulses as short as 20fs [129], which is sufficient for the bandwidth of the laser after the compressor, but not for anything broader. In figure 3.7, we plot the recovered temporal profile and phase [figure 3.7(a)] and spectral intensity and phase [figure 3.7(b)] of the laser beam after it has propagated through 1m of 2mbar Helium gas with an energy of 150mJ. Under these conditions, the laser experiences some temporal modulation and spectral broadening compared to the laser immediately after the compressor. The solid black line plotted in figure 3.7(b) is the spectrum as measured by a high resolution spectrometer (Ocean Optics 2000). Here we see that the GRENOUILLE algorithm produces

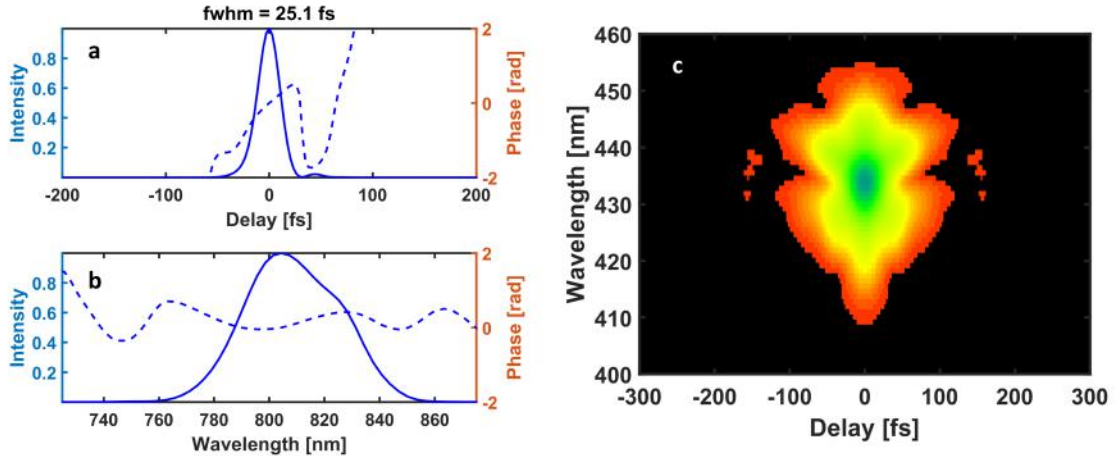


Figure 3.6: Pulse duration measurement of the compressed laser entering the experimental chamber using a home-built GRENOUILLE apparatus [129]. (a) Recovered temporal profile of the beam. (b) Recovered spectrum of the laser obtained by Fourier transforming the pulse from (a). (c) The recovered FROG spectrogram.

a smoothed spectra and fails to capture the spectral peak at 760nm. Additional problems with GRENOUILLE can arise since it is a single-shot device, which means that it relies on mapping the spatial profile of the beam into delay to construct the entire trace. This means that the beam must be free of spatial aberrations before the measurement is made as discussed above.

With the basics of making a GRENOUILLE measurement now explained, we can proceed to characterizing the pulse duration before and after interacting with PM1. However, since it is known that PM1 introduces some astigmatism into the beam, it is challenging to make a direct comparison between the beam entering the chamber with the one after reflecting from PM1. Instead we choose to compare the GRENOUILLE traces with PM1 engaged at alignment power (i.e. no plasma) and with PM1 engaged and 100mJ in the incident laser (i.e. at the highest reflectivity with plasma). These two conditions are illustrated in figures 3.8 and 3.9 for the laser beam at alignment power and 100mJ, respectively. Here we see that the temporal profile is nearly identical for the two cases and that the plasma hardly affects the pulse duration which is 25.8fs without plasma and 27.3fs with the plasma.

Finally, in figure 3.10, we plot the reflectivity [figure 3.10(a)] and recovered FWHM

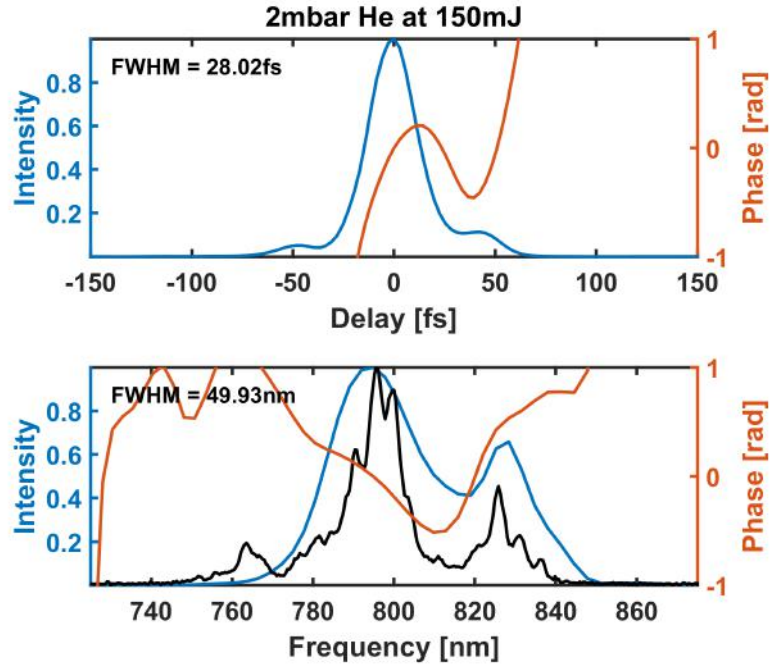


Figure 3.7: GRENOUILLE trace of the laser after about 1m of propagation through 2mbar of Helium gas, which induces some spectral modulation and broadening. The black spectrum was recorded by a commercial spectrometer (Ocean Optics 2000) and the blue spectra was recovered by the GRENOUILLE algorithm. The GRENOUILLE device successfully captures the global structure of the spectra, but it fails to capture the finer details of a more complicated spectra. The failure of the device to capture the peak at 760nm is due to the second harmonic filter which is only sufficient to capture the bandwidth of the main laser.

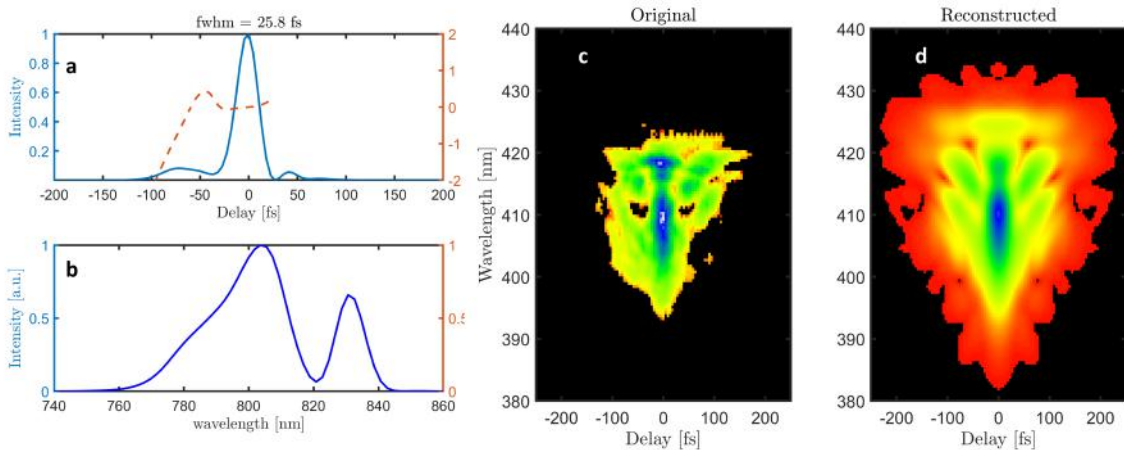


Figure 3.8: Pulse duration measurement of the laser after propagating through the experimental chamber along the beam diagnostics line with PM1 engaged and the laser energy set to alignment power so that no plasma is formed. (a) Recovered temporal profile of the beam. (b) Recovered spectrum of the laser obtained by Fourier transforming the pulse from (a). (c) The original FROG spectrogram that is input into the FROG algorithm. (d) The recovered FROG spectrogram.

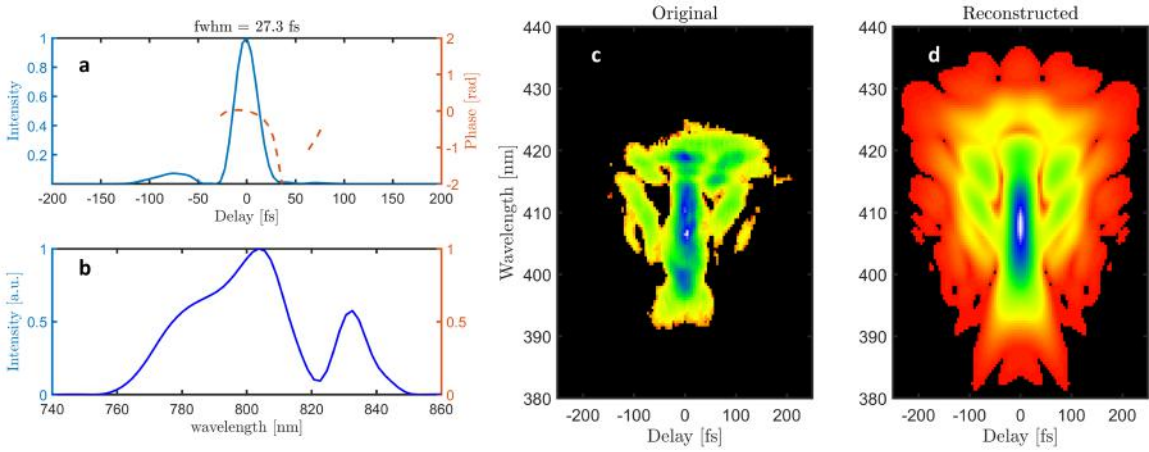


Figure 3.9: Pulse duration measurement of the laser after propagating through the experimental chamber along the beam diagnostics line with PM1 engaged and the laser energy set to 100mJ. (a) Recovered temporal profile of the beam. (b) Recovered spectrum of the laser obtained by Fourier transforming the pulse from (a). (c) The original FROG spectrogram that is input into the FROG algorithm. (d) The recovered FROG spectrogram.

of the reflected pulse [figure 3.10(b)] as a function of PM1z for incident energies of 50mJ (blue markers) and 100mJ (red markers). Even though the reflectivity increases as the plasma mirror is brought closer to best focus, the pulse duration remains fixed as a function of PM1z for both energies. Note that these measurements were made when the laser from the compressor was slightly broadened (35fs instead of the nominal 25fs).

3.3 Plasma gratings for diffraction and temporal contrast improvement

The plasma mirror is one type of plasma-based optic that is used to specularly reflect intense light and temporally clean the laser beam at the picosecond timescale. With 80% reflection efficiency and two orders of magnitude in contrast improvement, plasma mirrors are the standard method for cleaning high-power laser beams. A particularly favored design is the double plasma mirror which yields about 50% reflectivity and four orders of magnitude in contrast improvement [24]. In principle, plasma mirrors can operate at 1kHz repetition rate [133], but in practice they are often operated at 1Hz or

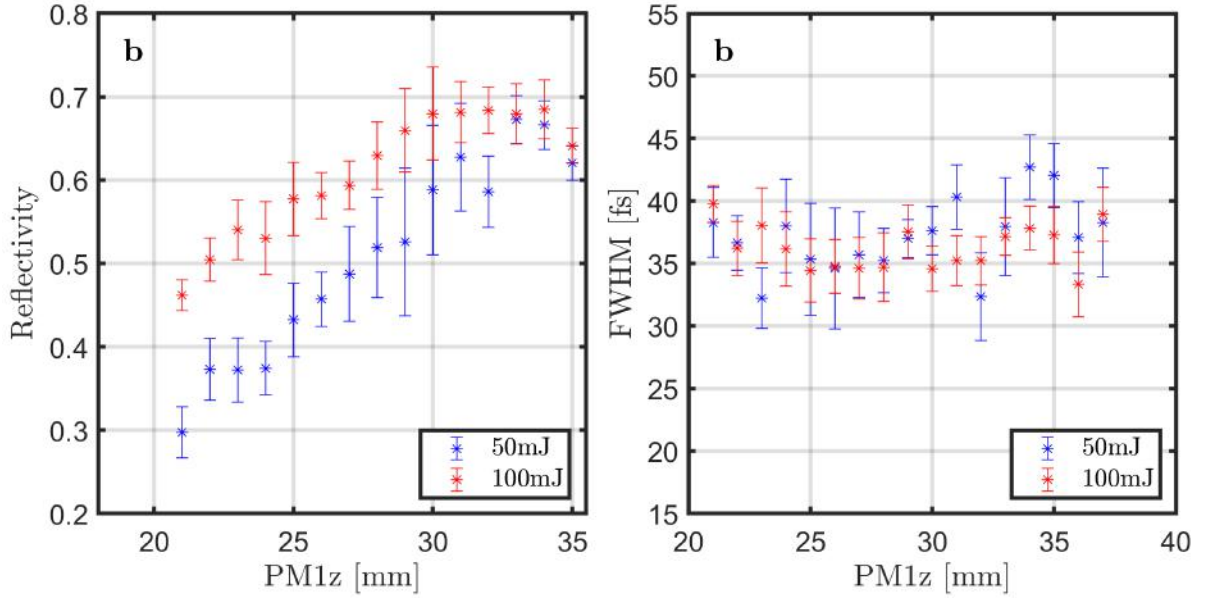


Figure 3.10: Reflection efficiency (a) and pulse duration (b) as a function of PM1z for two different incident energies from the contrast cleaning plasma mirror. Although the reflectivity increases as the plasma mirror is brought closer to focus, the reflected pulse duration remains roughly fixed.

less since it is challenging to replace the damaged target surface at such a high repetition rate and also plasma mirrors have a finite lifetime (the size of the glass target). In this section, a plasma grating is proposed to overcome these limitations of plasma mirrors, where we experimentally show that a diffracted probe from a plasma grating improves temporal contrast by more than five orders of magnitude and that the grating is stable when operated continuously at 10Hz for more than one hour.

3.3.1 Experimental set-up

The experimental set-up for constructing a plasma grating is depicted in figure 3.11. Two pump lasers at 400nm (blue lines) are focused into a gas cell filled with air at a pressure between 100-2000mbar. The 400nm pumps each have about 0.3mJ of energy and are crossed at an angle of 0.7° . The interference of the overlapped two pumps in space and time is shown in the lower inset of figure 3.11. Additionally, a (cotimed) 800nm pump with about 2mJ of energy is focused into the chamber at 2.3° . Although this third pump beam is not strictly necessary to obtain a diffracted signal, we found that the additional

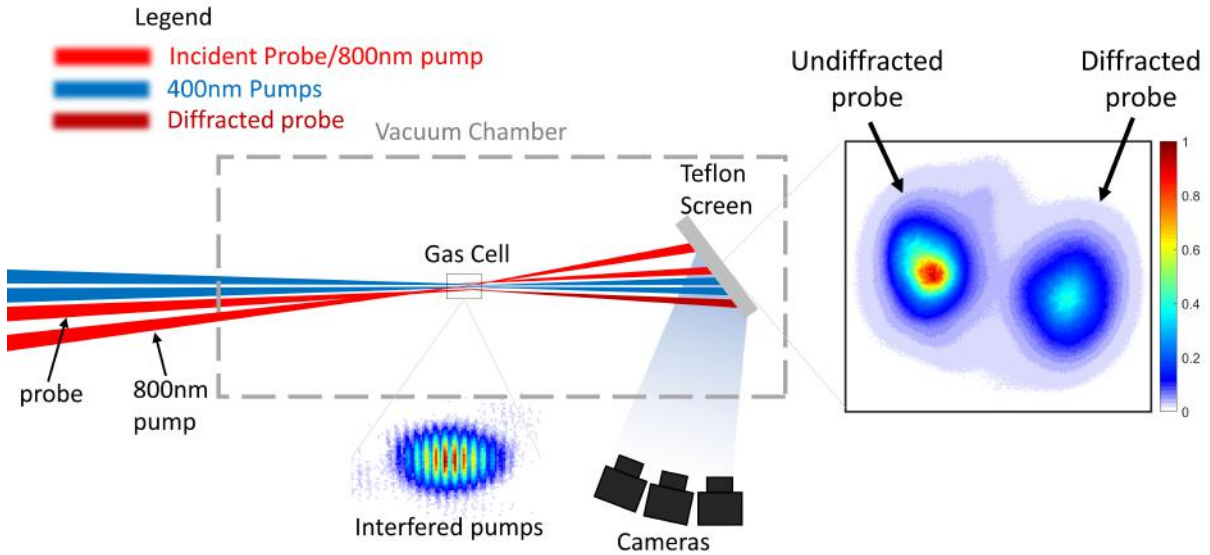


Figure 3.11: Schematic diagram of a plasma grating experiment. Three pump beams (two at 400nm and one at 800nm) are overlapped in space and time inside a gas cell filled with CO₂ or air, creating the interference pattern as illustrated in the inset. A delayed probe beam at 800nm is then sent in to diffract off the plasma grating. The right panel shows the undiffracted probe and the diffracted probe which are images from a teflon screen.

energy brought by this laser helped to enhance the ionization grating, improving the diffraction efficiency by an order of magnitude. A delayed 800nm probe beam with 1.5mJ of energy is then sent into the gas cell at 1.4° (the Bragg angle) which diffracts from the plasma grating as shown in the schematic. A teflon screen placed behind the gas cell is imaged with cameras placed outside the vacuum chamber. An example of the imaged undiffracted and diffracted probe beam are shown at the inset on the right.

3.3.2 Diffraction and grating stability

In figure 3.12, we plot the normalized diffracted signal efficiency as a function of the probe delay. The x-axis is set so that a delay of 0ps corresponds to the peak diffracted signal, which is about 0.5ps after the grating starts to form. Here we see the grating persist for about 1ps after peak diffraction. The periodic spikes in the diffracted signal corresponds to the rotational revival half period of Nitrogen which is 4ps [134]. This delay scan was made with air inside the gas cell, but grating lifetimes on the order of 100ps are feasible with different gases such as CO₂ [135].

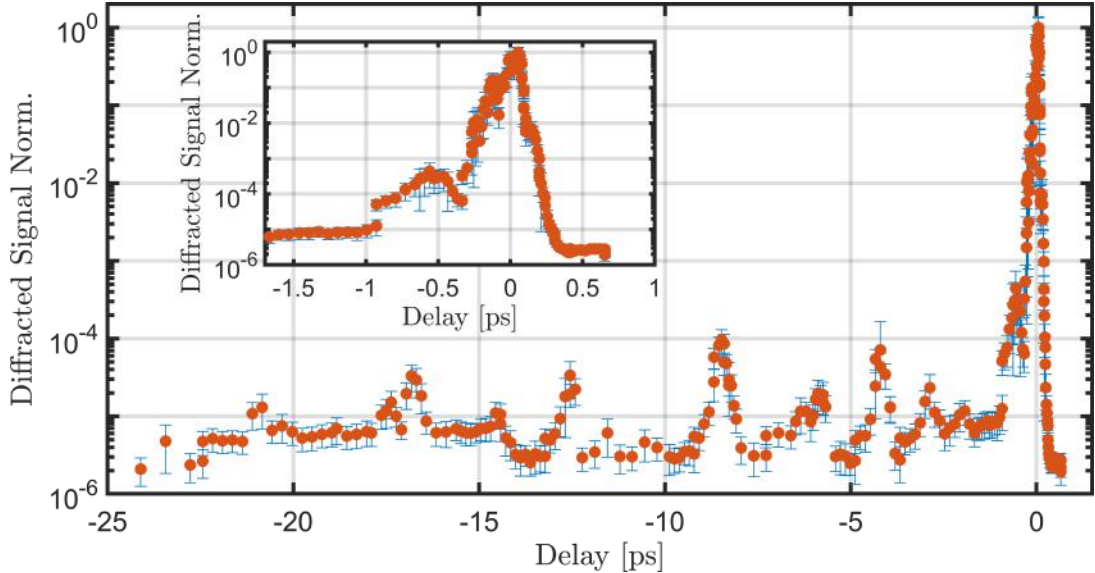


Figure 3.12: Normalized diffraction signal as a function of the probe delay with respect to the formation of the plasma grating. The grating in this experiment had a life time of a few picoseconds. The periodic spikes correspond to the rotational revival half period of Nitrogen which is 4ps [134].

With the probe delay stage set to maximum efficiency, we then set out to measure the stability of the diffraction signal as a function of time. The diffracted signal (normalized to its average value) is plotted as a function of time in figure 3.13. The system was run at 10Hz and images were recorded at 5 Hz (i.e. every other shot). Here we see that the average diffraction efficiency remained stable over the course of one hour. The high shot variance is largely due to the variance in the laser performance, which can have a dramatic affect on the second harmonic generation process that goes into creating the pump beams. Some of the variance is also a result of mechanical vibrations from vacuum pumps.

3.3.3 Contrast and pulse envelope measurements

As with a plasma mirror, it is important to fully characterize the effects that the plasma optic, in this case a grating, has on the temporal profile of the laser. In figure 3.14, we plot the laser's contrast on a picosecond timescale for both the undiffracted (blue) and diffracted (red) probe beam. The undiffracted probe beam's temporal contrast was intentionally spoiled by introducing a prepulse at about -60ps using a microscope slide

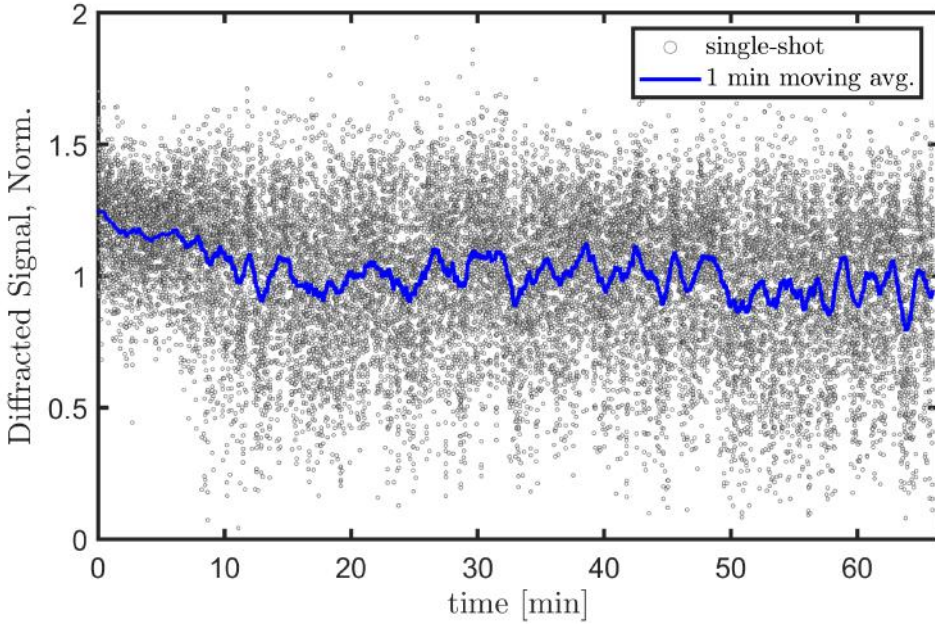


Figure 3.13: Single-shot diffraction efficiency (normalized) recorded for over 60 minutes. The system was run at 10 Hz, but the camera recorded at 5Hz. The blue line shows a 1minute moving average.

placed in the probe's beam path. Here we see that the diffracted laser beam's temporal contrast is improved by over five orders of magnitude compared to the undiffracted beam. The additional spike at -27ps is an artifact of the third-order correlator (sometimes called a ghost pulse) in which the post pulse at 27ps appears in the trace as a prepulse at -27ps, but two orders of magnitude weaker in intensity than the postpulse.

Finally, in figures 3.15 and 3.16, we plot the recovered temporal profile and GRENOUILLE trace for the incident probe beam and diffracted probe beam, respectively. Here we see that the grating does induce some spectral and temporal modulations, possibly from non-linear interaction of the probe beam inside of the gas cell with the air. The pulse is seen to broaden by 8 fs, but the phase remains smooth, suggesting that the pulse duration can be corrected.

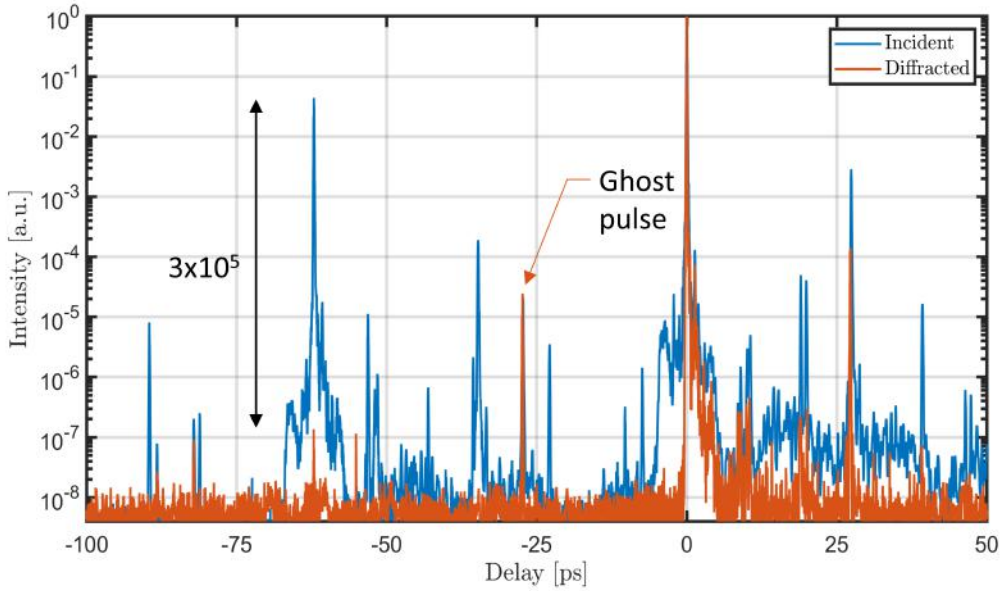


Figure 3.14: Contrast measurement of the incident (blue) and diffracted (red) laser showing that the diffracted beam improved the temporal contrast by at least a factor of 3×10^5 . To obtain this enhancement, the incident beam's temporal contrast was intentionally spoiled by introducing a prepulse at about -60ps. The spike at -27ps in the diffracted beam is an artifact of the measurement device (third-order correlator) due to the presence of a large post pulse at +27ps.

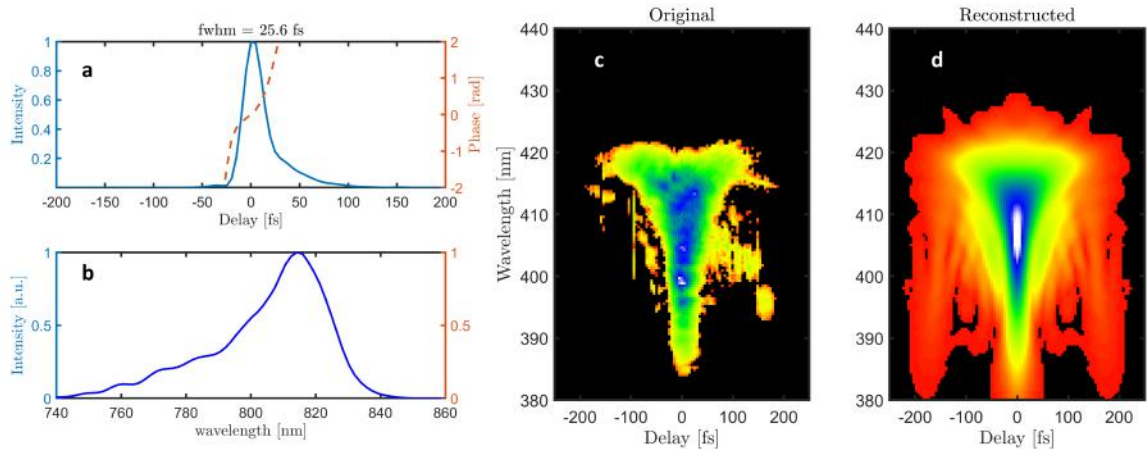


Figure 3.15: Pulse duration measurement of the incident probe beam. (a) Recovered temporal profile of the beam. (b) Recovered spectrum of the laser obtained by Fourier transforming the pulse from (a). (c) The original FROG spectrogram that is input into the FROG algorithm. (d) The recovered FROG spectrogram.

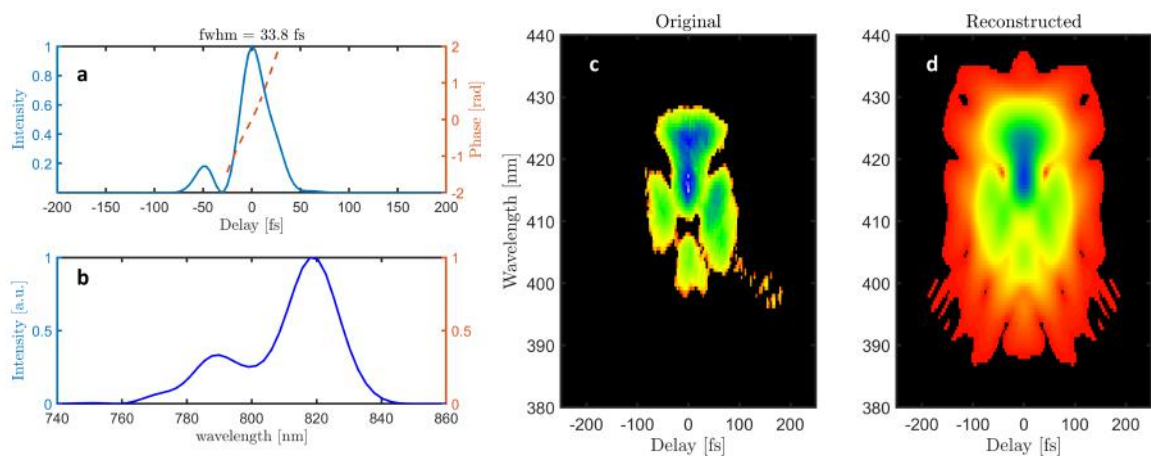


Figure 3.16: Pulse duration measurement of the diffracted probe beam. (a) Recovered temporal profile of the beam. (b) Recovered spectrum of the laser obtained by Fourier transforming the pulse from (a). (c) The original FROG spectrogram that is input into the FROG algorithm. (d) The recovered FROG spectrogram.

Chapter 4

A Cascaded Plasma Mirror Configuration for Enhanced Harmonic Generation

4.1 Introduction

In the chapter 2 we studied the sub-cycle dynamics of the electron bunches formed during the interaction of relativistic laser-plasma interactions and showed how the properties of the electron bunches, namely the bunch width and peak density, are crucial for achieving efficient conversion of energy from the driving laser to the high order harmonics. Since the dynamics of these electron bunches evolve on a sub-cycle timescale, the waveform of the laser, not just the temporal envelope, is crucial. Phase-controlled two-color lasers provide an additional degree of freedom for controlling these electron bunches compared to a single color alone, where a combination of experimental and numerical works have used two-color lasers to enhance harmonic efficiency and increase attosecond pulse isolation [60, 61, 113, 116, 136].

Waveform-controlled harmonic generation can be experimentally realized in a number of configurations. Previous experiments used second harmonic crystals to construct a two-color beam [60, 61]. However, two-color waveforms constructed with crystals are

not ideal for high-power systems since they cause pulse broadening and produce second harmonic which contains amplified spatial inhomogeneities of the laser fundamental. In addition, high peak powers will demand crystals with prohibitively large diameters. A second approach to realize waveform-controlled harmonic generation is to use a multi-pass plasma mirror configuration in which the reflected harmonics from one plasma mirror are used to drive harmonics on a second plasma mirror [114, 115]. Such a scheme can be realized by either placing two plasma mirrors within one Rayleigh length or by collecting the harmonics from the first plasma mirror and refocusing them onto a second plasma mirror. The former places strict requirements on the separation of the two targets to within one Rayleigh range [137], which is often less than $10\mu m$ for the short focal length focusing optics used in high intensity laser applications. The latter configuration has the downside of losing the high-order harmonics due to the poor reflectivity of standard mirrors for wavelengths below 200nm, but since the fraction of energy contained in these harmonics is comparatively low, the largest effects will come from just retaining the first few harmonic orders.

In this chapter, we first demonstrate that a plasma mirror can be used to synthesize a two-color, multi-terawatt laser beam. We then show the implementation of a multi-pass harmonic generation configuration in which the reflected fundamental and second harmonic from one plasma mirror are collected and refocused onto a second plasma mirror. We present spatial and spectral measurements of the reflected fundamental and the generated second through fourth harmonic orders, showing enhanced and suppressed harmonic emission for a two-color driving laser compared to a single-color laser, depending on the waveform of the two-color. As the target is scanned along the laser propagation direction, we show that the radiated harmonics can be either enhanced or suppressed due to the waveform evolution of the two-color laser as it propagates in free space.

4.2 Experimental set-up of a cascaded plasma mirror configuration

The experimental setup for studying waveform-controlled harmonic generation from plasma mirrors is shown in figure 4.1. The experiments use a 20TW Ti:Sapphire laser system which provides 25fs pulses centered at 800nm and an adjustable pulse energy between 10-400mJ. The set-up features three plasma mirrors. The first plasma mirror (PM1) is used as a contrast cleaner and operates at near-normal incidence. A full description of PM1's performance was provided in the previous chapter. The second and third plasma mirrors are both driven at relativistic intensities and used to generate harmonic orders of the driving lasers fundamental wavelength. In the next section we characterize the performance of PM2, which is used to synthesize a two-color waveform. In the section after that we study harmonic generation from PM3 when using the two-color laser from PM2.

4.3 Plasma mirror for synthesizing a terawatt two-color laser

The second plasma mirror (PM2) in the experimental set-up is different from PM1 in that the laser is obliquely incident on the plasma mirror and the focal length of the off axis parabolic mirror is only 152.4mm ($f/4$), yielding focused intensities up to 1×10^{19} . This is the first relativistic plasma mirror in the multi-pass configuration and its primary purpose is to synthesize the two-color laser. In principle, higher order harmonics are radiated from PM2, but they are lost in the beam transport. However, since the higher order harmonics have comparatively less energy than the fundamental and second harmonic, the largest effect on harmonic generation from the second relativistic plasma mirror (PM3) will come from just retaining these two colors.

For plasma mirrors to be useful as a two-color waveform synthesizer, the fraction of energy converted to second harmonic needs to be substantial enough to yield enhanced

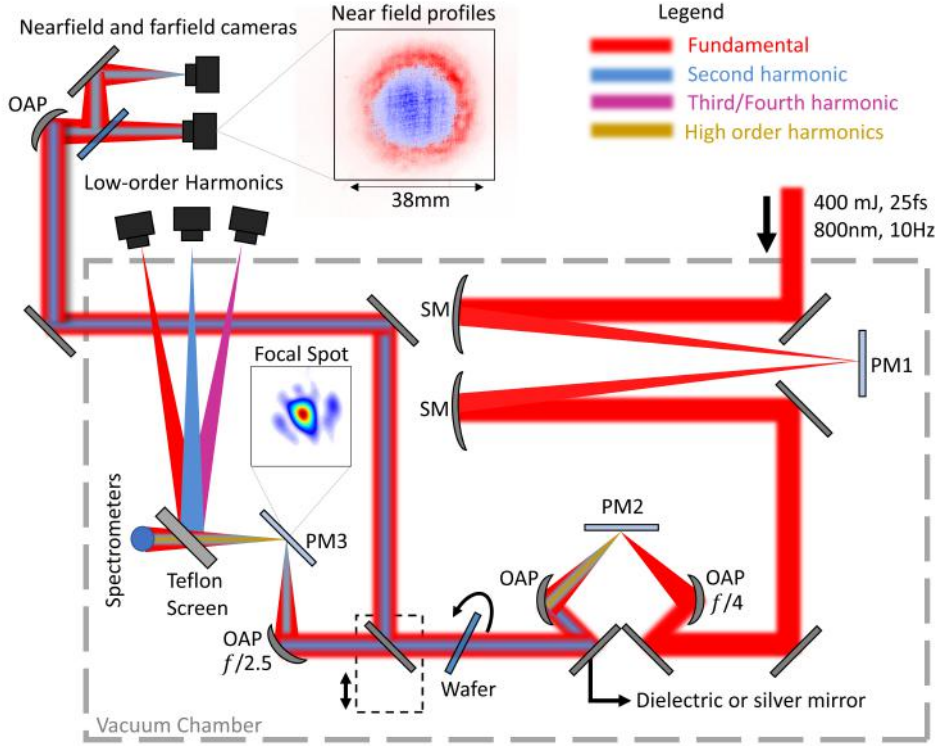


Figure 4.1: Experimental set-up of the multi-pass plasma mirror configuration. The laser beam (800nm, 10Hz, 25fs, 400mJ) enters the experimental vacuum chamber from the upper right and interacts with three plasma mirrors: one contrast-cleaning plasma mirror (PM1), a relativistically-drive plasma mirror used to synthesize a two-color waveform (PM2), and a relativistically-driven plasma mirror used for studying harmonic generation with the two-color laser (PM3). A mirror that sits on a translation stage can pick off the laser after the PM2 interaction which allows for near-field and far-field characterization of the two-color laser. A $100\mu\text{m}$ thick fused silica wafer is placed between PM2 and PM3, where the rotation of the wafer allows for controlling the relative phase between the two colors. After the interaction from PM3, visible and ultraviolet CCDs image the harmonics from a Teflon screen, and a visible spectrometer measures the spectrum. For one-color experiments on PM3, a sliver mirror was replaced with a dielectric mirror, which has poor reflectivity at 400nm. Insets: (lower panel) a focal spot image of the 800nm beam on PM3. (upper panel) The overlapping nearfield profiles of 400nm and 800nm light. Key: PM = Plasma Mirror. SM = Spherical Mirror. OAP = off axis parabola.

harmonics in subsequent plasma mirrors. Fortunately, particle-in-cell simulations have shown that even just a small amount of second harmonic energy, say 5%, can yield order of magnitude enhancement in attosecond pulse intensity [113]. In figure 4.2, we plot the second harmonic reflectivity as a function of the plasma mirror's position with respect the laser's best focus (right panel). In figure 4.2(m), the second harmonic energy increases as the plasma mirror is scanned through the laser's best focus, reaching greater than 8% energy conversion to the second harmonic at $z=0$.

Also plotted in figure 4.2 are the measured beam profiles of the incident 800nm laser as a function of z . Here we see a high quality focal spot with a $5\mu\text{m}$ FWHM at best focus ($z = 0$), but the presence of beam aberrations in the midfield ($z > 60\mu\text{m}$). Although the fraction of energy that is converted to second harmonic is enough for applications, the spatial quality of the second harmonic is crucial for experiments and the presence of these beam aberrations can affect the beam quality of the resulting two-color laser. In figure 4.3, lineouts of the fundamental (red) and second harmonic (blue) near field profiles are plotted for both in-focus (4.3(a) - $z=0\mu\text{m}$) and out of focus (4.3(b) - $z = 100\mu\text{m}$) interactions. For the in-focus interaction, the second harmonic has a Gaussian-like shape, although the fundamental beam has a flat top shape. This is one main advantage in using a plasma mirror instead of a crystal to generate the second harmonic; second harmonic generation from crystals amplifies the spatial inhomogeneities present in the fundamental, which is what we see for the out-of focus interactions [figure 4.3(b)]. In conclusion then, plasma mirrors can be used to generate a high quality two-color laser provided that the plasma mirror lies within one Rayleigh range of the driving lasers best focus.

In figure 4.4, we plot the measured far field profiles (d-f) alongside the near field spatial profiles (a-c) taken when the plasma mirror is at the laser's best focus. In addition to the high spatial quality of the near field spatial profiles, both colors can be simultaneously focused to a single spot. Although the second harmonic has half the wavelength of the fundamental, the collimated second harmonic is also smaller than the collimated fundamental so that the focal spots are roughly the same size as shown in figure 4.4(f). Taken together, the results of this section suggests the advantages to using plasma mirrors

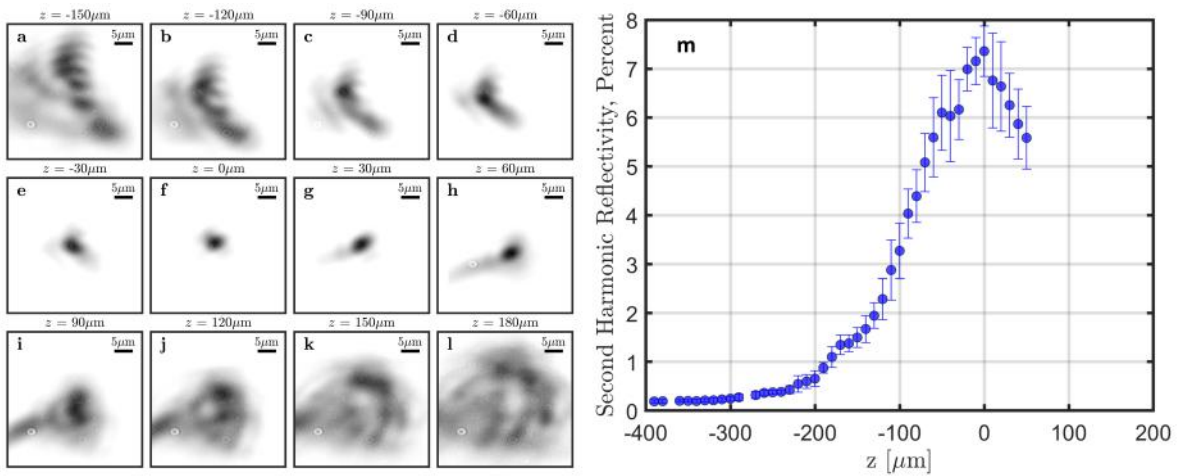


Figure 4.2: (left) Measured beam profile incident on the surface of PM2 as a function of z . (right) Second harmonic reflectivity as PM2 is scanned through the focus at a fixed incident laser energy of 60mJ.

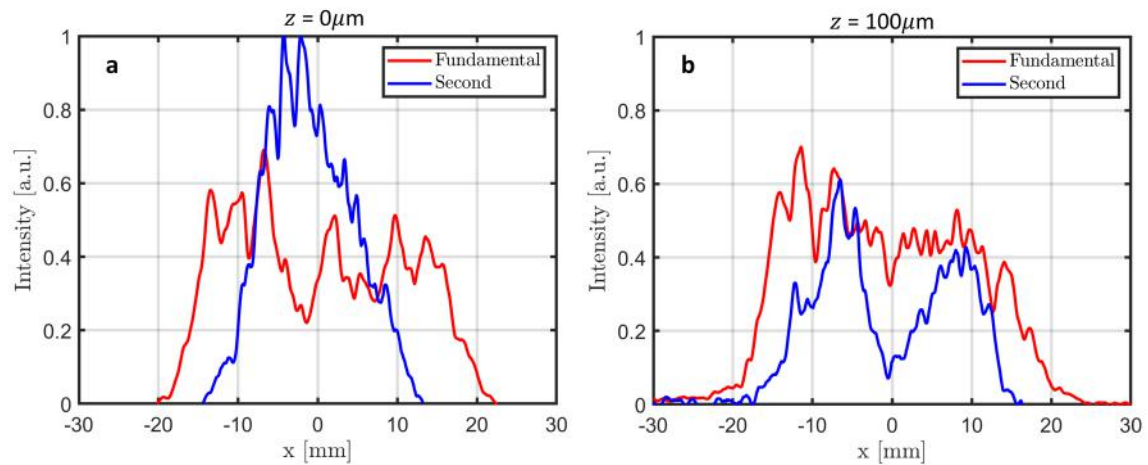


Figure 4.3: Lineouts of the spatial profile of the reflected fundamental and second harmonic from PM2 for an in-focus interaction (left - $z = 0$) and an out-of-focus interaction (right - $z = 100\mu\text{m}$).

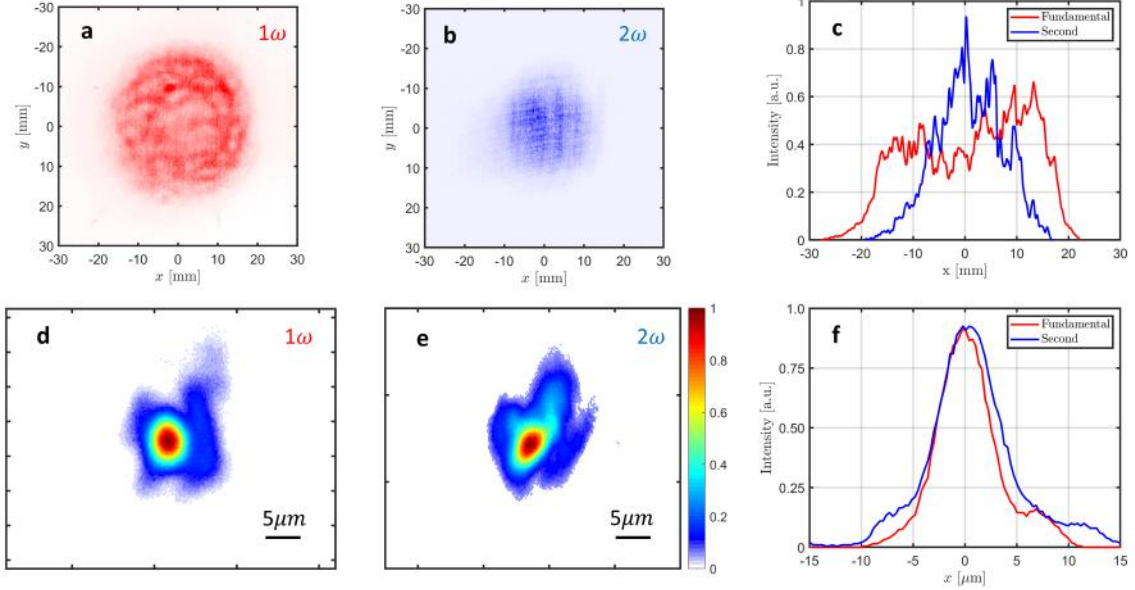


Figure 4.4: Measured near field (a,b) and far field (d,e) profiles of the reflected fundamental and second harmonic from PM2 taken when the plasma mirror was at the laser’s best focus. Subplots (c) and (f) show the vertical lineouts of the near field and farfield profiles taken at $x = 0\text{mm}$.

for synthesizing a two-color laser in-place of a conventional second harmonic crystal. The main drawbacks when using plasma mirrors is that the initial set-up is more challenging, and plasma mirrors are a disposable optic since the surface is damaged on every shot. However, we find that the performance of the plasma mirror is robust after the initial configuration. Furthermore, there has been recent research into renewable plasma targets based on liquid jets which can overcome these obstacles [138].

In figure 4.5, we plot the spatial profile of the fundamental beam entering the experimental chamber (Direct beam), after reflection from PM1, and after reflection from PM1 and PM2. The top row of subplots [4.5(a-c)] show the beam profiles under normal operating conditions, showing the improved spatial quality after reflection from both plasma mirrors as several hot-spots present in the direct beam have been smoothed out. The bottom row of profiles were taken under the same conditions except that the spherical mirror that collimates the laser after the PM1 interaction was damaged, yielding the distorted profile in figure 4.5(e). Interestingly, the final beam profile after reflection from PM2 [figure 4.5(f)] is similar to the beam after reflection from PM2 when there were no damaged mirrors on the beam path [figure 4.5(c)].

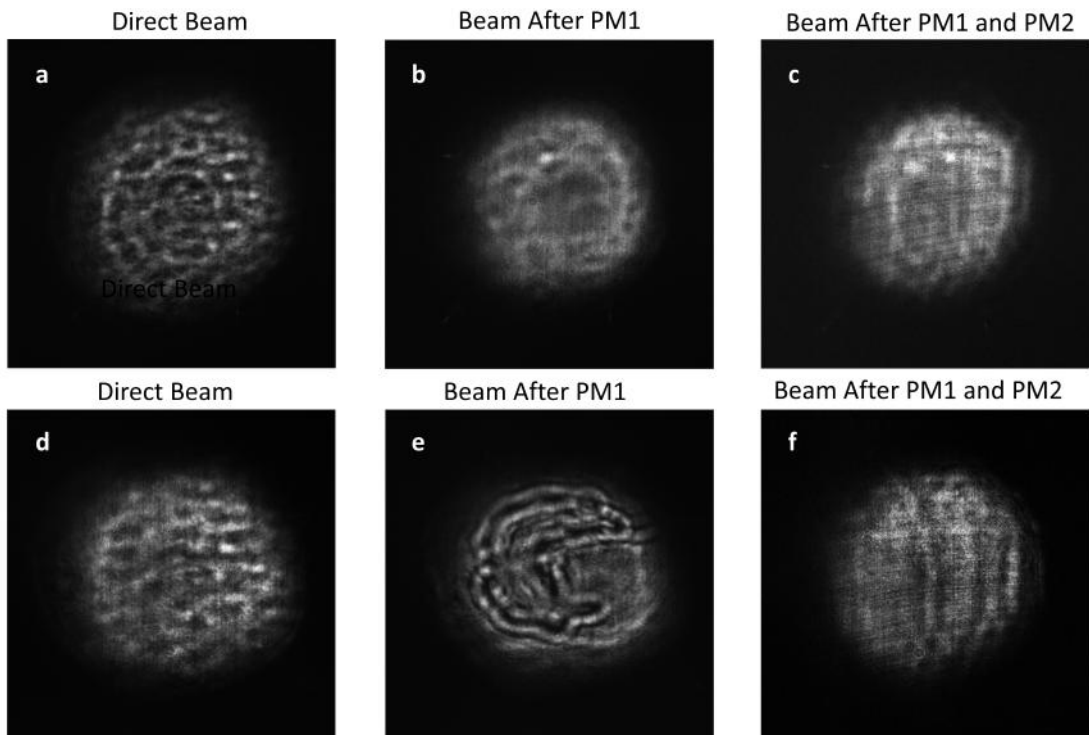


Figure 4.5: Spatial profiles of the direct beam, the beam after PM1, and the beam after PM1 and PM2, illustrating the spatial cleaning effect of plasma mirrors in the sub-relativistic and relativistic regimes. The top row of images shows the reflected profiles obtained in normal operating conditions. The bottom row of profiles were taken under the same conditions as the top row of images except that the spherical mirror that collimates the laser after the PM1 interaction was damaged, yielding the distorted profile in (e).

4.4 Waveform engineering for enhanced harmonic generation and sub-cycle control of electron density dynamics

The final plasma mirror (PM3 - see experimental set-up in figure 4.1) is another relativistic plasma mirror but with a tighter focusing geometry ($f/2.6$ for PM3 compared to $f/4$ for PM2). This plasma mirror is used for studying the effects of harmonic generation from the two-color waveform that was generated using PM2. The waveform of the two-color laser is controlled by rotating a $100\mu m$ fused-silica wafer placed in the beam's path after PM2. At an incidence angle of 25° , the wafer is 93% transmissive and introduces a relative phase difference of $\approx 135^\circ$ between the fundamental and second harmonic (See appendix D for detailed wafer calculations as a function of the wafer angle). To compare two-color interactions with one-color interactions we replace a mirror after PM2 from one that efficiently reflects the fundamental and second harmonic (a silver coated mirror) with one that only reflects the fundamental (a dielectric coated mirror).

After reflection from PM3, the fundamental and the second through fourth harmonic orders are imaged from a scattering screen using CCDs placed behind the appropriate bandpass filter. A 1cm hole on the scattering screen allows for simultaneous measurements of the visible spectra (Ocean Optics, 200nm-1100nm). The third (267nm) and fourth (200nm) harmonics lie within the ultraviolet wavelength regime and are ordinarily difficult to measure with standard CCDs and solid-state optics. In our experiment, we use a UV-enhanced CCD (pco.panda 4.2 bi UV), UV enhanced aluminum mirrors (Thorlabs), and UV-grade fused silica windows and lenses, which allows for detection of the third and fourth harmonic orders, for the first time from a Ti:Sapphire laser system operating at 800nm central wavelength. The third harmonic is a particularly convenient metric since second harmonic cannot produce third harmonic by itself, so any enhancement in third harmonic energy from a two-color interaction compared to a one-color interaction must come from the combined effect of the fundamental and second harmonic.

Fig. 4.6 shows the spatial profiles (a-d), vertical lineouts of the spatial profiles (e), and

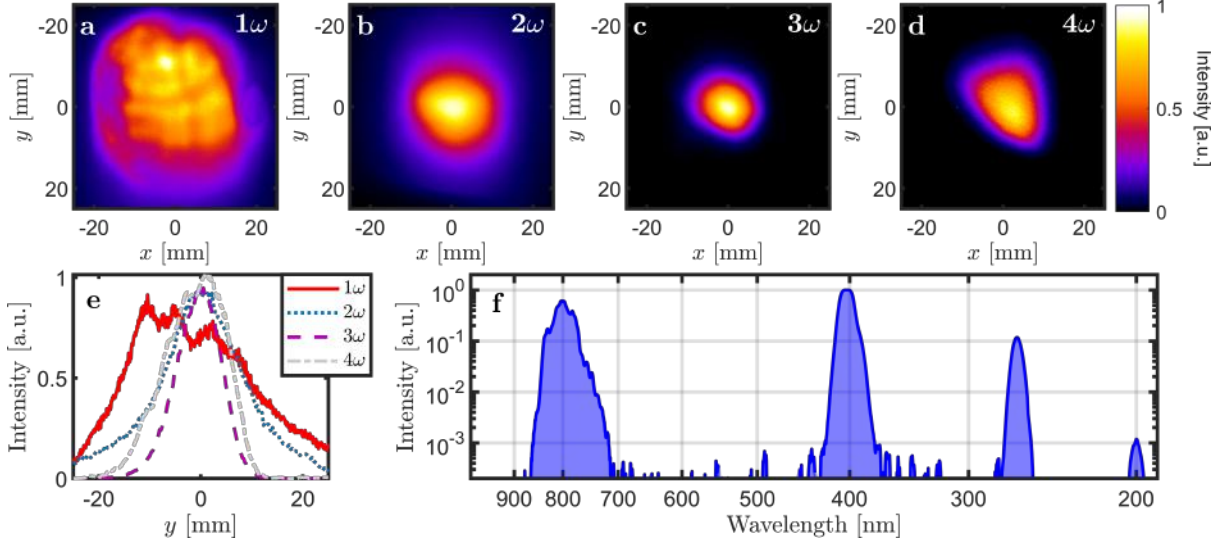


Figure 4.6: Near-field spatial profiles (a-d), vertical lineouts of the spatial profiles at $x = 0\text{mm}$ (e), and the reflected visible spectrum (f) of the reflected fundamental and second through fourth harmonic orders taken after PM3. The interaction was taken with the plasma mirror at the laser's focus using a two-color laser with an intensity of $I_L = 10^{19}\text{W/cm}^2$. Before the interaction, the two-color laser passed through the wafer at an incidence angle of 25° . All harmonic profiles are individually normalized.

the visible spectra (f) of the reflected fundamental and second through fourth harmonics taken with a two-color laser incident on PM3. All harmonics are narrowly beamed and have superior spatial quality to that of the fundamental. The second harmonic has nearly half the divergence of the reflected fundamental and the third harmonic has nearly one-third the divergence of the reflected fundamental. The fourth harmonic has a somewhat higher divergence than the third harmonic and its spatial distribution is not as round, more closely resembling the on target focal spot (see inset of Fig. 4.1). The spectra was recorded along the beam centerline where the highest fraction of the incident laser energy is converted to the harmonics.

In Fig. 4.7, we compare the reflected third and fourth harmonic energy from one-color and two-color interactions as a function of the on-target intensity. The intensity was varied by adjusting the amount of energy entering the chamber, which changes both the intensity incident on PM3 as well as the fraction of second harmonic energy contained in the two-color beam from 0-10%. Two-color interactions that enhanced harmonic efficiency (blue triangles) compared to the one-color interaction (red circles) had the wafer at a 25° angle of incidence. With no wafer in-place, the harmonic energy from a two-color

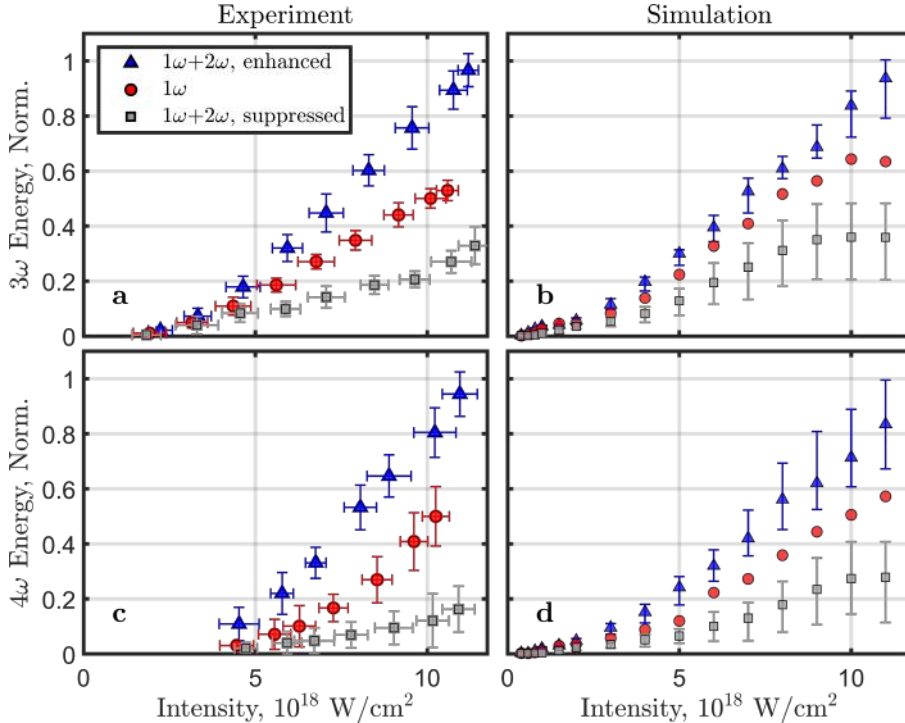


Figure 4.7: Third (a,b) and fourth (c,d) harmonic energy as a function of on-target intensity for one-color and two-color interactions. For the experiments, the intensity was varied by adjusting the energy entering the chamber, which simultaneously adjusts the energy fraction of the second harmonic between 1% and 10%. Two-color interactions that enhanced harmonic energy (blue triangles) were taken with the wafer in-place at a 25° angle of incidence. Two-color interactions that suppressed harmonic energy (grey squares) were taken without the wafer. The one-dimensional particle-in-cell simulations use a 25fs full-width-half-maximum envelope for both colors, and assume an exponential pre-plasma gradient scale length of $L = 0.05\lambda_L$. For enhanced two-color interactions, the relative phase ($\Delta\phi_{12}$) between the two colors is chosen to maximize the harmonic yield and a 10fs delay between the fundamental and second harmonic envelopes to model the effects of the wafer. For the suppressed two-color interactions, the relative phase between the two colors is chosen to be 135° less than that of the two-color enhanced simulations and the envelopes are assumed to be overlapped. For all simulations, the shaded markers are for simulations where 5% of the total energy was in the second harmonics and the errorbars show the spread in harmonic energy as this percentage is varied from 1%-10%.

interaction was suppressed (grey squares) compared to the one-color interaction. At an intensity of $1 \times 10^{19} \text{ W/cm}^2$, the third and fourth harmonics experience a maximum energy enhancement of 1.6. The negligible enhancement factors at intensities less than $5 \times 10^{18} \text{ W/cm}^2$ is due the lower on target intensity and the lower percentage of second harmonic energy. The change from enhanced third and fourth harmonic energy with the wafer to suppressed third and fourth harmonic energy without the wafer suggests that the waveform of the two-color laser plays an important role in harmonic generation, as predicted theoretically [113, 115, 136] and confirmed experimentally [60, 61].

The experimental results are plotted next to predictions from one-dimensional particle-in-cell (PIC) simulations [Fig. 4.7(b, d)]. The simulations used a 25fs Gaussian temporal envelope at a 45° angle of incidence onto a semi-infinite, fully ionized plasma containing a preplasma modeled as an exponential with a gradient scale length of $L = 0.05\lambda_L$ up until a peak density of $n_e = 7 \times 10^{23} \text{ cm}^{-3}$. For the two-color interactions, the shaded markers assume that 5% of the fundamental has been converted to second harmonic and the errorbars depict the variation of harmonic energy as this fraction changes from 1% to 10%. For the two-color enhanced simulations (blue triangles), the second harmonic temporal envelope was delayed by 10fs to model the effects of the wafer and the phase of the second harmonic was chosen to maximum the reflected third harmonic energy. In contrast, for the two-color suppressed simulations (grey dots), the fundamental and second harmonic had no temporal mismatch and the phase of the second harmonic was chosen to be 135° less than that of the enhanced simulations to account for the fact that there was no wafer.

In figure 4.8, we plot the fundamental, second, and third harmonic energy as a function of on target intensity for one-color (red xs) and two-color (blue dots) interactions. In the top row of subplots [figure 4.8(a-c)], the wafer was in-place at a 25° incidence angle which yields enhanced second and third harmonic energy for a two-color interaction compared to a one-color interaction. Interestingly, the reflected fundamental energy is identical in the two cases. In the bottom row of subplots [figure 4.8(d-f)], the wafer was removed, yielding suppressed second and third harmonic energy for a two-color interaction compared to a one-color interaction. Again we see here that the reflected fundamental energy is the

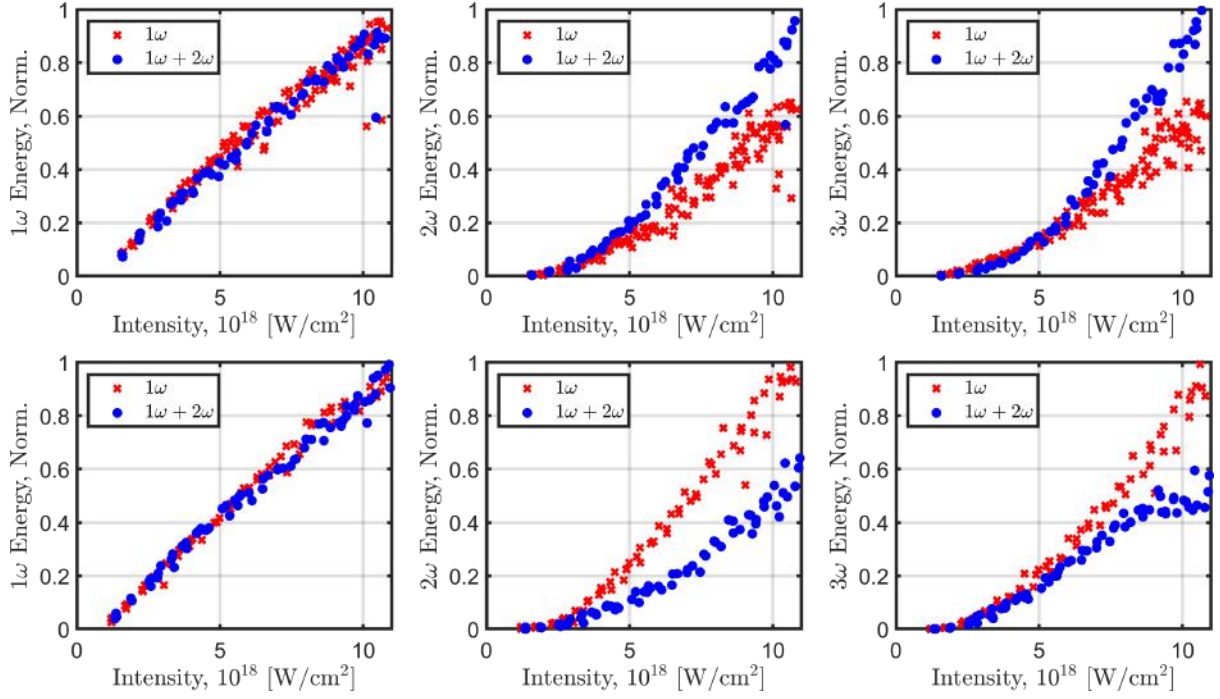


Figure 4.8: Reflected fundamental, second harmonic, and third harmonic energy for both one-color and two-color interactions as a function of on-target intensity. The top row of images were taken with the wafer in-place at a 25° angle of incidence, yielding enhanced second and third harmonic generation. The bottom row of images were taken without the wafer, yielding suppressed second and third harmonic generation.

same for the two cases.

In figures 4.8 and 4.7, the on target intensity was changed by varying the amount of energy entering the experimental chamber. In figure 4.9(a), we vary the on-target intensity by changing the incident pulse temporal width. To do this, the pulse was chirped before entering the experimental chamber using an acousto-optic modulator (AOM). This will affect the on-target intensity because the pulse duration is longer and because the reflectivity from PM1 and PM12 will decrease as the intensity decreases. The fraction of second harmonic energy after PM2 also decreases as the laser pulse duration is increased. For this set of measurements, the wafer was in-place at an angle 25° , yielding enhanced third harmonic generation. As we see in figure 4.9(a), as the group delay dispersion applied to the laser increases, the third harmonic energy decreases for both one-color and two-color interactions. For $\text{GDD} \gtrsim 1000 fs^2$, the difference between one-color and two-color interactions is negligible. In figure reffig:DazzlerScans (b,c), the pulse profile and spectra measured from a home-built Grenouille apparatus is shown [129]. At a GDD

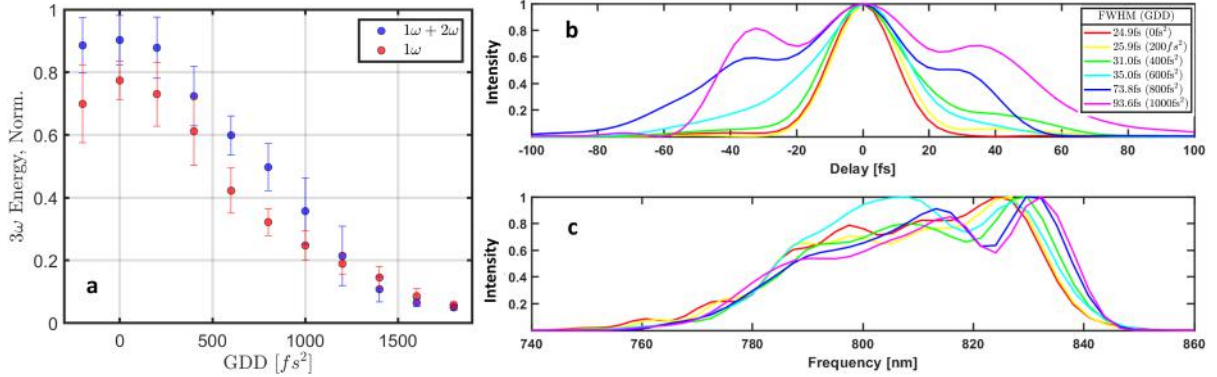


Figure 4.9: (a) Third harmonic energy for one-color and two-color interactions plotted as a function of GDD, which was controlled using an acousto-optic modulator. (b) The recovered temporal pulse profiles as measured by Grenouille for different values of GDD. The FWHM for each GDD setting is indicated in the legend. (c) The recovered spectra from Grenouille. The energy entering the chamber was kept fixed at 275mJ.

of $1000 fs^2$ the pulse duration was greater than 90fs.

In figure 4.10 and 4.11, we plot the fields, particle trajectories, and electron bunch evolution, comparing one-color interactions with two-color enhanced and two-color suppressed interactions for simulation parameters which are slightly out of reach for our laser system, but can easily be obtained on any of the Petawatt class laser systems. For these interactions with higher a_0 , the enhancement factors for two-color lasers can be much greater than the 1.6x enhancement factor achieved in experiments (figure 4.10(c)).

The simulations also reveal valuable information about the relativistic plasma dynamics which ultimately cause the enhanced or suppressed harmonic radiation. In figure 4.11(b), the electron bunch evolution from the time of maximum displacement from the initial vacuum-plasma interface through the time of attosecond pulse emission is shown for a one-color interaction. As shown in, for $a_0/N \lesssim 0.1$, the electron bunch in this regime slowly drops in peak density before emitting the attosecond pulse. In contrast, for a two-color enhanced simulation [figure 4.11(c)], the electron bunch maintains its peak density through the time of attosecond pulse emission as is the case for single color interactions with higher ratios of $a_0/N \gtrsim 0.1$. For two-color suppressed simulations [figure 4.11(a)], the electron bunch sharply drops in peak value after the time of maximum displacement, so that it is close to the original value at the time of emission. The experimental results,

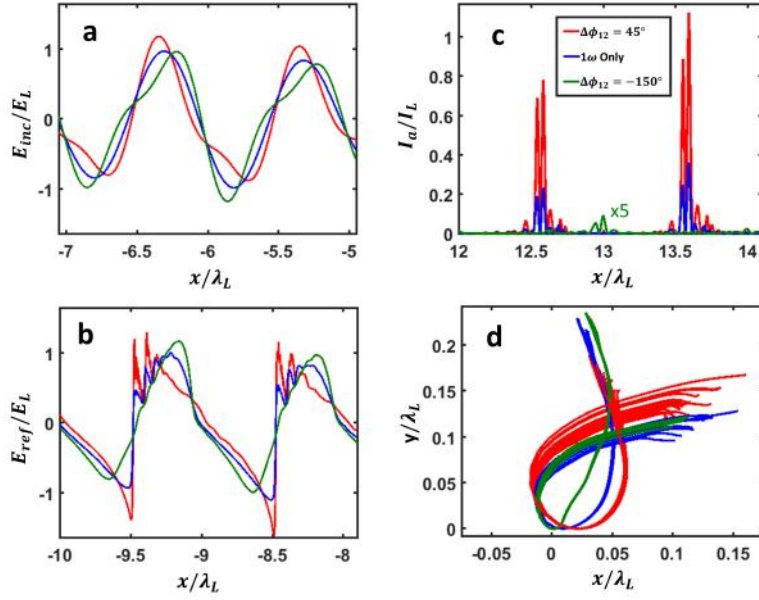


Figure 4.10: Reflected fields and particle trajectories extracted from one-dimensional particle-in-cell simulations of one and two-color interactions. (a) Incident waveform for a one-color laser (blue), a two-color laser that enhances harmonic generation (red), and a two-color waveform that suppresses harmonic generation (green). (b) and (c) show the reflected electric field waveform and filtered attosecond pulses, respectively, for the three cases shown in (a). The attosecond pulses were constructed using frequency in the range $5\omega/\omega_L < 20$. (d) Synchrotron trajectories of the emitting electrons. Relevant simulation parameters: $a_0 = 15$, $\theta = 30^\circ$, $N = 100$, $\tau = 8\text{fs}$, $C = 0.95$, $\Delta x/\lambda_L = 4000$, and particles/cell = 100. For two-color simulations, 10% of the incident laser's total energy was contained in the second harmonic.

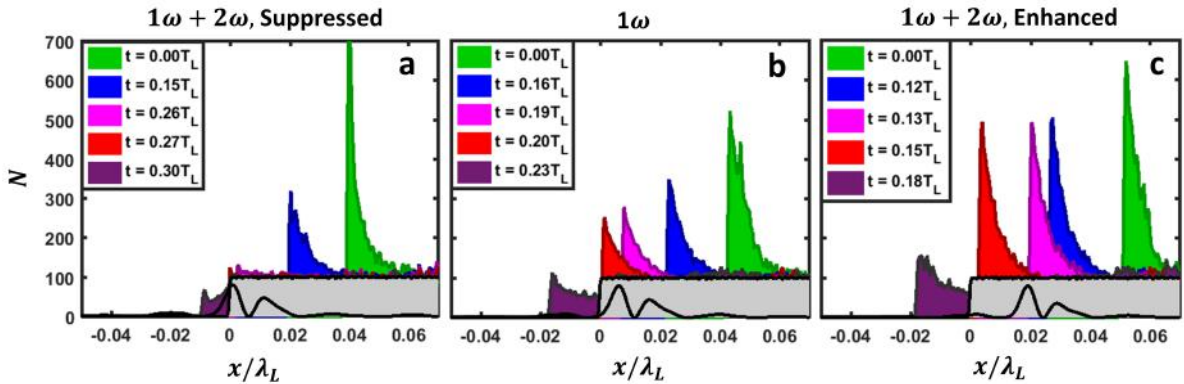


Figure 4.11: Evolution of the electron bunches from a time when the electron bunch is at its maximum displacement from the initial vacuum-plasma interface through the time of attosecond pulse emission. In each case, the electron bunch evolves from right to left and the grey shaded region shows the electron number density distribution before the arrival of the laser. The simulation parameters are the same as those used in figure 4.10.

coupled with the PIC simulations, suggest that we can control the dynamics of these electron bunches on an attosecond timescale.

To change the two-color waveform at a fixed target position, we used a dispersive element before the focus to adjust the relative phases between the fundamental and second harmonic. The waveform of the laser is also expected to evolve as it propagates in free space due to the well known Gouy phase shift [137]. To demonstrate this effect we compare the third harmonic energy for a one-color and two-color interaction as a function of the target position with respect to best focus (Fig. 4.12). In Fig. 4.12(a), the wafer was removed and we see that the third harmonic energy is enhanced for two-color interactions for $z \lesssim -0.1$ but suppressed for $z \gtrsim 0.1$. In Fig. 4.12(b), the wafer was set to a 25° angle of incidence, where we find that for $|z| \lesssim 0.1$ the third harmonic energy is enhanced for two-color interactions, while there is negligible difference between the two-color and one-color interactions everywhere else. These results suggest that the two-color waveform is evolving as it propagates through the focus. Note that due to the tight focusing geometry ($f/2$) and the aberrations inherent in the laser beam and introduced in our experiment, the evolution of the two-color waveform does not exactly evolve according to the paraxial Gaussian beam, which partially explains why the change from enhancement to suppression occurs over distances longer than the theoretical Rayleigh range of $7\mu\text{m}$.

In Fig. 4.13, the variation in peak intensity [Fig. 4.13(a)] and phase [Fig. 4.13(b)] for the fundamental and second harmonic is plotted for the case of a Gaussian beam propagating according to the paraxial equation. The calculation assumes that 10% of the energy was converted into the second harmonic and that the unfocused second harmonic beam waist is 55% that of the unfocused fundamental beam waist. Here we see that as the beam propagates away from best focus ($z = 0$), the overall peak intensity decreases but the ratio of second harmonic intensity to total intensity increases since the beam waist of both the fundamental and second harmonic grows as z increases, but the divergence of the second harmonic is less than that of the fundamental. In conjunction with a change in intensity, the relative phase ($\Delta\phi_{12} = 2\phi_1 - \phi_2$) changes by 180° . In Fig. 4.13(c), the third harmonic energy is plotted as a function of $\Delta\phi_{12}$ for one and two-color interactions.

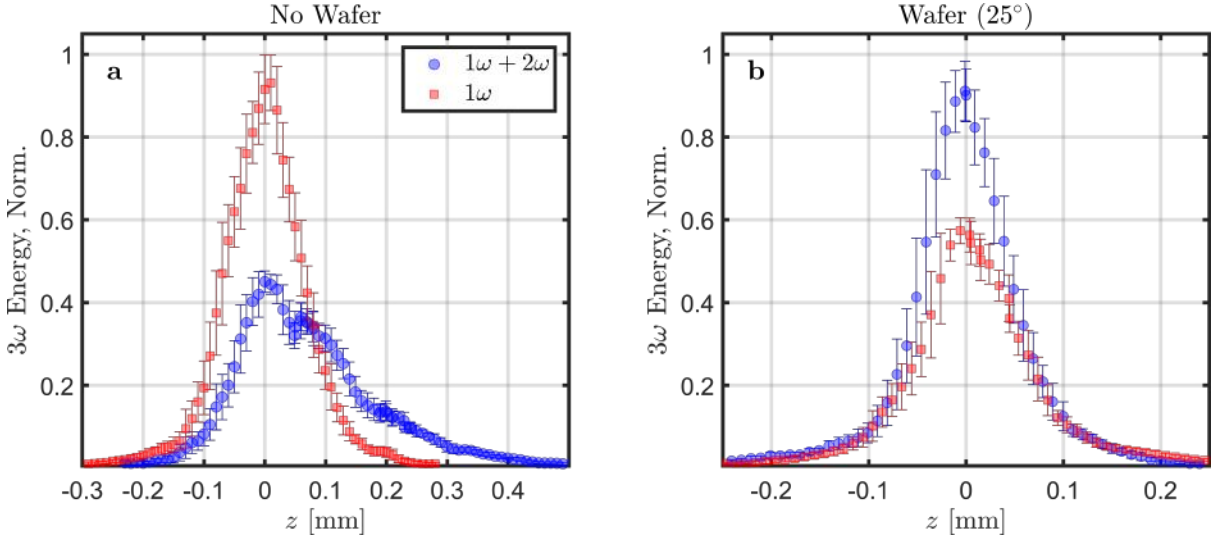


Figure 4.12: (a) Third harmonic energy as a function of PM3's target position, z , with respect to the incident laser's best focus ($z = 0$). The measurements were made with no wafer in place, yielding suppressed third harmonic energy for a two-color interaction compared to the one-color interaction at $z = 0$. (b) Same as (a) except the wafer is set to 25° , yielding enhanced third harmonic energy at $z = 0$. All measurements had an incident on target energy of $\approx 60\text{mJ}$ ($\approx 1 \times 10^{19}\text{W/cm}^2$ at $z = 0$).

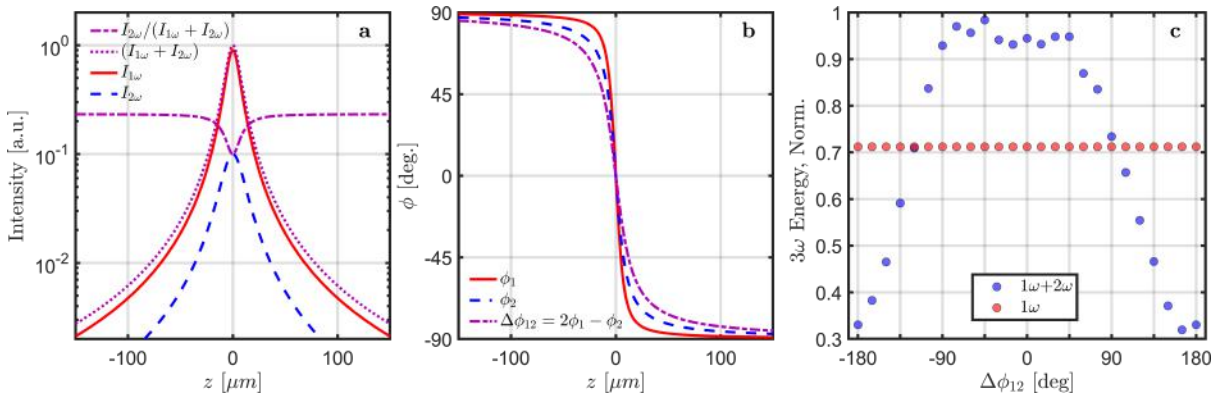


Figure 4.13: Propagation effects on the intensity (a) and phase (b) for a Gaussian laser beam. The calculation assumes that 10% of the energy was converted into the second harmonic and that the unfocused second harmonic beam waist is 55% that of the unfocused fundamental beam waist. The focal length was set to 100mm giving a Rayleigh length of $Z_R \approx 7\mu\text{m}$. (c) One-dimensional particle-in-cell simulations showing the effect of the relative phase difference of the two colors, $\Delta\phi_{12}$, on the third-harmonic energy. The simulation parameters are the same as those used in Fig. 4.7.

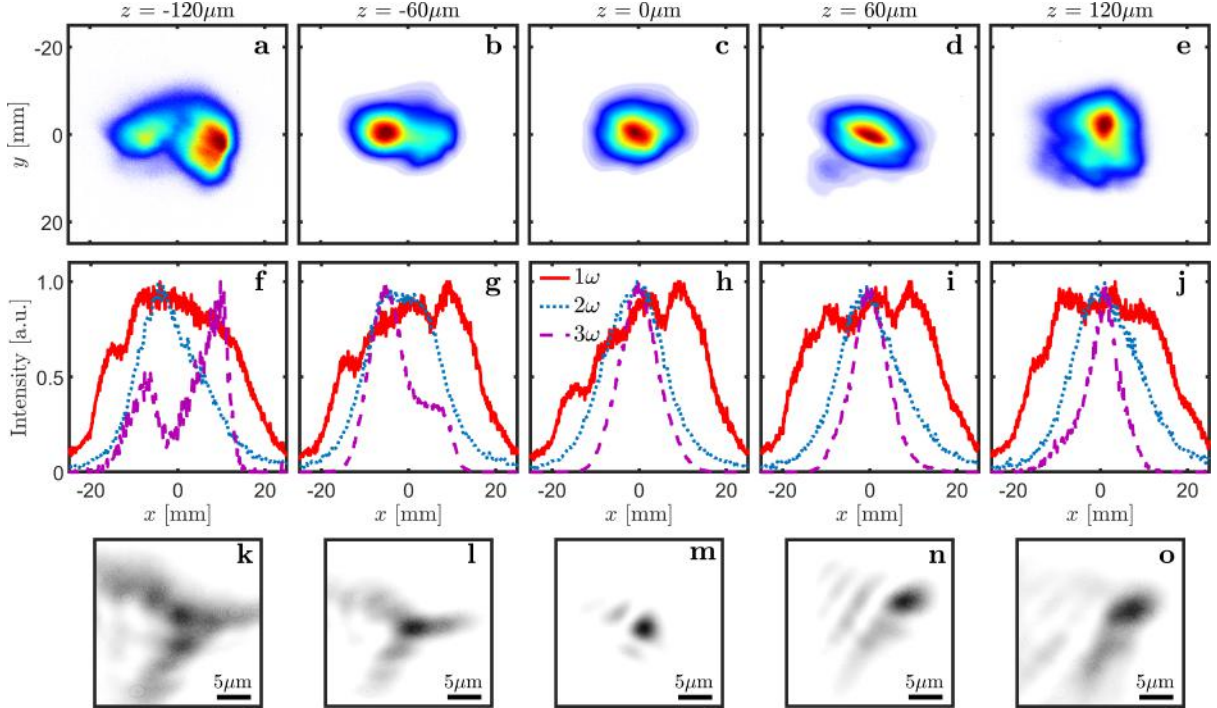


Figure 4.14: (a-e) Spatial profiles of the third harmonic for both in-focus and out-of-focus interactions. (f-j) Horizontal lineouts of the fundamental, second harmonic, and third harmonic spatial profiles at $y = 0\text{mm}$. (k-o) Measured on-target focal spots of the 800nm beam measured after interactions with PM1 and PM2.

Note that changing variations in intensity and ratio of second harmonic intensity to total intensity do not change whether the two-color beam enhances or suppresses harmonic generation as already apparent in Fig 4.7.

Although the waveform of the two-color laser can be controlled by adjusting the target's position with respect to the laser's focus position, the spatial quality of harmonics from out-of-focus interactions is expected to degrade due to the poor spatial quality of the mid-field beam [128]. In Fig. 4.14, we plot the third harmonic spatial profile [Fig. 4.14(a-e)], horizontal lineouts of the fundamental, second and third harmonic [Fig. 4.14(f-j)], and the measured on-target focal spot after PM1 and PM2 [Fig. 4.14(k-o)] for both in-focus and out-of-focus interactions. The spatial quality of the third harmonic degrades as $|z|$ increases from 0. The asymmetry in the spatial profile of third harmonic is also present from the measured on target focal spots measured after both PM1 and PM2, so that the third harmonic can be a valuable diagnostic for both the waveform of the two-color interaction and the quality of the focal spot, which was suggested previously

[139]. Interestingly, the second harmonic shows improved spatial quality well outside the Rayleigh range compared to the second harmonic generated outside the focus (see Fig. 4 of reference [128]), suggesting that using PM2 for constructing the two-color waveform improves the quality of harmonics from subsequent plasma mirrors.

In summary, we have demonstrated enhanced harmonic generation from relativistically driven plasma mirrors using a two-color waveform compared to a single-color waveform, for the first time using a multi-pass plasma mirror configuration. We demonstrated control of the two-color waveform incident on the target's surface using both a dispersive element placed in the unfocused beam path and by adjusting the target's position with respect to the focal spot. The spatial quality of harmonics radiated from the final plasma mirror is improved compared to harmonics emitted from earlier plasma mirrors, especially for interactions taken away from the laser's focus. These results provide a valuable research tool for investigating relativistically-driven, laser-produced plasmas.

Chapter 5

Harmonic Generation with Structured Lasers

5.1 Introduction

Harmonic generation from plasma mirrors has an optimal efficiency when using oblique, p-polarized interactions incident on a steep, semi-infinite plasma surface. However, optimal conversion efficiency is not the only consideration when trying to create a short wavelength light source via harmonic generation; the properties of the light source (e.g. the polarization state and spatial structure) are also important considerations depending on the intended application. In this chapter, we use particle-in-cell simulations to study relativistic harmonic generation from plasma mirrors driven by structured laser beams, including elliptically polarized lasers incident on ultrathin foils and semi-infinite targets and chirped laser pulses incident on semi-infinite targets. In each case, we show the effects of the initial laser and plasma geometry on the reflected radiation and then discuss what this radiation tells us about the relativistic plasma dynamics leading up to the emission of the radiation. We show how introducing these additional degrees of freedom to the incident laser allows for investigating the complex plasma dynamics of these unique laser-produced plasmas.

5.2 Ultrathin foil targets

5.2.1 P-polarized interactions and the importance of the electron bunch width on harmonic efficiency

Over the last 15 years, a large amount of research in high-energy laser-plasma interaction has studied the potential of ultrathin (nanometer-scale) foils to generate energetic bunches of electrons [140–143], and ions [144–153], as well as high harmonics and isolated x-ray pulses [49, 58, 59, 110, 112, 154–161]. However, there is limited research on analyzing the effect of the finite width of nanometer-scale electron bunches on the short-wavelength radiation that is emitted and the energy spectra of accelerated particles. In this section, we first present the case of p-polarized light incident on ultrathin foils and show that the emitting electron bunch width is significantly larger than that in semi-infinite plasma surfaces and governs the spectral shape of the emission [112]. We then study the case of circularly polarized light normally incident on an ultrathin foil and show, using three-dimensional particle-in-cell simulations, that this interaction produces vortex harmonics in both the reflected and transmitted geometries. Parameter scans of the target thickness, pulse duration, laser angle of incidence, and polarization state are performed which identifies efficient operating regimes and a sensitivity analysis to the generation of pure vortex modes.

In the ultrathin foil regime ($d \ll \lambda_L$ or $D = d/\lambda_L \ll 1$, where d is the target thickness), the relativistic harmonic efficiency becomes dependent on the charge contained within the target divided by the normalized laser amplitude (ND/a_0), rather than on N , D , or a_0 separately [154–156, 162]. In figure 5.1, the spectral efficiency in the reflected [figure 5.1(a)] and transmitted [figure 5.1(b)] directions contained in the frequency range $4 < \omega/\omega_L < 100$ is plotted as a function of ND/a_0 for several values of a_0 . Points to the right of this plot ($ND/a_0 > 0.5$) are considered to be in the semi-infinite regime as increasing the target thickness has no effect on the reflected efficiency. Decreasing the the foil thickness, D , for a fixed ratio of N/a_0 can result in at least two orders of magnitude increase in efficiency for moderately relativistic laser intensities (e.g. $a_0 \approx 10$) compared

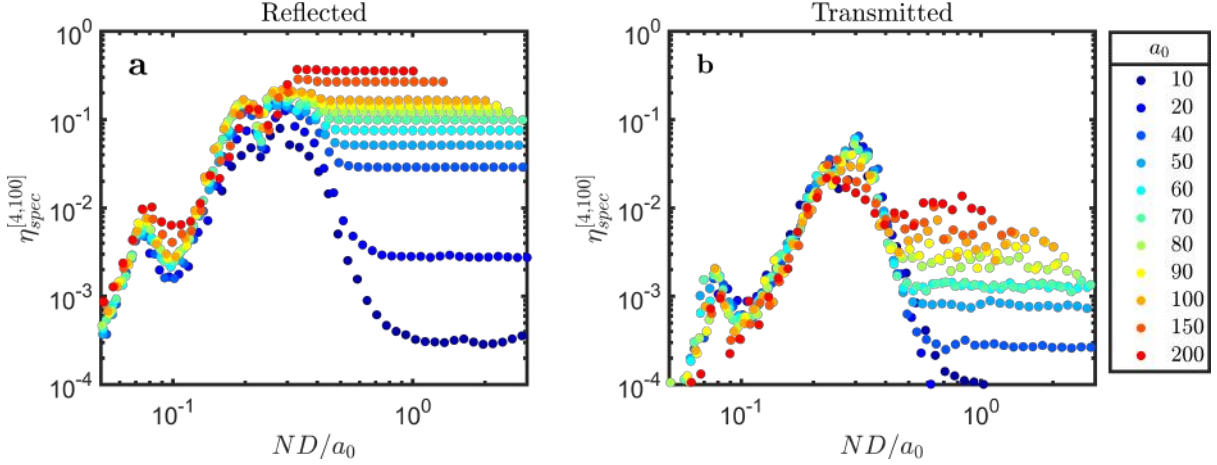


Figure 5.1: Spectral efficiency in the range $4 < \omega/\omega_L < 100$ of the (a) reflected and (b) transmitted radiation for various plasma thicknesses, D , and laser amplitudes, a_0 . Relevant simulation parameters: $\tau/T_L = 1$, $\phi_{CEP} = 90^\circ$, $\theta = 30^\circ$, $N = 400$, $\lambda_L/\Delta x = 5000$, and particles/cell = 200, $L = 0$.

to that obtained from the semi-infinite interaction. For $ND/a_0 < 0.2$ we see a collapse of the conversion efficiency to a single line for all a_0 , indicating that the efficiency of the process depends only on the parameter ND/a_0 .

Since relatively few particles are needed to model ultrathin foils, it is computationally feasible to track the dynamics of all particles in the simulation domain. In figure 5.2(a), we plot the distribution of the relativistic Lorentz factors of emitting electrons as a function of the advanced time coordinate. In the ultrathin foil regime, we find a large spread in the peaks of the Lorentz factors, extending to several tenths of a laser period. The distribution itself, has a steep leading edge where the peak Lorentz factors abruptly jump from zero and then slowly fall off. In figure 5.2(b), the particle trajectories in the x - y plane are plotted. Here we see that all the electrons in the bunch individually follow synchrotron trajectories, where emission occurs at $y/\lambda_L \approx 0.3$ but is spread out along the x-axis.

With detailed knowledge of the particle trajectories, it is possible to reconstruct the emitted fields of individual electrons in the reflected direction [163]:

$$E_y = 2\pi\sigma \frac{v_y}{c - v_z \operatorname{sgn}(x - x_u)} \quad (5.1)$$

where σ is the charge density, and x_u is the location of the observer. For the reflected

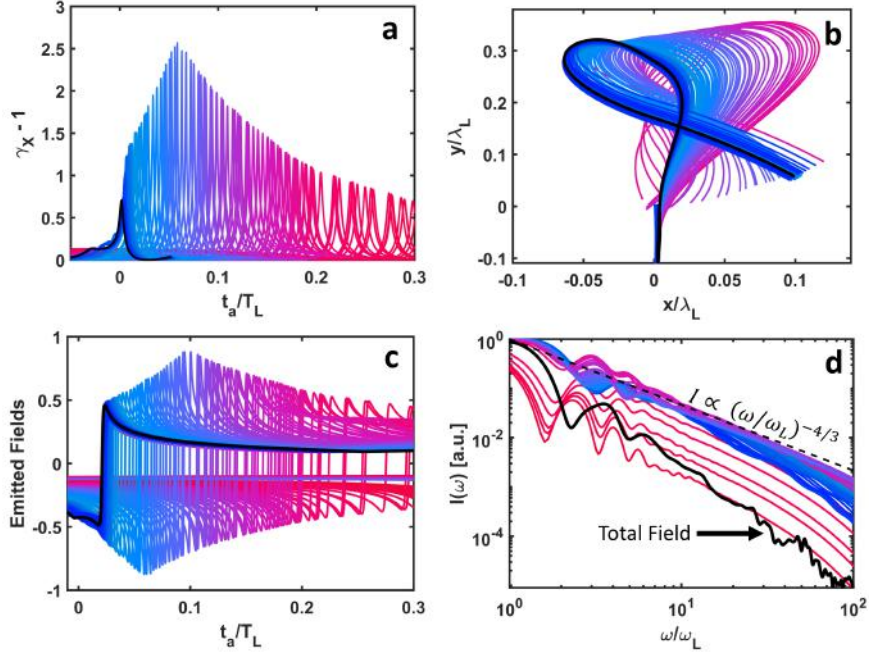


Figure 5.2: The dynamics of the emitting electrons within the electron bunch and the fields they emit when an intense laser interacts with an ultrathin foil. (a) Distribution of the electron's relativistic Lorentz factors as a function of the advanced time coordinate. (b) The synchrotron trajectories of emitting electrons in the $x - y$ plane. (c, d) Individual fields produced by these electrons in the (c) time and (d) frequency domain. In (a, b, c) the black line highlights a single electron. In (d) the solid black line represents the total reflected field after combining the emission from all particles. The dashed line represents a power-law scaling ($I(\omega) \propto \omega/\omega_L)^{-4/3}$. Relevant simulation parameters: $\tau/T_L = 1$, $\phi_{CEP} = 90^\circ$, $\theta = 0^\circ$, $N = 400$, $\lambda_L/\Delta x = 0$, and particles/cell = 0, $L = 0$, $D = 0.004$.

direction, we choose $x_u < x$ and for the transmitted direction, we choose $x_u > x$. The calculated electric fields and corresponding spectra for each particle shown in figure 5.2(a), are plotted in figure 5.2(c) and 5.2(d), respectively. Although most individual electrons have a spectral scaling in agreement with the Coherent Synchrotron emission (CSE) model, which predicts a power-law spectral scaling with an exponent of -4/3, the total reflected field (black line in figure 5.2(d)) has a much steeper slope.

Recall that the reflected spectra, within the framework of the CSE model, can be expressed by the following relation [108]:

$$I(\omega) \propto |\tilde{f}(\omega)|^2 \omega^{-4/3} \left\{ \text{Ai}' \left[(\omega/\omega_\gamma)^{2/3} \right] \right\}^2 \quad (5.2)$$

Where $\omega_\gamma = \sqrt{8\alpha}\gamma^3$, α is a constant calculated from the electron trajectories, $\gamma =$

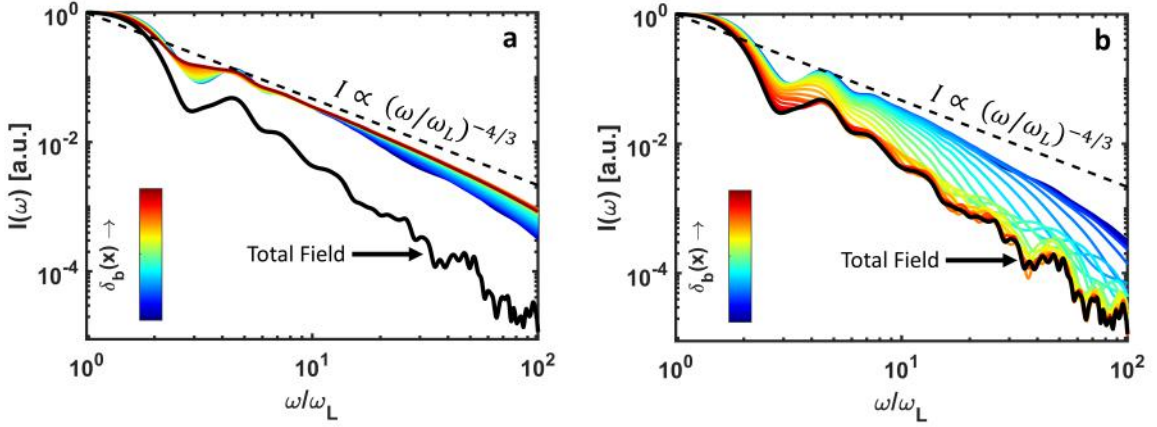


Figure 5.3: Reconstruction of the total reflected spectrum by progressively incorporating more electrons from the leading edge of the electron bunch. In (a) the spectrum is constructed by neglecting phase contributions and represents the if all electrons emitted coherently. In (b) the contribution of the phase is taken into account and results in a much steeper power-law scaling. Simulations parameters are the same as those presented in figure 5.2.

$1/\sqrt{1 - v^2/c^2}$ is the Lorentz factor of emitting electrons, Ai' is the derivative of the Airy function of the first kind, and $\tilde{f}(\omega)$ is the Fourier transform of the electron bunch shape function.

If we take $\tilde{f}(\omega)$ to be a delta function, then the reflected spectra will follow a $-4/3$ scaling which is in excellent agreement between the model and single electron spectra. In figure 5.3(a), we progressively sum the emitted intensity (i.e. ignoring contributions from the phase) from electrons within the electron bunch, showing that the total spectra follows a $-4/3$ power-law. However, when accounting for phase in this sum [figure 5.3(b)], the spectra converges to a steeper power-law as a consequence of destructive interference between emitting electrons within the electron bunch width. Looking back at figure 5.2(a), we see that the electron bunch has a finite extent that is better modeled as a step function rather than a delta function, since the peak Lorentz factors abruptly jump close to the maximum value at the leading edge of the distribution. Taking $\tilde{f}(\omega)$ to be a step function adds a factor of ω^{-2} to equation 5.2, yielding a power-law scaling of $\omega^{-2}\omega^{-4/3} = \omega^{-10/3}$. For ultrathin foils, the collapse of spectral efficiency [Figure 5.1(a,b)] is accompanied with a generalized spectral power-law scaling of $p = -10/3$.

It is instructive at this point to compare the distribution of Lorentz factors for an

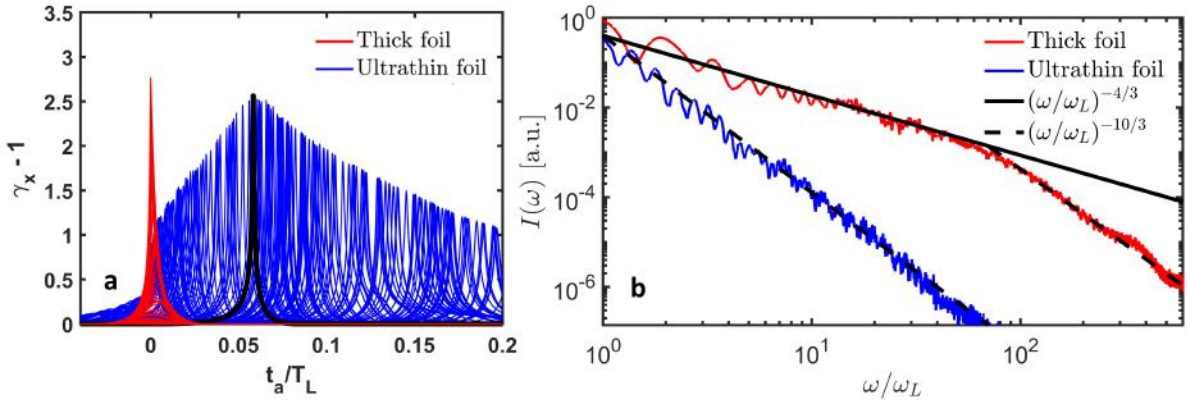


Figure 5.4: (a) The emitting electron bunch for both an ultrathin foil (blue) and a semi-infinite target (red). The black line in (a) isolates a single electron Lorentz factor to highlight its shape, which closely resembles a delta function. (b) The reflected spectra for the ultrathin foil simulation (blue) and semi-infinite target (red). The solid black line follows a -4/3 power law scaling and the dashed black line follows a -10/3 power law scaling.

ultrathin foil with that of a semi-infinite target [figure 5.4(a)]. Here we see that the electron bunch for the case of a thin foil (blue lines) extends to several tenths of a laser period while the electron bunch for the case of a semi-infinite target (red lines) is much less than one-tenth of a laser period, more closely resembling a delta function at this scale. This results in a -4/3 power-law scaling for the thick foil for harmonic orders less than ≈ 100 . The power law scaling then transitions to a -10/3 power-law when the emitted wavelength reaches a size comparable to that of the emitted electron bunch width. Therefore, although thin foils are a promising route for enhancing spectral efficiency for low values of a_0/N where thick foils yield spectra that follow a power-law which is steeper than -10/3, the most efficient interactions remain for p-polarized, oblique incidence interactions with thick foils.

5.2.2 Circularly polarized interactions and the emission of vortex harmonic orders

Light can be tailored in space, time, or through its polarization state to produce uniquely structured light beams. These structured light beams can carry angular momentum in the form of spin angular momentum (SAM) as a result of the polarization state of

the light [164], as well as orbital angular momentum (OAM) as a result of the twisted phase fronts of the light [165]. Spatially structured light that carries OAM, such as the Laguerre-Gauss modes which are solutions to the paraxial wave equation in cylindrical coordinates, are known as vortex beams. The twisted phase fronts of vortex beams arise from an azimuthally-dependent phase term ($\exp(-il\phi)$), where l is the azimuthal index and is usually referred to as the topological charge. In addition to the twisted phase fronts, vortex beams contain a null on-axis intensity which leads to their characteristic donut-shaped intensity profile in the transverse plane. These unique properties of vortex beams have been used in several breakthrough applications such as optical communications [166, 167], optical manipulations [168], and super-resolution microscopy [169].

However, most of these applications have taken place in the visible and near-infrared wavelength regimes and at relatively low powers. To achieve high-power extreme ultraviolet (xuv) vortex beams, several works have proposed converting infrared lasers with relativistic intensities to an xuv source through high harmonic generation from laser-solid interactions. Experimentally, xuv vortex beams were generated by using a linearly polarized infrared vortex beam incident on a plasma mirror [64], and also by using a linearly polarized Gaussian laser incident on a plasma hologram [63]. In addition, theoretical studies have demonstrated the generation of xuv vortex beams from laser-plasma interactions driven at normal incidence in the reflected direction from thick (semi-infinite) targets [170], and in the transmitted direction from preformed micro-apertured targets [171].

In this work, we use ultrathin foils to demonstrate the generation of vortex harmonic beams in both the transmitted and reflected directions. We study the efficiency of the process on the laser-plasma parameters such as the target thickness, plasma density, laser amplitude, pulse duration, angle of incidence, as well as for more general elliptically polarized driving lasers. Importantly, we demonstrate that in this geometry it is possible to achieve comparable efficiencies to that of ultrathin foils driven by linearly polarized lasers as well as to that of circularly polarized lasers normally incident on preformed apertures. In addition, we show that the presence of OAM in the generated harmonics

is robust to deviations from normal incidences or perfectly circularly polarized driving lasers. However, for pure vortex modes, a circularly polarized laser at normal incidence is required.

Consider a circularly polarized (CP) laser normally incident on a flat, solid density plasma foil (figure 5.5). In a one-dimensional geometry, one would not expect the generation of harmonics in this case. For a CP laser at normal incidence there will be no longitudinal oscillation of the plasma surface as the laser's electric field is purely tangential to the target surface and the Lorentz force ($q\vec{V} \times \vec{B}$) is a slowly varying function of the laser amplitude. This is in contrast to a linearly polarized (LP) laser at normal incidence which will drive surface oscillations owing to the Lorentz force which oscillates at twice the laser's frequency (see figure 5.6 for a comparison of the reflected spectra for CP and LP driving lasers for 1D simulations). However, as was demonstrated previously [170, 171], it is possible to see harmonics in two or three-dimensional geometries by taking advantage of transverse effects. What are special about these harmonics is that they possess a twisted phase front characteristic of a vortex beam as schematically illustrated in figure 5.5. That is, these harmonics contain OAM. Before discussing more details of the emitted harmonics, we first take a detailed look at the plasma dynamics leading up to the emission of this radiation using ab-initio three dimensional particle-in-cell (PIC) simulations.

To understand the full plasma dynamics that ensues for a normally incident CP laser on an ultrathin foil, we perform full three-dimensional PIC simulations using the EPOCH code [74]. The laser has a normalized laser amplitude $a_o = eE_L/m\omega_L c = 40$, a pulse duration of $\tau_{fwhm} = 10T_L$, and a beam radius of $W_o = 4\lambda_L$. The foil is initialized as fully-ionized with a target thickness of 32nm ($D = d/\lambda_L = 0.04$) and a normalized plasma density of $N = n_e/n_c = 100$, where $n_c = m_e\omega_L^2/4\pi e^2$ is the plasma critical density. The leading edge of the foil is located at $x = 0$ and the laser is initialized at the left boundary and propagates along the x-axis. The simulation contains 10 computational particles per cell and has a spatial resolution of 32 cells per fundamental wavelength in each direction.

At times much before the arrival of the peak amplitude, the laser simply reflects off the

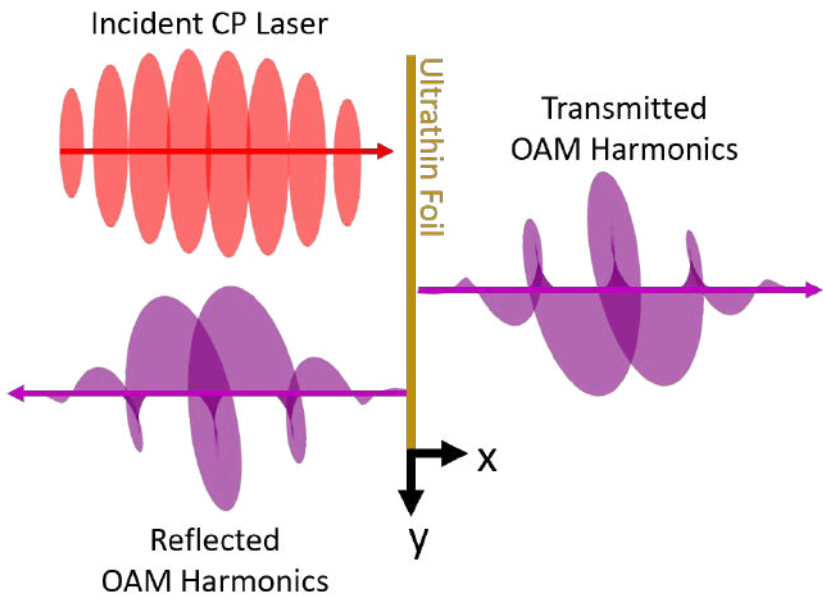


Figure 5.5: A schematic diagram of the proposed geometry for generating high-power ultraviolet and extreme ultraviolet vortex beams. A relativistically intense, circularly polarized laser with a Gaussian transverse profile (red beam) is normally incident on an ultrathin foil. The reflected and transmitted radiation contain harmonic orders of the driving laser's fundamental frequency which contain twisted wave fronts characteristic of vortex beams.

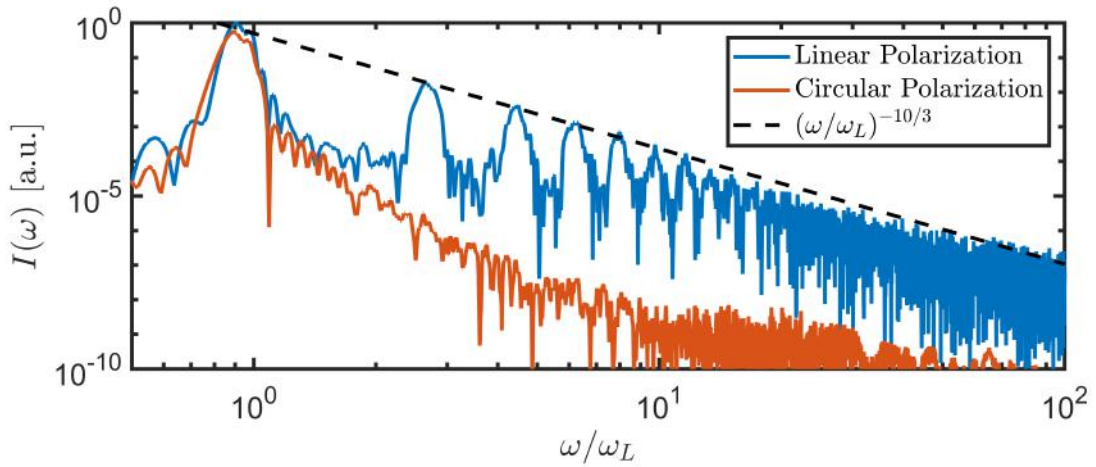


Figure 5.6: One-dimensional PIC simulation of harmonic generation from an ultrathin foil irradiated at normal incidence by a circularly polarized laser (red) and a linearly polarized laser (blue). Relevant simulation parameters: $\tau/T_L = 10$, $N = 100$, $a_0 = 80$, $\theta = 0^\circ$, $D = 0.20$, $\lambda_L/\Delta x = 1200$, particles/cell = 100, and $L = 0$.

flat, overdense plasma foil (figure 5.7a). During these cycles, just as in a one-dimensional geometry we do not expect to see the generation of harmonics. However, as the laser intensity builds up with the envelope of the pulse, the plasma surface begins to indent as a result of the Lorentz force. At this point, subsequent cycles now begin to locally see an oblique interaction at spatial locations away from the propagation axis (figure 5.7b). For a circularly polarized laser obliquely incident on the foil, the transverse electric field has a component in the longitudinal direction and hence will drive surface oscillations at the laser's frequency. As a result of these driven oscillations, we expect to see the emission of harmonic orders in the reflected direction.

As the laser pressure continues to build, the foil eventually breaks up leaving behind a micron-sized aperture for the remainder of the laser pulse to propagate through [figure 5.7(c-e)]. During this period we expect little harmonic emission to be emitted in the specular direction except possibly near the edges of the aperture where there is some curvature to the plasma surface that is not too oblique. It is possible, however, to see harmonic emission in the transmitted direction as a result of the relativistic oscillating window effect [171]. Here, the driving CP laser drives electron oscillations at the rim of the aperture leading to emission of harmonic radiation in the transmitted direction. In figure 5.9(c-f), the electron current density in the x -direction (longitudinal axis) is plotted in the transverse ($y-z$) plane at four instants of time over the course of a single laser cycle. Here we can see how the longitudinal current density varies in the azimuthal direction direction. We now proceed to describe the characteristics of the emitted harmonic generation in both the transmitted and reflected direction using results from these three-dimensional simulations.

The properties of the resulting transmitted and reflected harmonics are presented in figure 5.8. Here, the n^{th} harmonic is obtained by filtering the radiation in the range [$n - 0.5, n + 0.5$]. In the left panel, the longitudinal profiles of the first two harmonics are shown. Here we see that, while the fundamental harmonic remains Gaussian, the second harmonic has a higher-order transverse structure and most noticeably contains a null on-axis intensity. In the reflected direction the harmonics are primarily generated at the

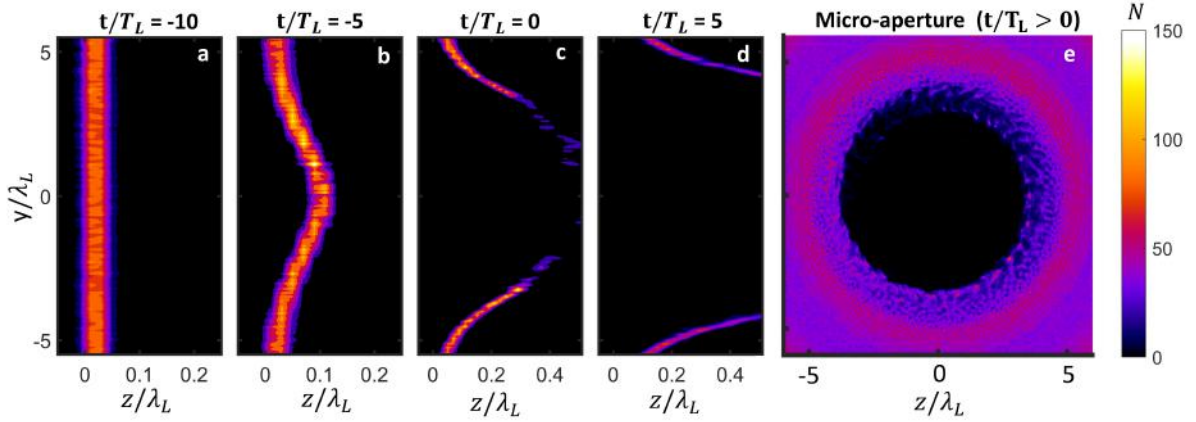


Figure 5.7: Three dimensional PIC simulations presenting the electron density evolution when a circularly polarized laser interacts with an ultrathin foil. (a - d) Contours of the electron density in the $x - y$ (longitudinal) plane at $z/\lambda_L = 0$ for four different time instants. The time $t/T_L = 0$ corresponds to the time when the peak of the laser envelope is at $x/\lambda_L = 0$. Here we see the onset of surface denting at early cycles and the eventual break up of the foil at later cycles. (e) Electron density in the $y - z$ (transverse) plane after the foil has broken up. Here we see that for $t/T_L > 0$ the laser will propagate through a micron-sized plasma aperture. The simulation parameters are the same as those used in figure 5.8.

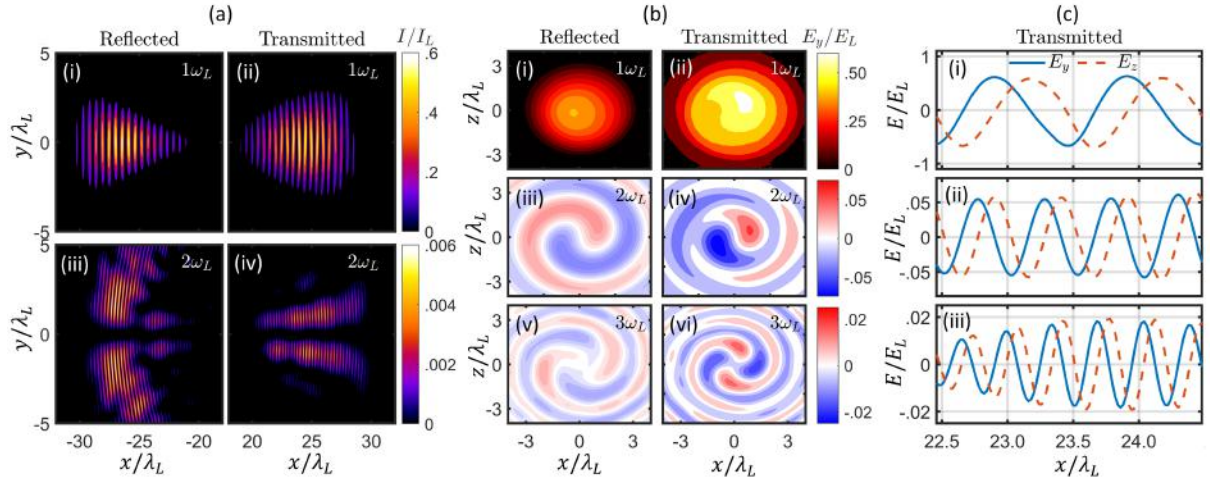


Figure 5.8: Reflected and transmitted harmonic radiation in the $x - y$ (longitudinal) plane (a), the $y - z$ (transverse) plane (b), and line-outs of the longitudinal fields along x (c). Although the fundamental beam remains Gaussian, the harmonic orders contain a null on-axis intensity and spiral phase fronts characteristic of a vortex beam. All harmonics remain circularly polarized as indicated by the equal amplitudes of the transverse electric fields and their 90° relative phase shift. Relevant simulation parameters: $\tau/T_L = 10$, $a_0 = 40$, $N = 100$, $W_0/\lambda_L = 4$, $\lambda_L/\Delta x = 50$, $\lambda_L/\Delta t_{\text{y}} = \lambda_L/\Delta t_{\text{z}} = 25$, particles/cell = 4, $D = 0.04$, and $L = 0$.

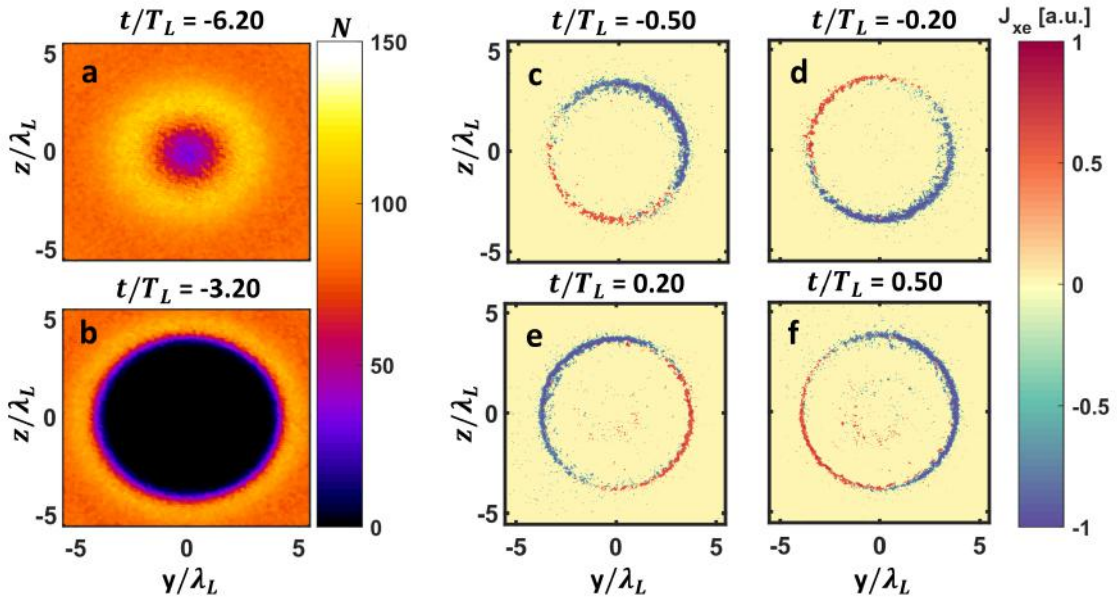


Figure 5.9: (a,b) Electron number density in the transverse plane at two different instants of time. The time $t/T_L = 0$ corresponds to the moment when the peak of the laser's temporal envelope reaches the front surface of the foil. Here we see the onset of surface denting at earlier times and the creation of a plasma window at later times. (c-f) Longitudinal electron current density at four different instants of time over the course of a single laser cycle. For this normally incident circularly polarized laser, the rotating surface oscillations in the longitudinal direction are induced by the transverse laser field. The simulation parameters are the same as those used in figure 5.8.

leading edge of the pulse as the foil has been dented but not yet experienced break-up. While the presence of a null on-axis intensity is one characteristic of a vortex beam, it is not a sufficient criteria to conclude that the beam possesses OAM as we also need to verify the presence of a twisted phase front by analyzing the transverse plane (central panel in figure 5.8).

Since the fundamental beam contains neither a null on-axis intensity nor a azimuthally-dependent phase front in the transverse beam, we conclude that the fundamental beam is not a vortex beam and contains no OAM. In contrast, it is clear that the second and third harmonics do contain an azimuthally-dependent phase front. As ϕ is varied from $[-\pi, \pi]$, the phase exhibits a 2π phase shift in the second harmonic and a 4π phase shift in the third harmonic. This is indicative of a topological charge of $l = 1$ and $l = 2$ for the second and third harmonics, respectively. In general, the n^{th} harmonic contains a topological of $l = n - 1$. It is important to note that all harmonics remain circularly polarized as indicated by the line out plots of the longitudinal field in the transmitted direction (right panel in figure 5.8). Here we see that both transverse components of the field contain roughly equal amplitudes with a relative phase shift of 90° .

The presence of OAM for harmonic orders is in agreement with the conservation of total angular momentum ($TAM = SAM + OAM$). From a photon point of view, harmonic generation can be understood as the destruction of n photons of frequency ω to create a single photon of frequency $n\omega$. In this process we also expect that the TAM of all n photons will be contained in the single photon at frequency $n\omega$. For the problem considered here, we see that all harmonic orders are circularly polarized so that each photon contains SAM of $1\hbar$. Thus, to conserve TAM, we would expect that the n^{th} order harmonic would contain OAM of $(n-1)\hbar$.

Now that we have explained the origin of the generated vortex harmonic beams as well as some properties of these harmonics, we move on to discuss the dependence of the process on various laser-plasma parameters. In particular, the dependence on harmonic generation efficiency as a function of target's thickness and density as well as the laser's duration and amplitude are considered. In addition, the laser's angle of incidence and

state of polarization is varied to determine the sensitivity of these properties of the driving laser to the generation of harmonics with OAM.

To conduct the parameter scans and achieve higher simulation resolution at a reduced computational cost, we drop down from 3D PIC simulations to 2D simulations. In a 2D geometry, we retain the ability to model the transverse effects necessary for harmonic generation. However, in a 2D geometry we lose the ability to fully observe the azimuthal variation of the phase in the transverse plane. We still can observe a null on-axis intensity as well as the phase of the field at $\phi = \{0, \pi\}$.

Harmonic generation from plasma mirrors is most efficient when the laser and plasma forces are approximately balanced [112, 116]. For most solid materials, the fully ionized plasma density is too high to be efficiently driven by present day ultra-intense lasers. A path toward achieving higher conversion efficiencies is to consider varying the foil thickness. The utility of thin foils arises from the fact that adjusting the foil thickness provides a way to adjust the effective plasma density. In this ultrathin foil regime, the harmonic efficiency is dependent on the total charge in the plasma (ND) rather than the plasma density or target thickness alone [112, 154]. For relativistic driving lasers ($a_o \gg 1$), the laser-plasma interaction is dependent on the relativistic similarity parameter, $S = N/a_o$, and so in the relativistic ultrathin foil regime the relevant similarity parameter is $SD = ND/a_o$.

In figure 5.10, we plot the third harmonic efficiency as a function of the charge contained within the foil normalized to the laser's amplitude (ND/a_o). The vertical dashed line is located at $ND/a_o = 1/\pi$ which corresponds to the point where the maximum laser pressure is perfectly balanced by the maximum plasma pressure when the electron slab is completely separated from the ion slab. In this plot, points to the right of the dashed line are for thick targets and the points to the left are for thin foils. The circles are for 2D simulations and the starred points are the corresponding 3D simulations showing reasonable agreement between the 2D and 3D PIC results.

In the transmitted direction we observe a peak in efficiency at $ND/a_o \approx 0.20$. For thicker targets, the laser does not borough through the foil and any generated third

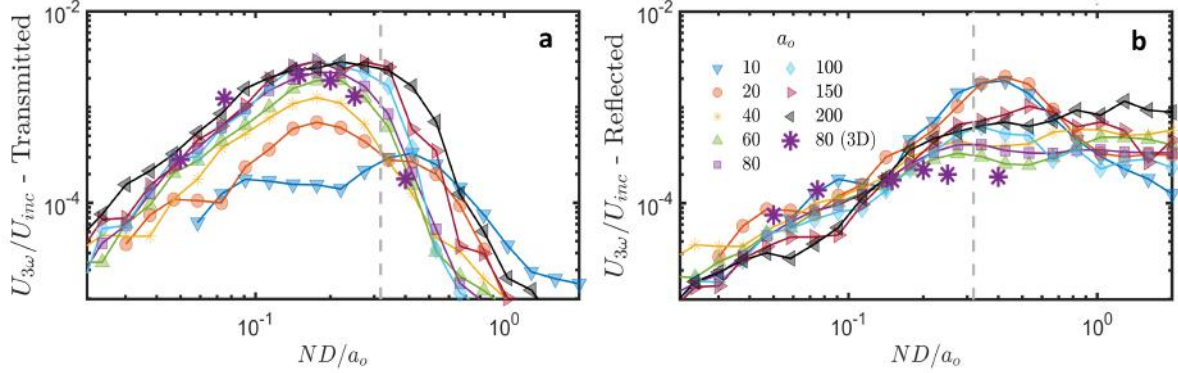


Figure 5.10: Third harmonic efficiency in the (a) transmitted and (b) reflected direction as a function of ND/a_0 for several values of D and a_0 . The plasma was irradiated by a normally incident, circularly polarized laser. The points marked with shaded symbols are for 2D simulations and those marked by a star are for 3D simulations. Relevant simulation parameters: $\tau/T_L = 10$, $N = 100$, $L = 0$, and $W_o/\Lambda_L = 4$. For 2D simulations, particles/cell = 15, $\lambda_L/\Delta x = 150$, and $\lambda_L/\Delta t = 50$. For 3D simulations, particles/cell = 4, $\lambda_L/\Delta x = 50$, and $\lambda_L/\Delta t = \lambda_L/\Delta z = 25$.

harmonic will be filtered out by the plasma. For thinner targets, the number of electrons coherently emitting radiation along the micro-aperture rim decreases which leads to a decrease in overall efficiency. On the other hand, for the reflected direction we see that the most efficient interactions take place for thick foils. This results from the fact that thinner foils will tend to break-up before the arrival of the center of the pulse so that a significant amount of the laser's energy goes into the transmitted direction.

From this parameter scan we can select the most efficient interaction and compare the result with other known geometries for generating xuv radiation from intense laser-foil interactions. In particular, it has been shown that when a LP laser is incident on an ultrathin foil there is a general $-10/3$ power-law exponent [112]. In addition, when a CP laser is incident on a preformed micro-aperture target, the relativistic oscillating window model predicts a -3.5 power-law scaling [171]. For the most efficient LP thick foil interactions, the power-law exponent can reach $-4/3$ [27]. In figure 5.12, we plot the line-out spectra from the most efficient interaction from our parameter scan and fit a power-law to the first six harmonic peaks yielding a -4.6 exponent. This is comparable to the exponents produced by the other known geometries. The advantage in this geometry is the simplicity of the set-up when compared with a preformed micro-aperture target

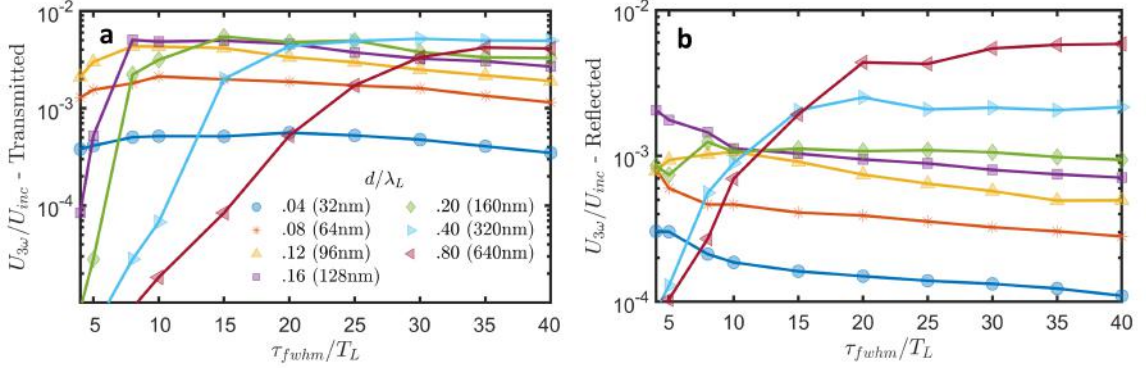


Figure 5.11: Two dimensional PIC simulations of the third harmonic efficiency in the (a) transmitted and (b) reflected directions as a function of τ/T_L for several values of ND/a_0 . Relevant simulation parameters: $\tau/T_L = 10$, $N = 100$, $a_0 = 40$, $L = 0$, $W_o/\Lambda_L = 4$, particles/cell = 10, $\lambda_L/\Delta x = 100$, and $\lambda_L/\Delta t = 40$.

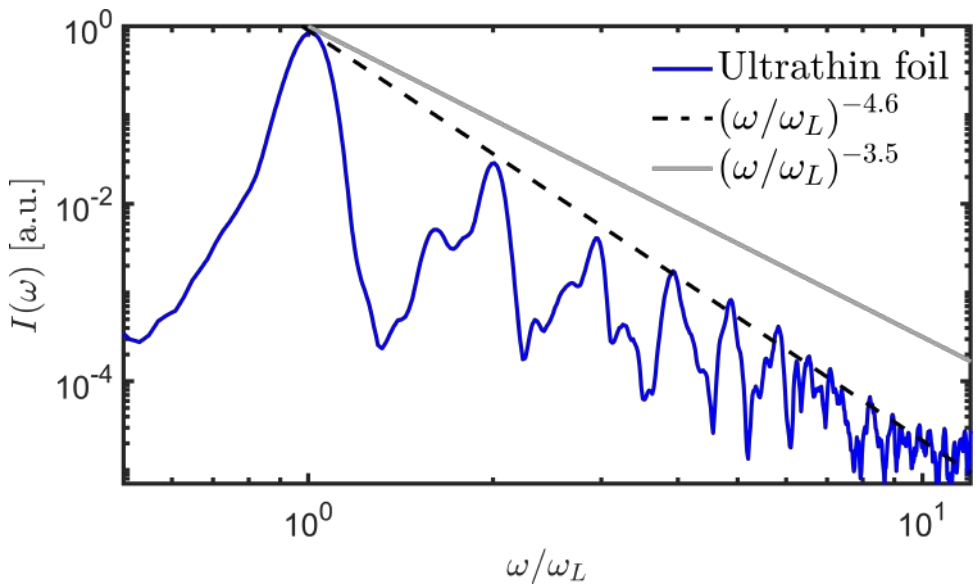


Figure 5.12: Spectral lineout plot from a 2D PIC simulation with parameters $N = 100$, $a_o = 80$, and $D = 0.18$. The dashed black line is a power-law fit to the first six harmonic orders. The grey solid line is the power-law scaling predicted when a CP laser is incident on a preformed micro-aperture [171], which is very close to the power-law exponent predicted when a linearly polarized laser irradiates an ultrathin foil [112].

and in the production of vortex harmonics carrying OAM when compared with an LP laser incident on an ultrathin foil.

In addition to the laser amplitude and target thickness, the laser's pulse duration is expected to play a crucial role in determining the harmonic efficiency. This is because the origin of the harmonic radiation critically relies on the surface denting and micro-aperture formation effect which takes many cycles to develop. If the laser pulse is too short, then we would expect no harmonic generation as the primary laser cycles will interact with a flat, solid-density target.

To this effect, we perform 2D PIC simulations with varied pulse duration from 2.7fs - 106.7fs ($1T_L$ - $40T_L$) for various target thicknesses. The third harmonic efficiency as a function of the pulse width for both the transmitted and reflected directions is presented in figure 5.11. In the transmitted direction, we see that for increasing pulse duration at a fixed D the efficiency first increases and then saturates. As the target thickness is increased, we need a longer pulse duration to reach the saturation of efficiency which will be greater than a thinner target at its saturation point. This makes sense since a thicker target will require a longer pulse duration to drill the micro-aperture. The aperture for this thicker target allows for enhanced harmonic efficiency as a result of the greater number of electrons that coherently emit the radiation. If the foil thickness is too large, then the efficiency will begin to decrease as at this thickness the laser cannot effectively drill through the plasma. For the reflected direction we see that longer pulses and thicker targets produce the most efficient harmonics.

The emission of harmonics for a CP laser at normal incidence on an ultrathin foils critically relies on the transverse effects such as surface denting and micro-aperture formation. In contrast to normal incidence, a CP laser obliquely incident on a flat solid target will lead to efficient harmonic generation even in a 1D geometry. This makes oblique interactions more desirable as they do not require wasted energy to go into surface denting or hole drilling of the plasma surface. The desire to work at oblique incidences is also motivated by more practical concerns. Experimentally, it is challenging to work at normal incidences as back reflection of the intense laser can lead to damage of the laser

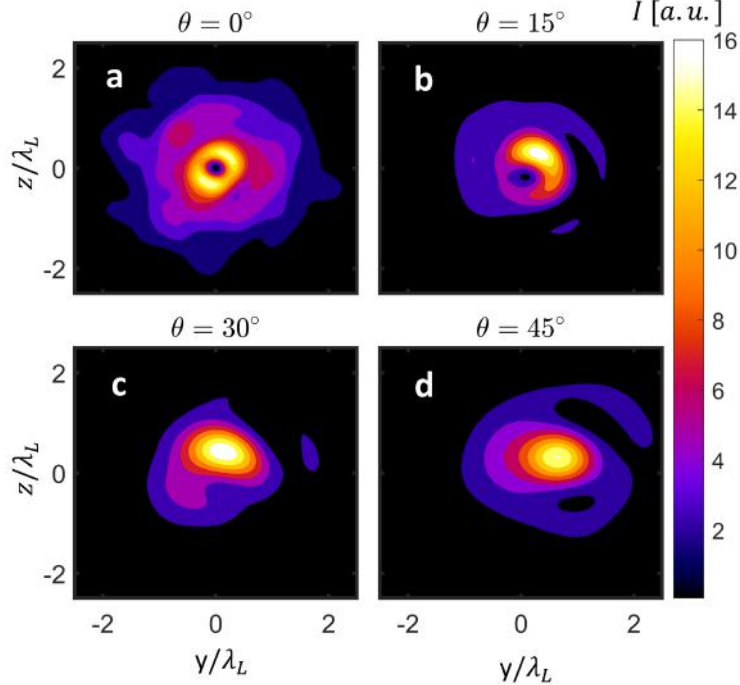


Figure 5.13: Second harmonic intensity summed along the propagation axis for four different angles of incidences. Relevant simulation parameters: $\tau/T_L = 15$, $a_0 = 40$, $N = 100$, $W_0/\lambda_L = 4$, $\lambda_L/\Delta x = \lambda_L/\Delta y = \lambda_L/\Delta z = 30$, particles/cell = 2, $D = 0.10$, and $L = 0$.

system. In addition, measuring the reflected beam in a normal incidence geometry is cumbersome, albeit not impossible.

However, for an oblique interaction, it is not clear whether or not the generated harmonics will contain OAM. To check for this we perform a set of 3D PIC simulations with varied angle of incidence and all other parameters the same as in figure 5.8. The summed axial intensity of the second harmonic generated in the transmitted direction from four different angles of incidence is plotted in figure 5.13. For $\theta = 0^\circ$ we see the donut-shaped intensity profile characteristic of a vortex beam. For $\theta = 15^\circ$ there is still a null on-axis intensity, however, the intensity distribution surrounding the center is no longer symmetric. At even higher angles of incidence, the donut-shaped intensity profile vanishes. The loss of the azimuthally-dependent phase in the transverse plane which gives rise to the on-axis intensity singularity means that, while oblique interactions are a route toward higher harmonic efficiencies for a CP laser incident on an ultrathin foil, the resulting harmonics are not vortex beams.

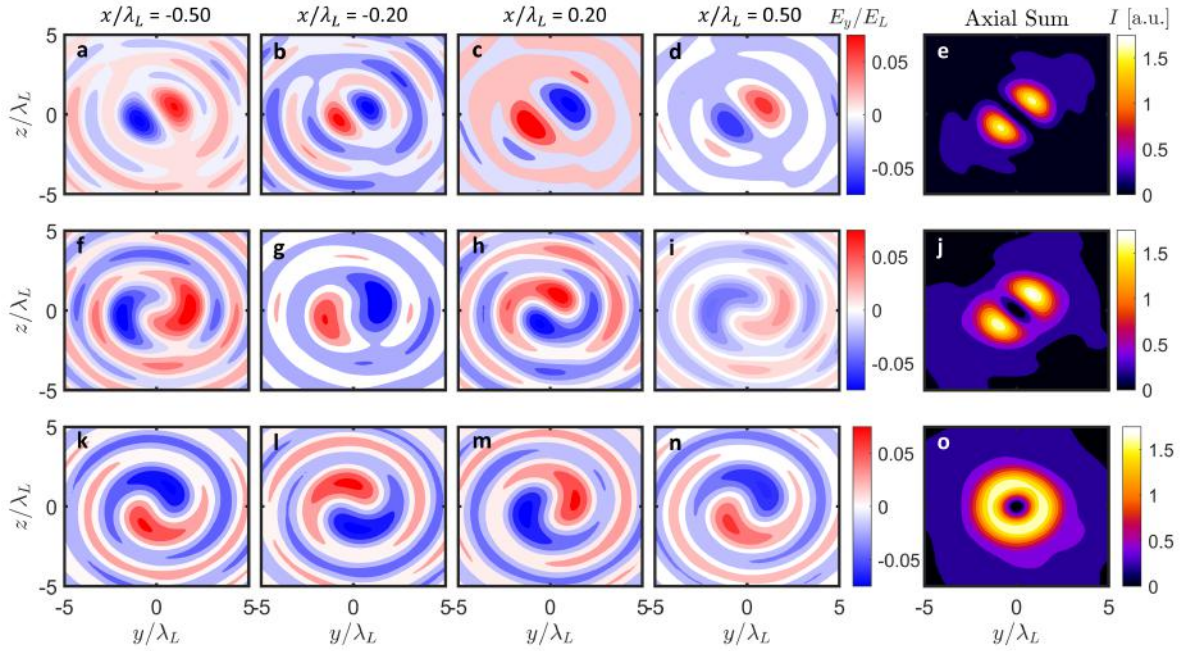


Figure 5.14: The transverse laser profile of the emitted second harmonic for various polarization states of a relativistically intense laser normally incident on an ultrathin foil. Each row corresponds to a different polarization state all of which have equal amplitudes in each of the two orthogonal components of the electric field and relative phases (top row) 0, (middle row) $\pi/4$, and (bottom row) $\pi/2$. The first four columns show the evolution of the transverse profile near the center of the laser pulse. The fifth column shows the axially-summed intensity. Relevant simulation parameters: $N = 100$, $a_0 = 80$, $\tau/T_L = 12$, $D = 0.12$, $L = 0$, $W_0/\lambda_L = 4$, particles/cell = 4, $\lambda_L/\Delta x = 60$, $\lambda_L/\Delta y = \lambda_L/\Delta z = 20$.

Previously, it has been shown that for LP lasers normally incident on an ultrathin foil will produce high-order transverse modes in the transmitted emitted harmonics which are characteristic of the Hermite-Gauss ($HG_{m,n}$) modes where m and n are the indices characterizing the mode order [153]. In this work we showed that a CP laser normally incident on an ultrathin foil produces Laguerre-Gauss (LG) modes. However, what the transverse structure looks like for more general elliptically polarized lasers has not been studied before. To this effect, we run several 3D PIC simulations with a varied polarization state at normal incidence. The results are summarized in figure 5.14 for which the second harmonic in the transverse plane is plotted. Each row pertains to a different polarization state of the driving laser where all three cases have equal amplitudes in the two transverse electric fields but different relative phases. In the first row, the two transverse electric fields of the driving laser are in-phase which produces a linearly polarized laser.

The resulting transverse structure is best described as a $HG_{0,1}$ mode rotated by 45° . It is also interesting to note that a 45° rotated $HG_{0,1}$ can be written as a superposition of the two non-rotated modes $HG_{0,1} + HG_{1,0}$ which are in-phase [165].

In this way, we can understand what to expect as the state of the polarization of the driving laser is varied. A more general state of elliptical polarization will yield a superposition of these two HG modes with a relative phase between them corresponding to the relative phase of the elliptically polarized driving laser. The resulting field produces an imperfect Laguerre-Gauss mode as shown in the middle row of figure 5.14. In the special case of circular polarization we have the superposition of the two non-rotated modes $HG_{0,1} + HG_{1,0}$ which are $\pi/2$ out of phase which is known to yield a Laguerre-Gauss mode [165].

In conclusion, we have demonstrated the generation of vortex harmonics from an ultrathin foil irradiated at normal incidence by a CP laser in both the reflected and transmitted directions. Through tuning of the laser-plasma parameters we were able to find efficiency regimes comparable to pre-formed micro-aperture or ultrathin foils driven by linear polarized lasers. Finally, we showed that to produce pure Laguerre-Gauss modes one needs to use a CP laser at normal incidence where more general elliptically polarized lasers at oblique incidence may produce more intense harmonics but the vortex structure will be lost.

5.3 Attosecond pulse interference and harmonic structure

Specular reflection of intense lasers from relativistic plasma mirrors produces a source of high-power, broad bandwidth radiation which, in addition to being a useful secondary light source for probing electron dynamics, encodes the information of the complex plasma dynamics that takes place during extreme light-matter interactions [60, 172]. The appearance of harmonic peaks in the reflected spectrum can be explained as a result of periodically spaced attosecond pulses emitted once every laser cycle. For multi-cycle

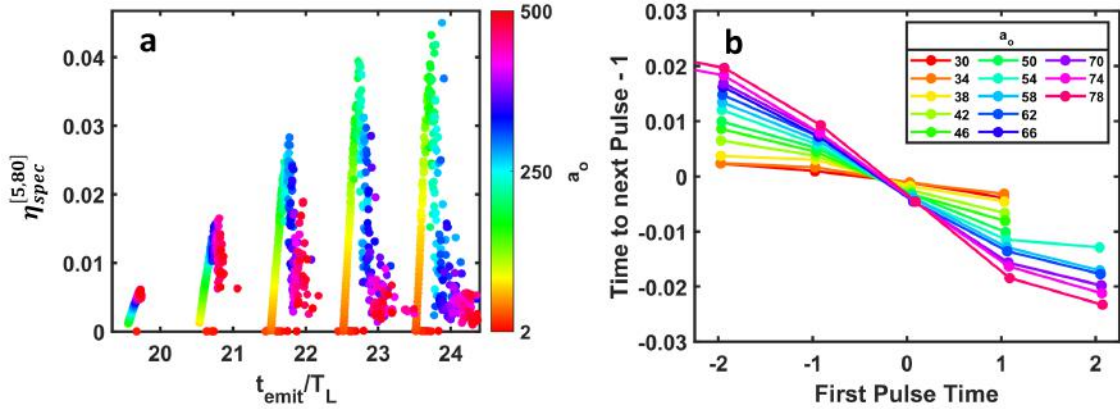


Figure 5.15: Variation in emission timing of attosecond pulses for a multi cycle driving laser and varied laser amplitude. (a) Spectral efficiency as a function of emission timing of the first five attosecond pulses within the attosecond pulse train. (b) Difference in emission timing between consecutive attosecond pulses within the train. Relevant simulation parameters: $N = 400$, $\theta = 30^\circ$, $\tau/T_L = 7$, $L = 0$, $\lambda_L/\Delta x = 1200$, particles/cell = 200, and $D = 2$.

laser pulses, cycle-to-cycle emission times of attosecond pulses varies due to evolving laser and plasma parameters. In this section, we use one-dimensional particle-in-cell simulations to map the temporal spacing of attosecond pulses to different observed harmonic structure, including harmonic broadening, harmonic splitting, and the appearance of integer and half-integer harmonics, all of which have been seen in previous experiments [57, 173, 174]. We demonstrate how a small amount of temporal chirp applied to the driving laser can compensate for the non-periodic emission time of attosecond pulses which results in narrower, more intense individual harmonics. The results of this section provides insight into the rapidly evolving plasma dynamics of intense laser-solid interactions and how these dynamics are encoded in the reflected radiation.

In section 2.2.2, we showed that values of $a_0/N \gtrsim 0.2$, the emission timing of attosecond pulses occurred at times exceeding $0.5T_L$ as a result of the large displacement of the electron surface from the initial plasma-vacuum interface. To understand how this plays a role in attosecond pulse emission timing for multi-cycle interactions where the ratio of a_0/N changes for each cycle in consecutive cycles, we perform a set of simulations with $\tau/T_L = 7$ and varied a_0 at $N = 400$ and $\theta = 30^\circ$ and track the separation in time of attosecond pulses within the train. In figure 5.15(a), we plot the spectral efficiency of the

emitted attosecond pulse in the frequency range $5 < \omega/\omega_L < 80$ as a function of time. The colorbar indicates the value of a_0 . To compute the spectral efficiency of each attosecond pulse within the attosecond pulse train, each attosecond pulse is isolated with a Gaussian temporal window of width $0.5T_L$ before Fourier transforming to the frequency domain. The location in time of the attosecond pulse is determined by the maximum value of the attosecond pulse intensity. Here we see that as a_0 increases, the emission timing of each attosecond pulse is delayed in time. At the highest values of a_0 , the emission timing of the attosecond pulse can be delayed by as much as $0.5T_L$. This can have substantial impact on subsequent cycles which is indicated by the decrease in spectral efficiency for cycles near the pulse center compared to cycles near the pulse's wings, which locally has a lower value of a_0 . At these values of a_0 , the single cycle approximation used throughout this thesis no longer holds.

In figure 5.15(b), the difference in emission timing between consecutive attosecond pulses is plotted as function of pulse number within the attosecond pulse, where 0 indicates the attosecond pulse emitted at the center of the pulse envelope. For $a_0 \lesssim 40$, the difference in pulse timing is close to zero for all pulses in the pulse train, which means the attosecond pulses are periodically separated. These results are in agreement with experiments performed in the relativistic regime for moderate laser intensities [40]. For $a_0 \gtrsim 40$, we observe a negative slope in attosecond pulse separation which is first greater than periodic spacing on the leading edge of the pulse and then drops to less than periodic spacing on the back end of the driving laser. For these simulations, we expect the distortions to the comb of harmonics predicted for the case of periodic spacing.

In figure 5.16, we plot the attosecond pulse train [figure 5.16(a)] and reflected spectrum zoomed in to the frequency range of $10 < \omega/\omega_L < 25$ [figure 5.16(b)] for the case of $a_0 = 40$. The blue line in both figures indicates the total reflected field. In the reflected spectra, we can see broadening of the harmonics beginning at $\omega/\omega_L \approx 14$ which becomes progressively broader for higher orders. To understand the effect that non-periodic emission timing of attosecond pulses has on the spectrum we use a Tukey window to isolate just two consecutive attosecond pulses within the attosecond pulse train and take the Fourier

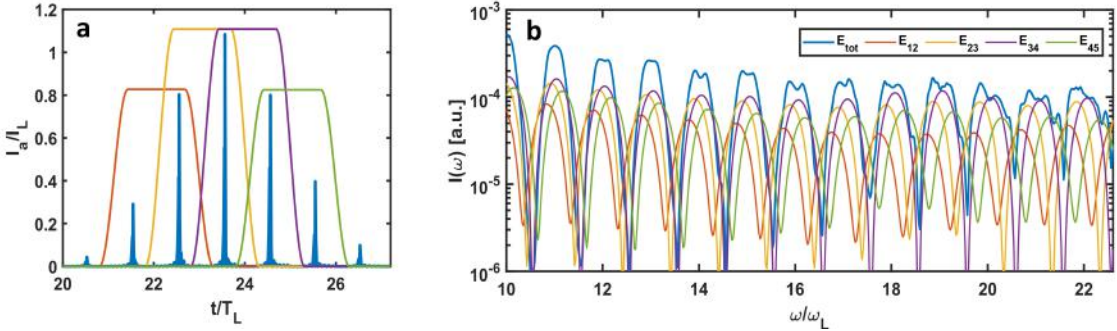


Figure 5.16: Illustration of harmonic broadening as a result of non periodic emission timing between attosecond pulses for the case of $a_0 = 40$. (a) The attosecond pulse train as observed in the time domain. (b) The total reflected spectrum (blue) and the spectrum of two neighboring attosecond pulses. Here we see how the sum of individual spectral components of the attosecond pulses add to yield the broadened final spectrum. All other simulation parameters are the same as those presented in figure 5.15.

transform of the resulting field. The red, yellow, purple, and green windows shown in figure 5.16(a) correspond to the same colored spectra shown in figure 5.16(b). At the leading edge of the pulse train, the longer than periodic separation times between attosecond pulses leads to smaller differences between the peaks of harmonics and vice-versa for the shorter separation times at the trailing edge of the attosecond pulse train where the attosecond pulse separation times have less than periodic spacing. The net result is a broadening of harmonic intensit which gets progressively worse at larger values of ω/ω_L .

The linear decay in separation timing between attosecond pulses suggests that a return to periodic spacing can be obtained by linearly chirping the pulse in time. To test for this we run a set of simulations where the incident pulse is negatively chirped [figure 5.17]. As the negative chirp increases from $GVD = 0 fs^2$ to $-2000 fs^2$, the harmonic width (δ_h) of both low order harmonics ($n_h = 10$) and high order harmonics ($n_h = 30$) decreases until all harmonic orders have nearly the same width [figure 5.17(a)]. The harmonic width is calculated as the full-width-half maximum of the harmonic peaks centered at n_h . In addition to narrowing the harmonic orders, indicating the near periodic spacing of all attosecond pulses within the pulse train[figure 5.17(c)], the intensity of individual harmonic orders increase, which will ultimately make detection easier near the noise threshold of spectrometers [figure 5.17(b)]. Since the chirped laser pulse decreases

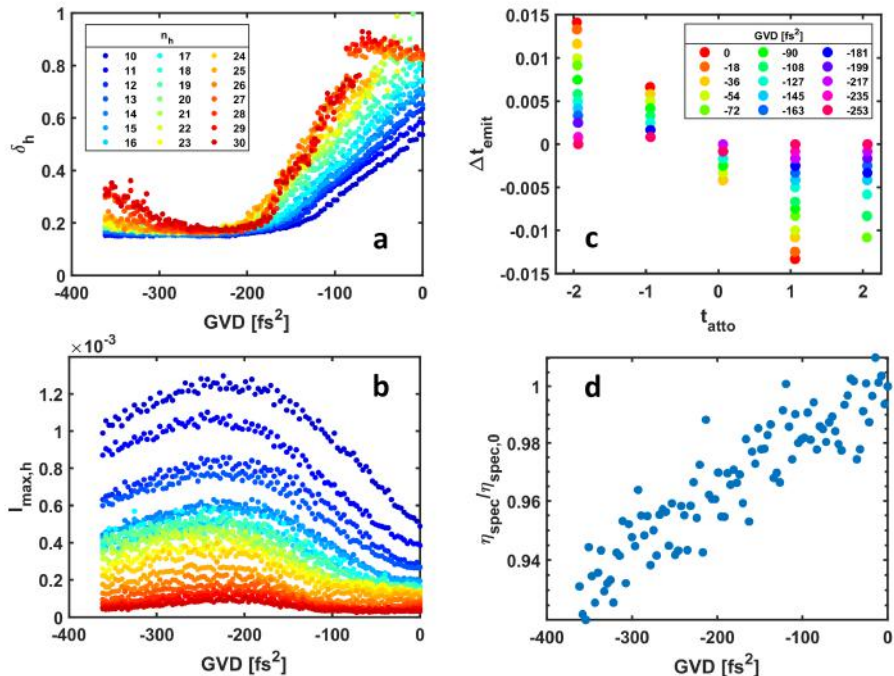


Figure 5.17: Effect of chirped driving lasers on (a) the harmonic width, δ_h , and (b) the harmonic intensity. For the case of $a_0 = 10$, (c) shows the control of the relative timing between attosecond pulses and (d) shows the expected reduction in efficiency for a chirped pulse. Relevant simulation parameters: $N = 400$, $\theta = 30^\circ$, $\tau/T_L = 7$, $L = 0$, $\lambda_L/\Delta x = 1000$, particles/cell = 100, and $D = 2$.

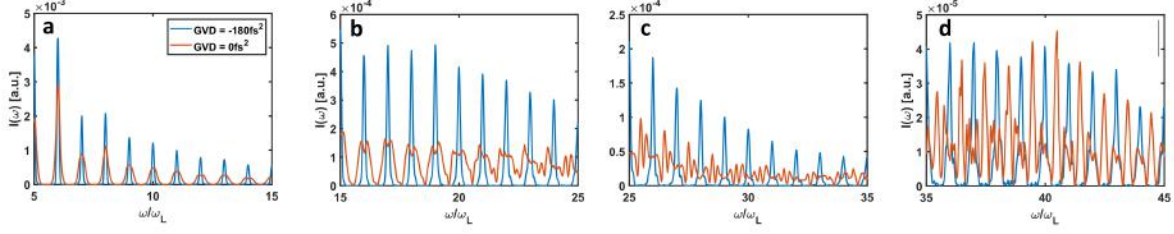


Figure 5.18: Comparison of the reflected spectrum for the cases of an unchirped (red) and negatively chirped (blue) incident laser. Relevant simulation parameters: $N = 400$, $a_0 = 10$, $\theta = 30^\circ$, $\tau/T_L = 7$, $L = 0$, $\lambda_L/\Delta x = 1000$, particles/cell = 100, and $D = 2$.

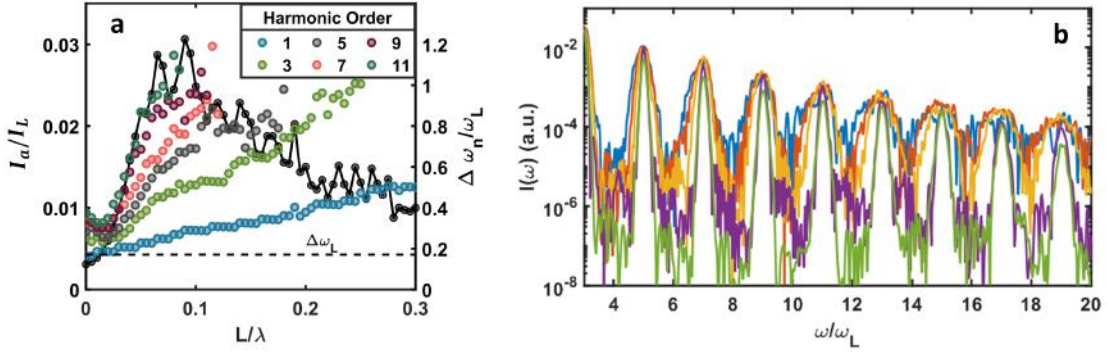


Figure 5.19: Broadening of harmonic orders as a function of the pre-plasma gradient length scale. (a) Harmonic width (colored circles) and peak attosecond pulse intensity (solid black line) as a function of the pre-plasma gradient scale length. (b) Illustration of the harmonic broadening for selected values of L . Relevant simulation parameters: $N = 200$, $a_0 = 5$, $\theta = 0^\circ$, $\tau/T_L = 7$, $\lambda_L/\Delta x = 1000$, particles/cell = 100, and $D = 2$.

the intensity of the driving laser, we see a drop in reflected spectral efficiency [figure 5.17(d)], but only by about 5% for a GVD value which maximizes harmonic intensity. The comparison of the spectra in different frequency ranges for the case when $GVD = 0$ and $-180 fs^2$ and is shown in figure 5.18.

Harmonic broadening can also occur for low values of $a_0 < 40$, if there is a preplasma gradient scale length. In figure 5.19(a), we plot the harmonic width, $\Delta\omega_n/\omega_L$, for odd order harmonics as a function of the pre-plasma gradient scale length L , showing that harmonics become progressively broader with increasing L . In addition, in figure 5.19(a), the attosecond pulse efficiency (black dots) is plotted on the left axis, showing that the maximum L occurs at 0.1. The broadened spectra for different L are shown in figure 5.19(b).

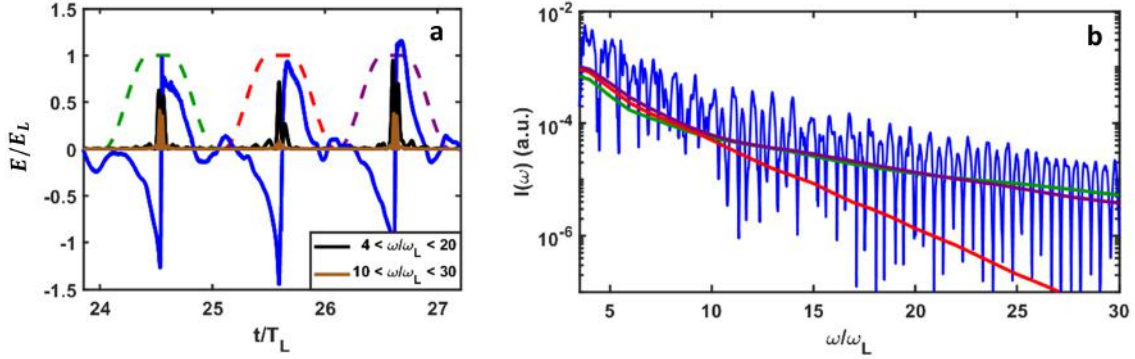


Figure 5.20: The appearance of half integer harmonics as a result of attosecond pulses with spacing at twice the incident laser's period. (a) The reflected field with the attosecond pulse train filtered in different frequency windows showing the disappearance of the center attosecond pulse at high frequencies. (c) Spectrum of the total reflected field and the individual spectra of the attosecond pulses. The earlier spectral cut off of the center attosecond pulse results in the appearance of integer and half integer harmonics. Relevant simulation parameters: $N = 400$, $a_0 = 5$, $\theta = 45^\circ$, $\tau/T_L = 8$, $L = 0.2$, $\lambda_L/\Delta x = 800$, particles/cell = 80, and $D = 2$.

The highest efficiency interactions take place under conditions such that the plasma and laser parameters change drastically from cycle to cycle. In figure 5.20, the attosecond pulse train and reflected spectra are shown in figures 5.20(a) and 5.20(b), respectively, for a simulation with a relatively long $L = 0.2\lambda_L$ pre-plasma gradient scale length. In this simulation, we see that the attosecond pulse which is emitted at $t/T_L = 25.5\text{fs}$ is substantially weaker than the ones emitted before and after it. This results in the appearance of half integer harmonics in the reflected spectra. Under such extreme conditions, an appeal to pattern recognition algorithms may be needed to extract information on the experimental conditions based on the spectral features [175].

In conclusion, in this section, we used one dimensional particle in cell simulations to explain the appearance of different types of harmonic structure present in the reflected light from a relativistic plasma mirror. The harmonic structure arises due to non-periodic spacing of attosecond pulses within the attosecond pulse train. These observations allow us to connect the properties of the reflected field to the complex relativistic plasma dynamics.

5.4 Elliptically polarized incident lasers and the emission of co- and counter-rotating harmonics

Relativistic high harmonic generation (RHHG) from plasma mirrors emit intense, phase-matched harmonics of the driving laser’s fundamental with sufficient bandwidth to support attosecond pulses [26, 27, 38]. Emission of these extreme ultraviolet attosecond pulses is accurately described within the coherent synchrotron emission (CSE) model, which ascribes the emission to dense bunches of electrons accelerated in synchrotron-like trajectories [27, 47, 49]. By controlling these electron trajectories with tailored driving lasers and structured plasmas, RHHG has been proposed for controlling the temporal, spatial, spectral, and polarization properties of the radiated harmonics, allowing for the generation of vortex harmonics and other higher-order transverse modes [64, 153, 170, 171], circularly polarized (CP) harmonics [176–179], isolated attosecond pulses [180, 181], and multi-color temporal waveforms [114, 115, 128]. A strong motivation for using plasma-based media for harmonic generation is the favorable scaling of the process with intensities beyond the ionization threshold of gas or solid-state media, allowing for the brightest high-order harmonics and attosecond pulses.

The polarization state of emitted harmonics from plasma mirrors are governed by a set of selection rules which predict the polarization state of radiated harmonics when given the polarization state of the driving laser [44]. Most previous work on RHHG utilized P-polarized driving lasers since they offer the most efficient conversion efficiencies. However, several works have reported on the prospect of achieving a polarization-controlled harmonic source from plasma mirrors by tuning the ellipticity of a single driving laser [176, 178, 179, 182] or by using a two laser configurations [183–187], where the later also allows for enhanced harmonic efficiency and additional spectral control compared to a single laser alone. Although parameter scans of single-color interactions have been discussed, showing CP attosecond pulse emission for several configurations of the driving laser’s ellipticity, a detailed analysis of the electron bunch dynamics leading up to emission for these configurations is missing.

In this section, we use one and two-dimensional particle-in-cell (PIC) simulations to investigate the attosecond electron bunch dynamics leading up to the emission of CP harmonics from plasma mirrors driven by single-color, elliptically polarized lasers. First, we show that tuning the driving laser's ellipticity yields two regimes in which nearly CP harmonics and attosecond pulses can be generated. The first is when the driving laser is nearly CP polarized, for which the emitted harmonics co-rotate with the reflected fundamental, and the second is when the driving laser is nearly S-polarized, for which the emitted harmonics counter-rotate with the reflected fundamental. We then analyze the electron number density and current density dynamics and the emitted attosecond pulses in detail for different polarization states of the driving laser. We find that S-polarized driving lasers emit CP attosecond pulses every half cycle, where consecutive attosecond pulses in the train have opposite helicity. By converting a small fraction (1-10%) of a purely S-polarized driving laser to the P-polarized component, one of the two attosecond pulses are suppressed and the other enhanced, yielding a CP attosecond pulse train. Although P-polarized interactions remain the most efficient, we show that P and CP interactions can reach comparable peak efficiencies, and both have higher peak efficiencies than S-polarized interactions. We conclude by demonstrating a practical approach for constructing bi-color co- and counter-rotating terawatt laser beams for chirality-sensitive nonlinear experiments.

The PIC simulations model the interaction of a realistically intense laser obliquely incident on a fully ionized, overdense plasma. The ellipticity of the incident laser is varied by adjusting either the phase difference between the S- and P-polarized components of the laser or by adjusting the fraction of energy contained in the S-polarized component, I_s/I_L . The laser has a Gaussian profile in both space, with a spot size W_0 , and time, with a full-width-half-maximum pulse duration of τ , and has a normalized laser amplitude of $a_0 = eE_L/(m\omega_L c)$, where e and m are the charge and mass of an electron, $E_L \propto \sqrt{I_p^2 + I_s^2}$ is the electric field strength at the center of the pulse's envelope, ω_L is the central laser frequency, and c is the speed of light. The semi-infinite plasma target has a pre-plasma gradient modeled as an exponential with a characteristic scale length L up until the

target's peak electron number density, N , which has been normalized by the plasma critical density $n_c = m\omega_L^2/(4\pi e^2)$. We define the $x - y$ plane as the plane of incidence, where the targets normal vector points in the $-x$ direction. This means that the S-polarized component of the electric field points in the z -direction. In all simulations, all three velocity and field components are retained to allow for arbitrary polarization states to be constructed while only one or two spatial dimensions are modeled. For one-dimensional oblique interactions, a Lorentz transform to a boosted frame is used [117, 118].

In this work we are interested in analyzing efficiency and ellipticity of the reflected harmonics and attosecond pulses. To analyze individual harmonics, we take a Fourier transform of the reflected laser in each of the two orthogonal polarization directions and apply a filter to the spectrum, zeroing out all radiation outside the frequency range $n-0.5 < \omega/\omega_L < n+0.5$, which isolates the n^{th} harmonic order. Attosecond pulses are analyzed similarly, but where the filter is applied over a larger spectral window ($\omega_{LF} < \omega/\omega_L < \omega_{UF}$). The spectral efficiency, $\eta_{spec}^{[\omega_{LF}, \omega_{UF}]}$, is defined as the energy contained in both components of the reflected field's spectrum normalized by the energy contained in the incident laser's spectra. The ellipticity of the reflected beam is calculated as the average of $2E_p E_s \sin(\delta)/(E_p^2 + E_s^2)$, where δ is the phase difference between E_p and E_s . This definition corresponds to the normalized Stokes parameter which measures the degree of circular polarization in the right-handed (+1) or left-handed (-1) states as viewed from an observer toward whom the wave is moving [188]. [Note this means that I am choosing two different observers: one for the incident beam and one for the reflected beam. Maybe it is better to pick a fixed lab coordinate for the observer (i.e. an observer positioned at the target or one in which the laser is always moving toward/away from the observer)]

In Fig. 5.21(a), the relative fraction of energy contained in the S and P components of the reflected harmonics is plotted as a function of I_s/I_L . The phase between the S and P components of the incident laser was set to $\pi/2$, so that the incident laser is CP when $I_s/I_L = 0.5$. For odd ordered harmonics, the fraction of energy contained in the S-polarized component experiences a monotonic increase from purely p-polarized to purely

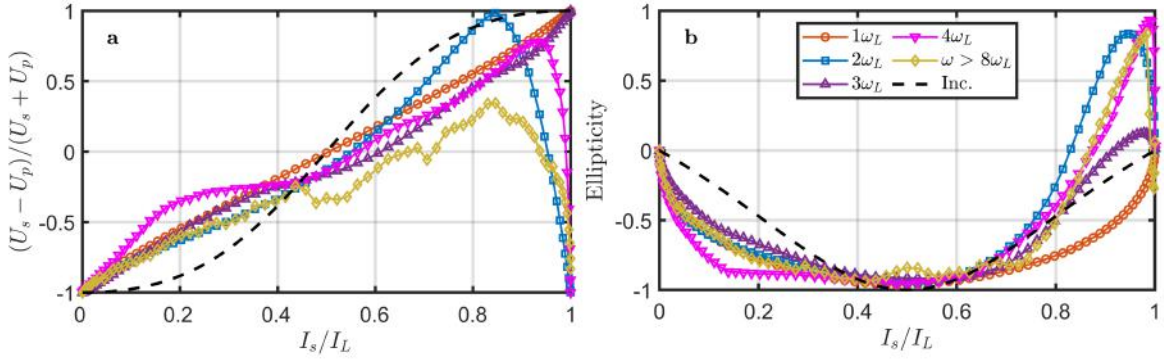


Figure 5.21: Two-dimensional particle-in-cell simulations characterizing the polarization state of the reflected harmonics as a function of the fraction of energy contained in the S-polarized component of the driving laser, I_s/I_L . (a) Relative fraction of energy between the P-polarized and S-polarized component for the first four reflected harmonics and superposition of harmonic orders greater than 8. (b) is the same as (a) except that the y-axis measures the ellipticity of the reflected beam. An ellipticity of ± 1 indicates right-handed and left-handed states, respectively. Simulation parameters: $a_0 = 10$, $N = 400$, $\theta = 45^\circ$, $\tau/T_L = 8$, $W_o/\lambda_L = 4$, $L = 0.05$, $I_s/I_L = \text{varied}$, $\phi_{sp} = \pi/2$, $\lambda_L/\Delta x = \lambda_L/\Delta y = 280$, and particles/cell = 7.

s-polarized, in conjunction with the incident driving laser. For even ordered harmonics and the superposition of higher order harmonics, the fraction of energy contained in the S-polarized component first increases together with odd-ordered harmonics, but eventually peaks and rapidly drops to -1 in agreement with the selection rules of harmonic generation which predicts P-polarized odd harmonics and S-polarized even harmonics for when $I_s/I_L = 1.0$. Here we are interested in the cases where the reflected harmonics have $U_S \approx U_P$, which is one criteria for CP harmonics. For odd harmonics, this happens only once when $I_s/I_L \approx 0.5$, but for even harmonics this happens twice: once when $I_s/I_L \approx 0.5$ and again at a value of I_s/I_L which depends on the harmonic order but is greater than 0.90.

The second criterion for CP harmonics is that $\delta = \pm\pi/2$, where the sign determines the helicity of the reflected harmonic. In Fig. 5.21(b), the ellipticity is plotted as a function of I_s/I_L . When $I_s/I_L \approx 0.5$, all harmonic orders have an ellipticity close to -1, which is the same as that of the reflected fundamental. In contrast, for $I_s/I_L > 0.90$, the even ordered harmonics and superposition of high-order harmonics reach a maximum ellipticity close to 1, which is an opposite orientation to the reflected fundamental. Therefore,

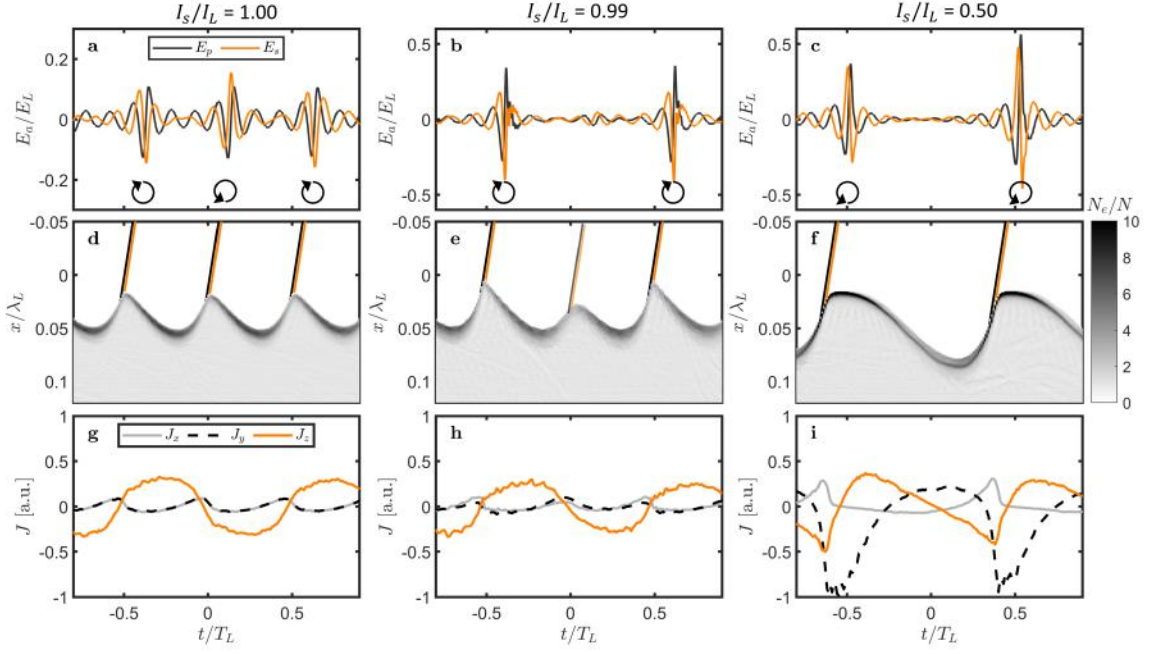


Figure 5.22: One-dimensional particle-in-cell simulation of the attosecond pulse train (a-c), space-time electron number density contours (d-f), and the electron current density at the front surface of the electron number density for $I_s/I_L = 1.0$ (a,d,g), 0.99 (b,e,h), and 0.50 (c,f,i). The plots show only the attosecond pulses and plasma dynamics for a few laser cycles near the center of the pulse envelope. In a-c, the arrows indicate the helicity for each individual attosecond pulse. In d-f the black and orange lines mark the trajectory of attosecond pulses after emission. Simulation parameters: $a_0 = 160$, $N = 400$, $\theta = 45^\circ$, $\tau/T_L = 5$, $L = 0$, $I_s/I_L = \text{varied}$, $\phi_{sp} = \pi/2$, $\lambda_L/\Delta x = 1000$, and particles/cell = 100.

while interactions with $I_s/I_L = 0.5$ produce harmonics which co-rotate with the reflected fundamental, interactions with $I_s/I_L > 0.90$ produce harmonics which counter-rotate with the reflected fundamental.

Although CP harmonics were expected for the case when $I_s/I_L \approx 0.5$, it is not at first clear why CP harmonics are emitted when $I_s/I_L \approx 1$ and why the two regimes have opposite helicity. To gain insight into this phenomena we investigate the plasma dynamics leading up to the emission of the attosecond pulses. Fig.5.22 plots the emitted attosecond pulses (a-c), space-time density contours (d-f), and the electron current density (g-i) for the cases when $I_s/I_L = 1.0$, 0.99, and 0.5 and $\phi_{sp} = 90^\circ$. For these figures, only a few cycles near the central envelope are shown. For $I_s/I_L = 1.0$, we observe the emission of an attosecond pulse train with half-period spacing in which all attosecond pulses have a $\pm\pi/2$ phase difference, in agreement with previous theoretical work [185]. Furthermore,

the S and P amplitudes are nearly the same so that each attosecond pulse in the train is circularly polarized. However, note that consecutive attosecond pulses in the train have opposite helicity, as indicated by the arrows located beneath each attosecond pulse, so that the averaged ellipticity across the entire attosecond pulse train is nearly zero, which in the frequency domain manifests itself as linearly polarized harmonics. That is, s-polarized driving lasers emit linearly polarized harmonics and circularly polarized attosecond pulses. The change in helicity for consecutive attosecond pulses can be understood by analyzing the electron current density [Fig. 5.22(g)], where we see that J_x and J_y are identical near the time of emission, but the slope in J_z near the time of emission flips sign every half cycle, in accordance with E_z of the driving laser. This causes the S-polarized component of the attosecond pulse to flip sign every half cycle.

As illustrated in Fig. 5.22b, the introduction of a small p-polarized component (1% here) suppresses one of the two attosecond pulses emitted each cycle, since the component of the p-polarized electric field that acts normal to the plasma surface will suppress one of the surface oscillations. The result is an attosecond pulse train with periodic spacing between pulses and where all pulses within the train have the same helicity (counterclockwise). Inspection of the plasma density dynamics [Fig. 5.22(h)] shows that the introduction of a small p-polarized component to a purely s-polarized driving laser does little to the transverse currents, but is still effective at mostly suppressing one of the two attosecond pulses emitted each cycle. This means that Note that for $I_s/I_L = 0.99$ there is still some weak emission during the suppressed half cycle, which is why lower values of I_s/I_L are required to achieve near CP low order harmonics.

As I_s/I_L is decreased further to 0.5, a CP attosecond pulse train is again observed, but the helicity of the attosecond pulse train has flipped to an orientation which coincides with the reflected fundamental (clockwise). For $I_s/I_L = 0.5$, the transverse current in the y-direction is now dominated by the p-polarized component of the laser's electric field, which is evident since J_y is primarily oscillating at $1\omega_L$ rather than the $2\omega_L$ oscillations observed for higher values of I_s/I_L where the $v \times B$ force dominates J_y .

Although a full parameter scan of the phase difference between the S and P polarized

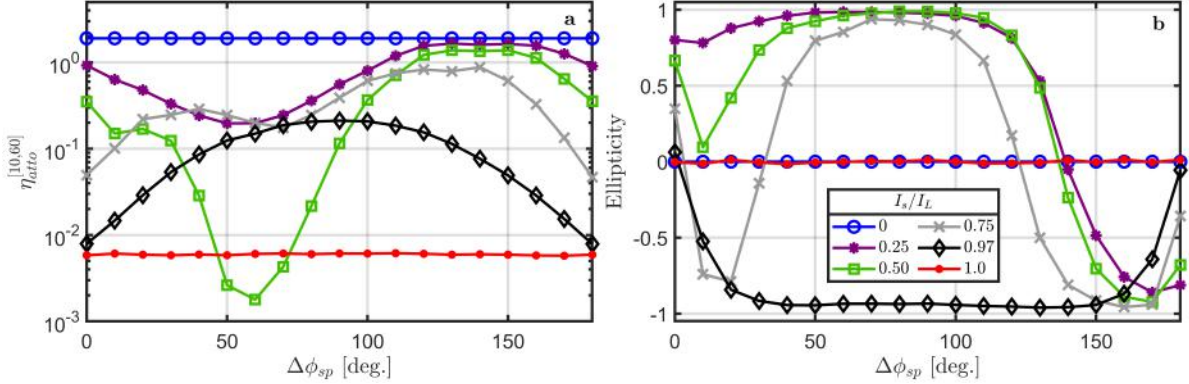


Figure 5.23: (a) Attosecond pulse efficiency and (b) attosecond pulse ellipticity in the spectral range $10 < \omega/\omega_L < 60$ as a function of the phase difference between the S and P-polarized components of the incident laser, ϕ_{sp} , for different values of I_s/I_L . Relevant simulation parameters: $a_0 = 60$, $N = 400$, $\theta = 45^\circ$, $\tau/T_L = 8$, $L = 0.05$, I_s/I_L = varied, ϕ_{sp} = varied, $\lambda_L/\Delta x = 800$, and particles/cell = 100.

components of the incident laser, ϕ_{sp} , has already been discussed in the literature [179], it is useful to return to the findings in light of the above discussion. In figure 5.23, we plot the attosecond pulse efficiency [figure 5.23(a)] and average attosecond pulse ellipticity [figure 5.23(b)] in the frequency range $10 < \omega/\omega_L < 60$ as a function of $\Delta\phi_{sp}$. In each figure, the different line types indicate the fraction of energy contained in the S-polarized component of the driving laser, I_s/I_L . Although P-polarized interactions are the most efficient for all values of $\Delta\phi_{sp}$, interactions with $I_s/I_L \lesssim 0.75$ reach comparable attosecond pulse efficiencies at an optimized value of $\Delta\phi_{sp}$. For $I_s/I_L = 0.97$, the peak efficiency occurs at $\Delta\phi_{sp} = 90^\circ$. The least efficient interactions happens for $I_s/I_L = 1.0$ for all values of $\Delta\phi_{sp}$.

At this value of a_0/N , we find that the highest ellipticity (in absolute value), occurs when $\Delta\phi_{sp} = 90^\circ$ and $I_s/I_L = 0.5$ or 0.97 . Circularly polarized attosecond pulses are also obtained for values of $I_s/I_L = 0.25$ and 0.75 when $\Delta\phi_{sp} = 90^\circ$. For purely S and P polarized interactions, the ellipticity of the attosecond pulse train is nearly zero, but for linearly polarized lasers with energy in both the S and P-polarized components, an ellipticity close to one can be obtained (see e.g. the point where $\Delta\phi_{sp} = 180^\circ$ for the line $I_s/I_L = 0.25$). This is in agreement with previous numerical results [184].

In Fig. 5.24 we plot the spectral efficiency [Fig. 5.24(a)] and attosecond pulse train ellipticity [Fig. 5.24(b)] as a function of I_s/I_L for ratios of a_0/N between 0.01 and 1.0.

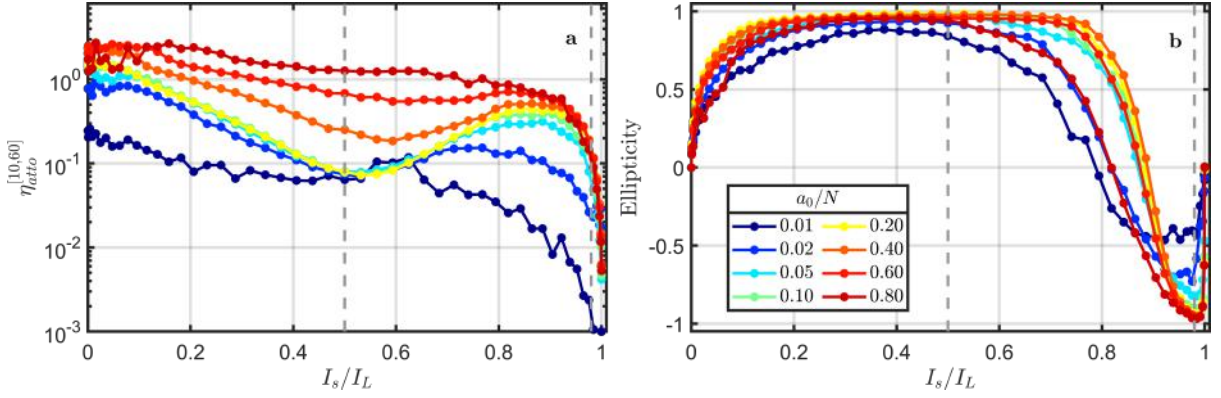


Figure 5.24: One-dimensional particle-in-cell simulations of (a) spectral efficiency and (b) ellipticity using frequencies in the range $10 < \omega/\omega_L < 60$ as a function of I_s/I_L for different values of a_0/N . The grey dashed lines are located at $I_s/I_L = 0.50$ and 0.98 . Simulation parameters: $a_0 = \text{varied}$, $N = 400$, $\theta = 45^\circ$, $\tau/T_L = 8$, $L = 0.05$, $I_s/I_L = \text{varied}$, $\phi_{sp} = \pi/2$, $\lambda_L/\Delta x = 2000$, and particles/cell = 75.

Both the attosecond pulses and spectral efficiency were constructed using frequency in the range $10 < \omega/\omega_L < 60$. Here we see that peak efficiency from CP incident lasers is comparable to the peak efficiency of P-polarized lasers, and is generally greater than that of nearly S-polarized driving lasers. Purely s-polarized driving lasers have the lowest efficiency. In addition to increased efficiency, higher laser intensities increase the degree of ellipticity [Fig. 5.24b] for both CP driving lasers and nearly S-polarized driving lasers. At $a_0/N = 0.01$, the peak ellipticity is about 0.8 for CP driving laser and about -0.55 for nearly S-polarized driving lasers. The peak ellipticity approaches 1 for CP driving lasers and -1 for nearly S-polarized driving lasers as a_0/N is increased beyond 0.40.

Although it is interesting from a theoretical point that CP attosecond pulses with opposite helicity are emitted for nearly CP driving lasers and nearly s-polarized driving lasers, respectively, it is not all that practically useful. CP driving lasers emit more efficient attosecond pulses than nearly s-polarized driving lasers and is less sensitive to the input value of I_s/I_L . If you want a CP attosecond pulse with opposite helicity, then you can just flip the helicity of the driving laser. However, this phenomena is useful if one plans to keep the fundamental driving laser after the interaction such as when constructing two-color light sources [128]. In this case, one can use this result to readily construct co- and counter-rotating two color beams, which often require complicated set-ups with several transmissive optics [36], simply by tuning the ellipticity of the driving

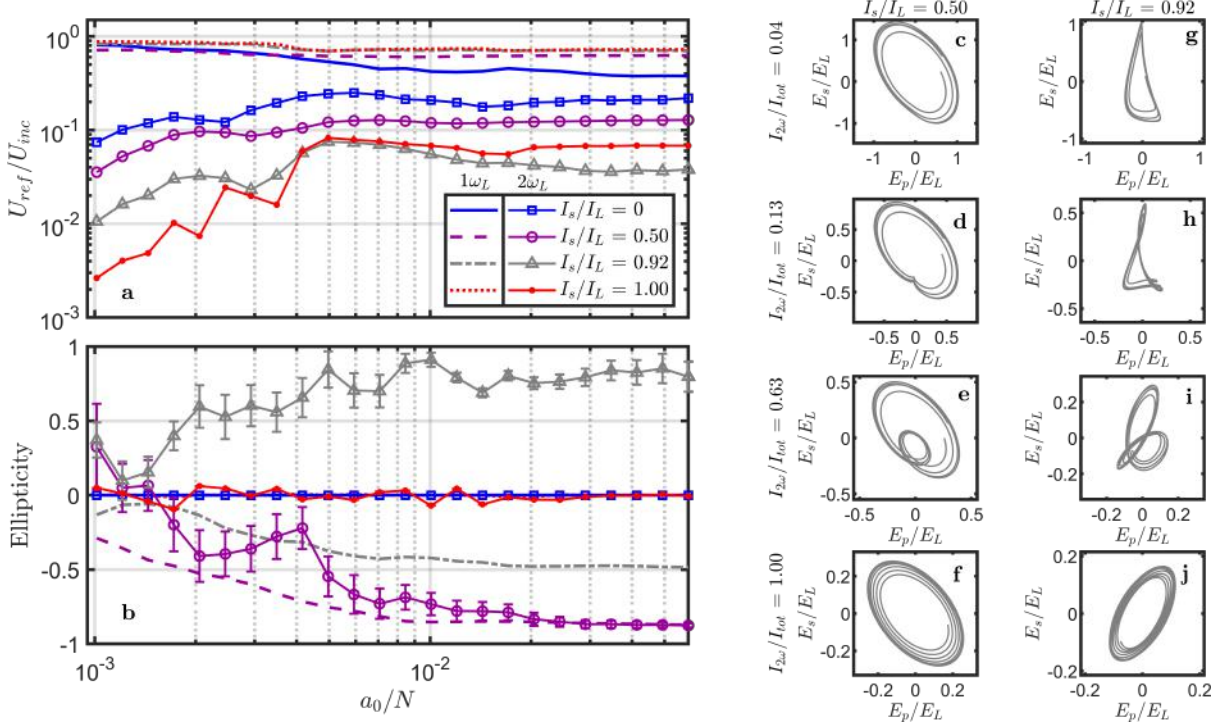


Figure 5.25: One-dimensional particle-in-cell simulations of the reflected energy (a) and ellipticity (b) contained in the fundamental (lines) and second harmonic (lines and symbols) as a function of a_0/N for different values of I_s/I_L . Panels c-j show the polarization plane projections of the reflected fundamental and second harmonics, where each column is for a different value of I_s/I_L and each row is for a different ratio of second harmonic energy to the total beam energy. Panels (b) and (e) represents the unaltered reflected two color beam and the other panels were formed by decreasing the fundamental energy, which can be accomplished with the use of a dichroic mirror. Simulation parameters: a_0 = varied, $N = 400$, $\theta = 45^\circ$, $\tau/T_L = 8$, $L = 0.05$, I_s/I_L = varied, $\phi_{sp} = \pi/2$, $\lambda_L/\Delta x = 300$, and particles/cell = 100.

laser incident on a plasma mirror.

In Fig. 5.25 we plot the reflected fundamental (lines) and second harmonic (lines with symbols) efficiency [Fig. 5.25(a)] and ellipticity [Fig. 5.25(b)] as a function of the laser intensity for different values of I_s/I_L . Importantly, we show here that at the laser intensity increases, both the ellipticity and efficiency of the reflected fundamental and second harmonic saturate to fixed values. The saturation efficiency of the second harmonic is 20% for P-polarized interactions, 11% for CP interactions, and 4% for S-polarized interactions. In Fig. 5.25(c-j), we plot the polarization plane projection of the reflected two-color laser when $a_0/N = 0.04$ and $I_s/I_L = 0.5$ [Fig. 5.25(c-f)] and $I_s/I_L = 0.90$ [Fig. 5.25(g-j)]. Each row is for a different value of the second harmonic energy

compared to the total energy in the beam, where Fig. 5.25(b) and 5.25(e) correspond to the unaltered reflected beams. The other plots are constructed by adjusting the reflected fundamental energy, which can be done in experiments with a dichroic mirror. Co- and counter-rotating bi-color lasers have been proposed for several applications including the prospect of enhanced harmonic generation from plasma mirrors as well as in gas-based and underdense plasmas [36, 189].

In summary, we showed that tuning the ellipticity of the driving laser in relativistic laser-solid interactions leads to the emission of co-rotating and counter-rotating circularly polarized harmonics, depending on whether the driving laser is nearly circularly polarized or nearly s-polarized, respectively. We find that harmonics produced with circularly polarized lasers have a higher peak efficiency and their ellipticity is less sensitive to initial conditions than harmonics produced from nearly S-polarized interactions. Finally, we propose using plasma mirrors to construct two-color, co- and counter-rotating lasers with up to 11% and 4% conversion into the second harmonic, respectively, which will be a valuable research tool for high-power nonlinear light-matter interactions.

Chapter 6

Conclusion

6.1 Summary of this thesis

In summary, this thesis has presented a series of novel experimental and numerical results pertaining to the generation of harmonics from relativistic laser–solid interactions.

In particular, in chapter 2, results from one-dimensional particle-in-cell simulations of relativistic laser-solid interactions are presented, concentrating on the sub-cycle dynamics of electron bunches and the emitted attosecond pulses modeled with and without a Monte-Carlo-based collision algorithm as a function of the laser intensity, plasma density, laser angle of incidence, and spatial and temporal resolution of the simulations. In collisionless simulations, we find the appearance of resolution-dependent, single-cell density spikes in the spatial distribution of the electron number density at times leading up to the attosecond pulse emission. In simulations with collisions, the resolution-dependent density spikes disappear. In addition, collisions increase the spread in the distribution of relativistic Lorentz factors of emitting electrons, reducing attosecond pulse intensity. Finally, we showed that the numerical dispersion present in particle-in-cell codes based on the Yee solver does not affect the temporal profiles of emitted attosecond pulses for significant propagation lengths at a spatial resolution of ten cells per the shortest harmonic wavelength under study.

Chapters 3 and 4 presented experimental results pertaining to intense light interact-

ing with plasma optics. In chapter 3, a thorough characterization of a plasma mirrors effect on the reflected spatial and temporal profiles of the incident laser was performed, showing that plasma mirrors improve the spatial quality of the laser when operating in either the sub-relativistic or relativistic regime, that plasma mirrors do not change the temporal profile of the laser on a femtosecond timescale but reduce the intensity of any pre-pulses by at least two orders of magnitude. In chapter 4, it was experimentally demonstrated that plasma mirrors driven with a phase-controlled two-color driving laser (made of co-propagating 800nm light and its second harmonic) emit enhanced third and fourth harmonic energy compared to plasma mirrors driven with with 800nm light alone. The two-color laser itself was synthesized with harmonic generation from a plasma mirror, providing the first demonstration of waveform-controlled engineering using a multi-pass plasma mirror configuration. The relative phase between the two colors at the target surface is adjusted either by having the two colors propagate through a dispersive element or by varying the position of the target with respect to the two-color laser's focus.

Finally, chapter 5 presented a number of numerical results from particle-in-cell simulations, focusing on the effects of changing the polarization state of the driving laser on the radiated harmonics. For normal incidence circularly polarized interactions with ultra thin foils, it was demonstrated that vortex harmonics are emitted in both the reflected and transmitted direction. For more general elliptically polarized lasers, it was shown that plasma mirrors emit circularly polarized harmonics that either co-rotate or counter-rotate with the reflected fundamental, depending on if the driving laser is nearly circularly polarized or nearly s-polarized, respectively. The change in helicity is explained by the different behavior of the transverse electron density current in the plane of incidence, which is primarily driven by the $q\vec{v} \times \vec{B}$ force for s-polarized interactions or by the p-polarized component of the laser's electric field for circularly polarized interactions. Finally, it was proposed that using plasma mirrors to generate two-color co- and counter-rotating high-power lasers with up to 11% and 4% conversion efficiencies, respectively, into the second harmonic.

6.2 Future work

In chapter 4, we experimentally demonstrated the application of using plasma mirrors for synthesizing multi-color waveforms and then used this multi-color waveform to realize enhanced harmonic efficiency in a subsequent interaction. Then in Chapter 5, we showed that plasma mirrors can be used to synthesise two color co- and counter-rotating waveforms by using elliptically polarized driving lasers. With slight modifications to the experimental set-up of chapter 4, we can implement a study of harmonic generation from plasma mirrors driven by an ellipticity-controlled laser. In figure 6.1, we show the experimental setup which includes a quarter waveplate after PM1. Rotating the quarter waveplate about the laser's polarization axis can tune the laser's polarization from linear to circular polarization. After interaction with a plasma mirror, the harmonics can be collected and sent through a polarizing beam splitter (e.g. here a Wollaston prism). Although the energy of harmonics driven by s, p, and circularly polarized lasers have been performed, a complete measurement of the harmonics polarization state under these conditions is still missing. Potential applications of these harmonics include probing the spin-resolved features in magnetic materials and molecular chirality on a sub-femtosecond timescale.

As shown in chapter 5, plasma mirrors driven by elliptically polarized lasers can synthesize two-color circularly polarized lasers, where the second harmonic either co-rotates with the reflected fundamental or counter-rotates with the reflected fundamental. Following the success of chapter 4, a multi-pass plasma mirror configuration is proposed for first generating two-color circularly polarized lasers and then using this two-color laser to further drive harmonic radiation from a secondary plasma mirror, providing additional degrees of freedom to control the relativistic plasma dynamics. A polarization-controlled is just one additional source of structure a plasma mirror can impart on the radiated harmonics. In principle, the experimental set-up can also be modified to include studies of spatial structure by using high-order transverse modes for harmonic generation (e.g. Laguerre-Gauss, Hermite-Gauss, or Bessel beams).

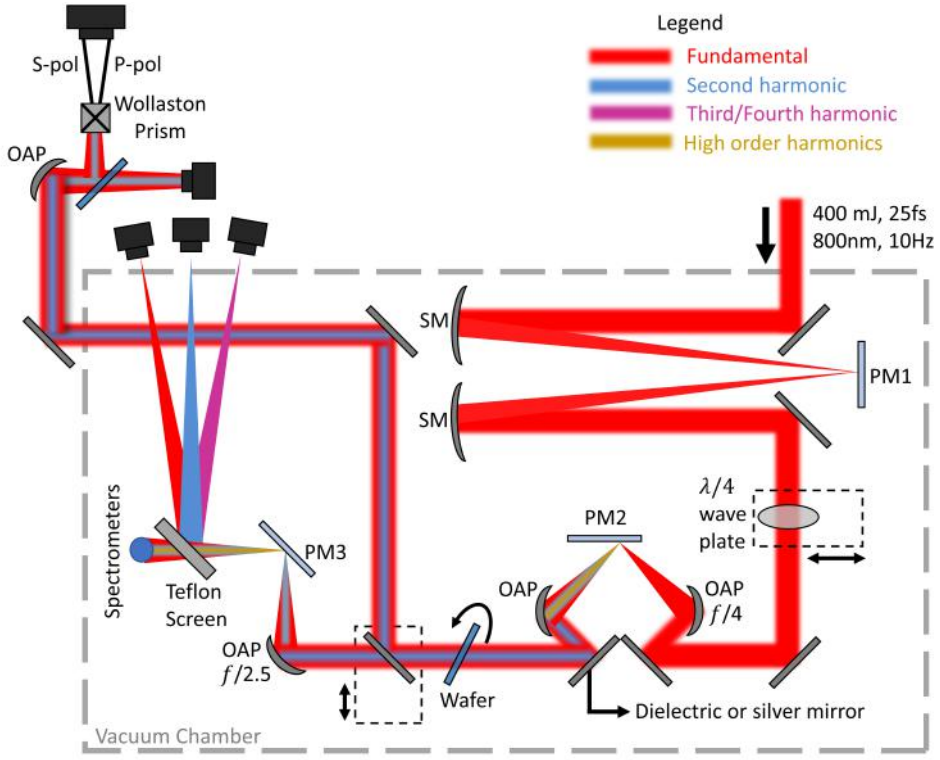


Figure 6.1: Proposed changes to the experimental set-up of the multi-pass plasma mirror configuration to include elliptically polarized driving lasers, showing the interaction geometries for all three plasma mirrors as well as the diagnostics for measuring the energy and polarization state of the reflected harmonics. The laser beam (800nm, 10Hz, 25fs, 400mJ) enters the experimental vacuum chamber from the upper right and interacts with three plasma mirrors: one contrast-cleaning plasma mirror (PM1), a relativistically-drive plasma mirror used to synthesize a two-color waveform (PM2), and a relativistically-driven plasma mirror used for studying harmonic generation with the two-color laser (PM3). After PM1, the beam passes through a quarter wave plate which will convert the p-polarized light to elliptically polarized light or circular polarized light, depending on the orientation of the quarter waveplate. A Wollaston prism in conjunction with bandpass filters will be used to characterize the polarization state of individual harmonic orders. A mirror that sits on a translation stage can pick off the laser after the PM2 interaction which allows for near-field and far-field characterization of the two-color laser. A 100 μ m thick fused silica wafer is placed between PM2 and PM3, where the rotation of the wafer allows for controlling the relative phase between the two colors. After the interaction from PM3, visible and ultraviolet CCDs image the harmonics from a Teflon screen, and a visible spectrometer measures the spectrum. Key: PM = Plasma Mirror. SM = Spherical Mirror. OAP = off axis parabola.

Bibliography

- ¹C. Danson, D. Hillier, N. Hopps, and D. Neely, “Petawatt class lasers worldwide”, High Power Laser Science and Engineering **3**, e3 (2015).
- ²D. Strickland and G. Mourou, “Compression of amplified chirped optical pulses”, Optics Communications **55**, 447–449 (1985).
- ³H. Milchberg, “Indestructible plasma optics”, Physics Today **72**, 70–71 (2019).
- ⁴J. M. Mikhailova, A. Buck, A. Borot, K. Schmid, C. Sears, G. D. Tsakiris, F. Krausz, and L. Veisz, “Ultra-high-contrast few-cycle pulses for multipetawatt-class laser technology”, Optics Letters **36**, 3145–3147 (2011).
- ⁵H. C. Kapteyn, M. M. Murnane, A. Szoke, and R. W. Falcone, “Prepulse energy suppression for high-energy ultrashort pulses using self-induced plasma shuttering”, Optics letters **16**, 490–492 (1991).
- ⁶P. Michel, L. Divol, D. Turnbull, and J. D. Moody, “Dynamic Control of the Polarization of Intense Laser Beams via Optical Wave Mixing in Plasmas”, Physical Review Letters **113**, 205001 (2014).
- ⁷K. Qu, Q. Jia, and N. J. Fisch, “Plasma q -plate for generation and manipulation of intense optical vortices”, Physical Review E **96**, 053207 (2017).
- ⁸V. M. Malkin, G. Shvets, and N. J. Fisch, “Fast Compression of Laser Beams to Highly Overcritical Powers”, Physical Review Letters **82**, 4448–4451 (1999).
- ⁹M. R. Edwards, V. R. Munirov, A. Singh, N. M. Fasano, E. Kur, N. Lemos, J. M. Mikhailova, J. S. Wurtele, and P. Michel, “Holographic Plasma Lenses”, Physical Review Letters **128**, 065003 (2022).
- ¹⁰L. Shi, W. Li, Y. Wang, X. Lu, L. Ding, and H. Zeng, “Generation of High-Density Electrons Based on Plasma Grating Induced Bragg Diffraction in Air”, Physical Review Letters **107**, 095004 (2011).
- ¹¹S. Suntsov, D. Abdollahpour, D. G. Papazoglou, and S. Tzortzakis, “Femtosecond laser induced plasma diffraction gratings in air as photonic devices for high intensity laser applications”, Applied Physics Letters **94**, 251104 (2009).
- ¹²M. R. Edwards and P. Michel, “Plasma Transmission Gratings for Compression of High-Intensity Laser Pulses”, Physical Review Applied **18**, 024026 (2022).
- ¹³D. Turnbull, C. Goyon, G. E. Kemp, B. B. Pollock, D. Mariscal, L. Divol, J. S. Ross, S. Patankar, J. D. Moody, and P. Michel, “Refractive Index Seen by a Probe Beam Interacting with a Laser-Plasma System”, Physical Review Letters **118**, 015001 (2017).
- ¹⁴G. Lehmann and K. H. Spatschek, “Plasma-based polarizer and waveplate at large laser intensity”, Physical Review E **97**, 063201 (2018).

- ¹⁵J. Ren, W. Cheng, S. Li, and S. Suckewer, “A new method for generating ultraintense and ultrashort laser pulses”, *Nature Physics* **3**, 732–736 (2007).
- ¹⁶A. A. Andreev, C. Riconda, V. T. Tikhonchuk, and S. Weber, “Short light pulse amplification and compression by stimulated Brillouin scattering in plasmas in the strong coupling regime”, *Physics of Plasmas* **13**, 053110 (2006).
- ¹⁷M. R. Edwards, Q. Jia, J. M. Mikhailova, and N. J. Fisch, “Short-pulse amplification by strongly coupled stimulated Brillouin scattering”, *Physics of Plasmas* **23**, 083122 (2016).
- ¹⁸J.-R. Marquès, L. Lancia, T. Gangolf, M. Blecher, S. Bolaños, J. Fuchs, O. Willi, F. Amiranoff, R. L. Berger, M. Chiaramello, S. Weber, and C. Riconda, “Joule-Level High-Efficiency Energy Transfer to Subpicosecond Laser Pulses by a Plasma-Based Amplifier”, *Physical Review X* **9**, 021008 (2019).
- ¹⁹H.-E. Tsai, A. V. Arefiev, J. M. Shaw, D. J. Stark, X. Wang, R. Zgadzaj, and M. C. Downer, “Self-aligning concave relativistic plasma mirror with adjustable focus”, *Physics of Plasmas* **24**, 013106 (2017).
- ²⁰D. Kumar, M. Šmíd, S. Singh, A. Soloviev, H. Bohlin, K. Burdonov, G. Fente, A. Kotov, L. Lancia, V. Lédl, S. Makarov, M. Morrissey, S. Perevalov, D. Romanovsky, S. Pikuz, R. Kodama, D. Neely, P. McKenna, T. Laštovička, M. Starodubtsev, S. Weber, M. Nakatsutsumi, and J. Fuchs, “Alignment of solid targets under extreme tight focus conditions generated by an ellipsoidal plasma mirror”, *Matter and Radiation at Extremes* **4**, 024402 (2019).
- ²¹R. Wilson, M. King, R. J. Gray, D. C. Carroll, R. J. Dance, C. Armstrong, S. J. Hawkes, R. J. Clarke, D. J. Robertson, D. Neely, and P. McKenna, “Ellipsoidal plasma mirror focusing of high power laser pulses to ultra-high intensities”, *Physics of Plasmas* **23**, 033106 (2016).
- ²²C. Thaury, F. Quéré, J.-P. Geindre, A. Levy, T. Ceccotti, P. Monot, M. Bougeard, F. Réau, P. d’Oliveira, P. Audebert, R. Marjoribanks, and P. Martin, “Plasma mirrors for ultrahigh-intensity optics”, *Nature Physics* **3**, 424–429 (2007).
- ²³G. Doumy, F. Quéré, O. Gobert, M. Perdrix, P. Martin, P. Audebert, J. C. Gauthier, J.-P. Geindre, and T. Wittmann, “Complete characterization of a plasma mirror for the production of high-contrast ultraintense laser pulses”, *Physical Review E* **69**, 026402 (2004).
- ²⁴A. Lévy, T. Ceccotti, P. D’Oliveira, F. Réau, M. Perdrix, F. Quéré, P. Monot, M. Bougeard, H. Lagadec, P. Martin, J.-P. Geindre, and P. Audebert, “Double plasma mirror for ultrahigh temporal contrast ultraintense laser pulses”, *Optics Letters* **32**, 310–312 (2007).
- ²⁵A. Macchi, M. Borghesi, and M. Passoni, “Ion acceleration by superintense laser-plasma interaction”, *Reviews of Modern Physics* **85**, 751–793 (2013).
- ²⁶C. Thaury and F. Quéré, “High-order harmonic and attosecond pulse generation on plasma mirrors: basic mechanisms”, *Journal of Physics B: Atomic, Molecular and Optical Physics* **43** (2010).
- ²⁷M. R. Edwards and J. M. Mikhailova, “The X-Ray Emission Effectiveness of Plasma Mirrors: Reexamining Power-Law Scaling for Relativistic High-Order Harmonic Generation”, *Scientific Reports* **10**, 1–20 (2020).

- ²⁸N. H. Burnett, H. A. Baldis, M. C. Richardson, and G. D. Enright, “Harmonic generation in CO₂ laser target interaction”, *Applied Physics Letters* **31**, 172–174 (1977).
- ²⁹R. L. Carman, C. K. Rhodes, and R. F. Benjamin, “Observation of harmonics in the visible and ultraviolet created in co₂-laser-produced plasmas”, *Physical Review A* **24**, 2649–2663 (1981).
- ³⁰R. L. Carman, D. W. Forslund, and J. M. Kindel, “Visible harmonic emission as a way of measuring profile steepening”, *Physical Review Letters* **46** (1981).
- ³¹B. Bezzerides, R. D. Jones, and D. W. Forslund, “Plasma Mechanism for Ultraviolet Harmonic Radiation Due to Intense CO₂ Light”, *Physical Review Letters* **49**, 202–205 (1982).
- ³²T. Brabec and F. Krausz, “Intense few-cycle laser fields: Frontiers of nonlinear optics”, *Reviews of Modern Physics* **72**, 545–591 (2000).
- ³³F. Krausz and M. Ivanov, “Attosecond physics”, *Reviews of Modern Physics* **81**, 163–234 (2009).
- ³⁴M. Hentschel, R. Kienberger, C. Spielmann, G. A. Reider, N. Milosevic, T. Brabec, P. Corkum, U. Heinzmann, M. Drescher, and F. Krausz, “Attosecond metrology”, *Nature* **414**, 509–513 (2001).
- ³⁵J. Li, X. Ren, Y. Yin, K. Zhao, A. Chew, Y. Cheng, E. Cunningham, Y. Wang, S. Hu, Y. Wu, M. Chini, and Z. Chang, “53-attosecond X-ray pulses reach the carbon K-edge”, *Nature Communications* **8**, 186 (2017).
- ³⁶A. Fleischer, O. Kfir, T. Diskin, P. Sidorenko, and O. Cohen, “Spin angular momentum and tunable polarization in high-harmonic generation”, *Nature Photonics* **8**, 543–549 (2014).
- ³⁷K. M. Dorney, L. Rego, N. J. Brooks, J. San Román, C.-T. Liao, J. L. Ellis, D. Zusin, C. Gentry, Q. L. Nguyen, J. M. Shaw, A. Picón, L. Plaja, H. C. Kapteyn, M. M. Murnane, and C. Hernández-García, “Controlling the polarization and vortex charge of attosecond high-harmonic beams via simultaneous spin-orbit momentum conservation”, *Nature Photonics* **13**, 123–130 (2019).
- ³⁸P. Gibbon, “Harmonic Generation by Femtosecond Laser-Solid Interaction: A Coherent “Water-Window” Light Source?”, *Physical Review Letters* **76**, 50–53 (1996).
- ³⁹F. Quéré, C. Thaury, P. Monot, S. Dobosz, P. Martin, J.-P. Geindre, and P. Audebert, “Coherent Wake Emission of High-Order Harmonics from Overdense Plasmas”, *Physical Review Letters* **96**, 125004 (2006).
- ⁴⁰F. Quéré, C. Thaury, J.-P. Geindre, G. Bonnaud, P. Monot, and P. Martin, “Phase Properties of Laser High-Order Harmonics Generated on Plasma Mirrors”, *Physical Review Letters* **100**, 095004 (2008).
- ⁴¹S. Kahaly, S. Monchocé, H. Vincenti, T. Dzelzainis, B. Dromey, M. Zepf, P. Martin, and F. Quéré, “Direct Observation of Density-Gradient Effects in Harmonic Generation from Plasma Mirrors”, *Physical Review Letters* **110**, 175001 (2013).
- ⁴²L. Plaja, L. Roso, K. Rzazewski, and M. Lewenstein, “Generation of attosecond pulse trains during the reflection of a very intense laser on a solid surface”, *JOSA B* **15**, 1904–1911 (1998).

- ⁴³S. V. Bulanov, N. M. Naumova, and F. Pegoraro, “Interaction of an ultrashort, relativistically strong laser pulse with an overdense plasma”, Physics of Plasmas **1**, 745–757 (1994).
- ⁴⁴R. Lichters, J. Meyer-ter-Vehn, and A. Pukhov, “Short-pulse laser harmonics from oscillating plasma surfaces driven at relativistic intensity”, Physics of Plasmas **3**, 3425–3437 (1996).
- ⁴⁵T. Baeva, S. Gordienko, and A. Pukhov, “Theory of high-order harmonic generation in relativistic laser interaction with overdense plasma”, Physical Review E **74**, 046404 (2006).
- ⁴⁶T. J. M. Boyd and R. Ondarza-Rovira, “Anomalies in Universal Intensity Scaling in Ultrarelativistic Laser-Plasma Interactions”, Physical Review Letters **101**, 125004 (2008).
- ⁴⁷D. an der Brügge and A. Pukhov, “Enhanced relativistic harmonics by electron nanobunching”, Physics of Plasmas **17**, 033110 (2010).
- ⁴⁸A. A. Gonoskov, A. V. Korzhimanov, A. V. Kim, M. Marklund, and A. M. Sergeev, “Ultrarelativistic nanoplasmonics as a route towards extreme-intensity attosecond pulses”, Physical Review E **84**, 046403 (2011).
- ⁴⁹J. M. Mikhailova, M. V. Fedorov, N. Karpowicz, P. Gibbon, V. T. Platonenko, A. M. Zheltikov, and F. Krausz, “Isolated Attosecond Pulses from Laser-Driven Synchrotron Radiation”, Physical Review Letters **109**, 245005 (2012).
- ⁵⁰B. Dromey, M. Zepf, A. Gopal, K. Lancaster, M. Wei, K. Krushelnick, M. Tatarakis, N. Vakakis, S. Moustaisis, R. Kodama, et al., “High harmonic generation in the relativistic limit”, Nature physics **2**, 456–459 (2006).
- ⁵¹B. Dromey, S. Kar, C. Bellei, D. C. Carroll, R. J. Clarke, J. S. Green, S. Kneip, K. Markey, S. R. Nagel, P. T. Simpson, L. Willingale, P. McKenna, D. Neely, Z. Najmudin, K. Krushelnick, P. A. Norreys, and M. Zepf, “Bright Multi-keV Harmonic Generation from Relativistically Oscillating Plasma Surfaces”, Physical Review Letters **99**, 085001 (2007).
- ⁵²B. Dromey, D. Adams, R. Hörlein, Y. Nomura, S. G. Rykovanov, D. C. Carroll, P. S. Foster, S. Kar, K. Markey, P. McKenna, D. Neely, M. Geissler, G. D. Tsakiris, and M. Zepf, “Diffraction-limited performance and focusing of high harmonics from relativistic plasmas”, Nature Physics **5**, 146–152 (2009).
- ⁵³C. Rödel, D. an der Brügge, J. Bierbach, M. Yeung, T. Hahn, B. Dromey, S. Herzer, S. Fuchs, A. G. Pour, E. Eckner, et al., “Harmonic generation from relativistic plasma surfaces in ultrasteep plasma density gradients”, Physical review letters **109**, 125002 (2012).
- ⁵⁴P. Heissler, A. Barna, J. M. Mikhailova, G. Ma, K. Khrennikov, S. Karsch, L. Veisz, I. Földes, and G. D. Tsakiris, “Multi- μ J harmonic emission energy from laser-driven plasma”, Applied Physics B **118**, 195–201 (2015).
- ⁵⁵H. Vincenti, S. Monchocé, S. Kahaly, G. Bonnaud, P. Martin, and F. Quéré, “Optical properties of relativistic plasma mirrors”, Nature Communications **5**, 3403 (2014).

- ⁵⁶O. Jahn, V. E. Leshchenko, P. Tzallas, A. Kessel, M. Krüger, A. Münzer, S. A. Trushin, G. D. Tsakiris, S. Kahaly, D. Kormin, L. Veisz, V. Pervak, F. Krausz, Z. Major, and S. Karsch, “Towards intense isolated attosecond pulses from relativistic surface high harmonics”, *Optica* **6**, 280–287 (2019).
- ⁵⁷F. Dollar, P. Cummings, V. Chvykov, L. Willingale, M. Vargas, V. Yanovsky, C. Zulick, A. Maksimchuk, A. Thomas, and K. Krushelnick, “Scaling high-order harmonic generation from laser-solid interactions to ultrahigh intensity”, *Physical review letters* **110**, 175002 (2013).
- ⁵⁸B. Dromey, S. Rykovanov, M. Yeung, R. Hörlein, D. Jung, D. C. Gautier, T. Dzelzainis, D. Kiefer, S. Palaniyppan, R. Shah, J. Schreiber, H. Ruhl, J. C. Fernandez, C. L. S. Lewis, M. Zepf, and B. M. Hegelich, “Coherent synchrotron emission from electron nanobunches formed in relativistic laser–plasma interactions”, *Nature Physics* **8**, 804–808 (2012).
- ⁵⁹B. Dromey, S. Cousens, S. Rykovanov, M. Yeung, D. Jung, D. C. Gautier, T. Dzelzainis, D. Kiefer, S. Palaniyppan, R. Shah, J. Schreiber, J. C. Fernandez, C. L. S. Lewis, M. Zepf, and B. M. Hegelich, “Coherent synchrotron emission in transmission from ultrathin relativistic laser plasmas”, *New Journal of Physics* **15**, 015025 (2013).
- ⁶⁰M. Yeung, S. Rykovanov, J. Bierbach, L. Li, E. Eckner, S. Kuschel, A. Woldegeorgis, C. Rödel, A. Sävert, G. G. Paulus, M. Coughlan, B. Dromey, and M. Zepf, “Experimental observation of attosecond control over relativistic electron bunches with two-colour fields”, *Nature Photonics* **11**, 32–35 (2017).
- ⁶¹L. Chopineau, G. Blaclar, A. Denoeud, H. Vincenti, F. Quéré, and S. Haessler, “Sub-laser-cycle control of relativistic plasma mirrors”, *Physical Review Research* **4**, L012030 (2022).
- ⁶²M. Yeung, J. Bierbach, E. Eckner, S. Rykovanov, S. Kuschel, A. Sävert, M. Förster, C. Rödel, G. G. Paulus, S. Cousens, M. Coughlan, B. Dromey, and M. Zepf, “Noncollinear Polarization Gating of Attosecond Pulse Trains in the Relativistic Regime”, *Physical Review Letters* **115**, 193903 (2015).
- ⁶³A. Leblanc, A. Denoeud, L. Chopineau, G. Mennerat, P. Martin, and F. Quéré, “Plasma holograms for ultrahigh-intensity optics”, *Nature Physics* **13**, 440–443 (2017).
- ⁶⁴A. Denoeud, L. Chopineau, A. Leblanc, and F. Quéré, “Interaction of Ultraintense Laser Vortices with Plasma Mirrors”, *Physical Review Letters* **118**, 033902 (2017).
- ⁶⁵E. S. Sarachik and G. T. Schappert, “Classical theory of the scattering of intense laser radiation by free electrons”, *Physical Review D* **1**, 2738–2753 (1970).
- ⁶⁶J. N. Bardsley, B. M. Penetrante, and M. H. Mittleman, “Relativistic dynamics of electrons in intense laser fields”, *Physical Review A* **40**, 3823–3835 (1989).
- ⁶⁷P. Gibbon, *Short pulse laser interactions with matter: an introduction* (Sept. 5, 2005), 327 pp.
- ⁶⁸P. M. Woodward, “A method of calculating the field over a plane aperture required to produce a given polar diagram”, *Journal of the Institution of Electrical Engineers - Part IIIA: Radiolocation* **93**, 1554–1558 (1946).
- ⁶⁹J. D. Lawson, “Lasers and Accelerators”, *IEEE Transactions on Nuclear Science* **26**, 4217–4219 (1979).

- ⁷⁰G. Lehmann, “Efficient Semi-Lagrangian Vlasov-Maxwell Simulations of High Order Harmonic Generation from Relativistic Laser-Plasma Interactions”, Communications in Computational Physics **20**, 583–602 (2016).
- ⁷¹J. Dawson, “One-Dimensional Plasma Model”, The Physics of Fluids **5**, 445–459 (1962).
- ⁷²J. M. Dawson, “Particle simulation of plasmas”, Reviews of Modern Physics **55**, 403–447 (1983).
- ⁷³C. Birdsall, “Particle-in-cell charged-particle simulations, plus Monte Carlo collisions with neutral atoms, PIC-MCC”, IEEE Transactions on Plasma Science **19**, 65–85 (1991).
- ⁷⁴T. D. Arber, K. Bennett, C. S. Brady, A. Lawrence-Douglas, M. G. Ramsay, N. J. Sircombe, P. Gillies, R. G. Evans, H. Schmitz, A. R. Bell, and C. P. Ridgers, “Contemporary particle-in-cell approach to laser-plasma modelling”, Plasma Physics and Controlled Fusion **57**, 113001 (2015).
- ⁷⁵Kane Yee, “Numerical solution of initial boundary value problems involving maxwell’s equations in isotropic media”, IEEE Transactions on Antennas and Propagation **14**, 302–307 (1966).
- ⁷⁶R. W. Hockney and J. W. Eastwood, *Computer Simulation Using Particles* (1988).
- ⁷⁷A. Pukhov, “Three-dimensional electromagnetic relativistic particle-in-cell code VLPL (Virtual Laser Plasma Lab)”, Journal of Plasma Physics **61**, 425–433 (1999).
- ⁷⁸C. K. Birdsall and A. B. Langdon, *Plasma Physics via Computer Simulation* (2004).
- ⁷⁹A. Pukhov, “X-dispersionless Maxwell solver for plasma-based particle acceleration”, Journal of Computational Physics **418**, 109622 (2020).
- ⁸⁰A. Blinne, D. Schinkel, S. Kuschel, N. Elkina, S. G. Rykov, and M. Zepf, “A systematic approach to numerical dispersion in Maxwell solvers”, Computer Physics Communications **224**, 273–281 (2018).
- ⁸¹F. Li, P. Yu, X. Xu, F. Fiuzza, V. K. Decyk, T. Dalichaouch, A. Davidson, A. Tableman, W. An, F. S. Tsung, R. A. Fonseca, W. Lu, and W. B. Mori, “Controlling the numerical Cerenkov instability in PIC simulations using a customized finite difference Maxwell solver and a local FFT based current correction”, Computer Physics Communications **214**, 6–17 (2017).
- ⁸²B. B. Godfrey and J.-L. Vay, “Suppressing the numerical Cherenkov instability in FDTD PIC codes”, Journal of Computational Physics **267**, 1–6 (2014).
- ⁸³X. Xu, P. Yu, S. F. Martins, F. S. Tsung, V. K. Decyk, J. Vieira, R. A. Fonseca, W. Lu, L. O. Silva, and W. B. Mori, “Numerical instability due to relativistic plasma drift in EM-PIC simulations”, Computer Physics Communications **184**, 2503–2514 (2013).
- ⁸⁴B. M. Cowan, D. L. Bruhwiler, J. R. Cary, E. Cormier-Michel, and C. G. R. Geddes, “Generalized algorithm for control of numerical dispersion in explicit time-domain electromagnetic simulations”, Physical Review Special Topics - Accelerators and Beams **16**, 041303 (2013).
- ⁸⁵R. Lehe, A. Lifschitz, C. Thaury, V. Malka, and X. Davoine, “Numerical growth of emittance in simulations of laser-wakefield acceleration”, Physical Review Special Topics - Accelerators and Beams **16**, 021301 (2013).

- ⁸⁶J. B. Cole, “High-accuracy Yee algorithm based on nonstandard finite differences: new developments and verifications”, *IEEE Transactions on Antennas and Propagation* **50**, 1185–1191 (2002).
- ⁸⁷B. B. Godfrey, “Numerical Cherenkov instabilities in electromagnetic particle codes”, *Journal of Computational Physics* **15**, 504–521 (1974).
- ⁸⁸J.-L. Vay, I. Haber, and B. B. Godfrey, “A domain decomposition method for pseudo-spectral electromagnetic simulations of plasmas”, *Journal of Computational Physics* **243**, 260–268 (2013).
- ⁸⁹H. Vincenti and J.-L. Vay, “Detailed analysis of the effects of stencil spatial variations with arbitrary high-order finite-difference Maxwell solver”, *Computer Physics Communications* **200**, 147–167 (2016).
- ⁹⁰G. Blachard, H. Vincenti, R. Lehe, and J. L. Vay, “Pseudospectral Maxwell solvers for an accurate modeling of Doppler harmonic generation on plasma mirrors with particle-in-cell codes”, *Physical Review E* **96**, 033305 (2017).
- ⁹¹H. Vincenti and J.-L. Vay, “Ultrahigh-order Maxwell solver with extreme scalability for electromagnetic PIC simulations of plasmas”, *Computer Physics Communications* **228**, 22–29 (2018).
- ⁹²H. Kallala, J.-L. Vay, and H. Vincenti, “A generalized massively parallel ultra-high order FFT-based Maxwell solver”, *Computer Physics Communications* **244**, 25–34 (2019).
- ⁹³H. Vincenti, “Achieving Extreme Light Intensities using Optically Curved Relativistic Plasma Mirrors”, *Physical Review Letters* **123**, 105001 (2019).
- ⁹⁴T. Takizuka and H. Abe, “A binary collision model for plasma simulation with a particle code”, *Journal of Computational Physics* **25**, 205–219 (1977).
- ⁹⁵K. Nanbu, “Theory of cumulative small-angle collisions in plasmas”, *Physical Review E* **55**, 4642–4652 (1997).
- ⁹⁶K. Nanbu and S. Yonemura, “Weighted Particles in Coulomb Collision Simulations Based on the Theory of a Cumulative Scattering Angle”, *Journal of Computational Physics* **145**, 639–654 (1998).
- ⁹⁷Y. Sentoku and A. J. Kemp, “Numerical methods for particle simulations at extreme densities and temperatures: Weighted particles, relativistic collisions and reduced currents”, *Journal of Computational Physics* **227**, 6846–6861 (2008).
- ⁹⁸F. Pérez, L. Gremillet, A. Decoster, M. Drouin, and E. Lefebvre, “Improved modeling of relativistic collisions and collisional ionization in particle-in-cell codes”, *Physics of Plasmas* **19**, 083104 (2012).
- ⁹⁹D. P. Higginson, I. Holod, and A. Link, “A corrected method for Coulomb scattering in arbitrarily weighted particle-in-cell plasma simulations”, *Journal of Computational Physics* **413**, 109450 (2020).
- ¹⁰⁰E. P. Alves, W. B. Mori, and F. Fiúza, “Numerical heating in particle-in-cell simulations with monte carlo binary collisions”, *Physical Review E* **103**, 013306 (2021).
- ¹⁰¹Y. M. Mikhailova, V. T. Platonenko, and A. B. Savel’ev, “Efficient heating of near-surface plasmas with femtosecond laser pulses stimulated by nanoscale inhomogeneities”, *Quantum Electronics* **35**, 38 (2005).

- ¹⁰²Y. Zhao, R. Lehe, A. Myers, M. Thévenet, A. Huebl, C. B. Schroeder, and J.-L. Vay, “Modeling of emittance growth due to Coulomb collisions in plasma-based accelerators”, *Physics of Plasmas* **27**, 113105 (2020).
- ¹⁰³S. Weber, G. Bonnaud, and J.-C. Gauthier, “Role of collisions in particle-in-cell modeling of high-density short-pulse laser-plasma interaction”, *Physics of Plasmas* **8**, 387–390 (2001).
- ¹⁰⁴D. Von der Linde and K. Rzazewski, “High-order optical harmonic generation from solid surfaces”, *Applied Physics B* **63**, 499–506 (1996).
- ¹⁰⁵P. Norreys, M. Zepf, S. Moustaisis, A. Fews, J. Zhang, P. Lee, M. Bakarezos, C. Danson, A. Dyson, P. Gibbon, et al., “Efficient extreme uv harmonics generated from picosecond laser pulse interactions with solid targets”, *Physical Review Letters* **76**, 1832 (1996).
- ¹⁰⁶S. Gordienko, A. Pukhov, O. Shorokhov, and T. Baeva, “Relativistic doppler effect: universal spectra and zeptosecond pulses”, *Physical review letters* **93**, 115002 (2004).
- ¹⁰⁷P. Heissler, P. Tzallas, J. M. Mikhailova, K. Khrennikov, L. Waldecker, F. Krausz, S. Karsch, D. Charalambidis, and G. D. Tsakiris, “Two-photon above-threshold ionization using extreme-ultraviolet harmonic emission from relativistic laser–plasma interaction”, *New Journal of Physics* **14**, 043025 (2012).
- ¹⁰⁸D. an der Brügge and A. Pukhov, “Enhanced relativistic harmonics by electron nanobunching”, *Physics of Plasmas* **17**, 033110 (2010).
- ¹⁰⁹M. Cherednychek and A. Pukhov, “Analytical approach to high harmonics spectrum in the nanobunching regime”, *Physics of Plasmas* **23**, 103301 (2016).
- ¹¹⁰S. Cousens, B. Reville, B. Dromey, and M. Zepf, “Temporal Structure of Attosecond Pulses from Laser-Driven Coherent Synchrotron Emission”, *Physical Review Letters* **116**, 083901 (2016).
- ¹¹¹A. Gonoskov, “Theory of relativistic radiation reflection from plasmas”, *Physics of Plasmas* **25**, 013108 (2018).
- ¹¹²M. R. Edwards, N. M. Fasano, and J. M. Mikhailova, “Electron-Nanobunch-Width-Dominated Spectral Power Law for Relativistic Harmonic Generation from Ultrathin Foils”, *Physical Review Letters* **124**, 185004 (2020).
- ¹¹³M. R. Edwards, V. T. Platonenko, and J. M. Mikhailova, “Enhanced attosecond bursts of relativistic high-order harmonics driven by two-color fields”, *Optics Letters* **39**, 6823 (2014).
- ¹¹⁴P. Zhang and A. G. R. Thomas, “Enhancement of high-order harmonic generation in intense laser interactions with solid density plasma by multiple reflections and harmonic amplification”, *Applied Physics Letters* **106**, 131102 (2015).
- ¹¹⁵M. R. Edwards and J. M. Mikhailova, “Multipass relativistic high-order-harmonic generation for intense attosecond pulses”, *Physical Review A* **93**, 023836 (2016).
- ¹¹⁶M. R. Edwards and J. M. Mikhailova, “Waveform-Controlled Relativistic High-Order-Harmonic Generation”, *Physical Review Letters* **117**, 125001 (2016).
- ¹¹⁷A. Bourdier, “Oblique incidence of a strong electromagnetic wave on a cold inhomogeneous electron plasma. Relativistic effects”, *The Physics of Fluids* **26**, 1804–1807 (1983).

- ¹¹⁸P. Gibbon, A. Andreev, E. Lefebvre, G. Bonnaud, H. Ruhl, J. Delettrez, and A. R. Bell, “Calibration of one-dimensional boosted kinetic codes for modeling high-intensity laser–solid interactions”, Physics of Plasmas **6**, 947–953 (1999).
- ¹¹⁹S. Gordienko and A. Pukhov, “Scalings for ultrarelativistic laser plasmas and quasi-monoenergetic electrons”, Physics of Plasmas **12**, 043109 (2005).
- ¹²⁰C. Wang, T. Lin, R. Caflisch, B. I. Cohen, and A. M. Dimits, “Particle simulation of Coulomb collisions: Comparing the methods of Takizuka & Abe and Nanbu”, Journal of Computational Physics **227**, 4308–4329 (2008).
- ¹²¹F. Peano, M. Marti, L. O. Silva, and G. Coppa, “Statistical kinetic treatment of relativistic binary collisions”, Physical Review E **79**, 025701 (2009).
- ¹²²D. P. Higginson, “A full-angle Monte-Carlo scattering technique including cumulative and single-event Rutherford scattering in plasmas”, Journal of Computational Physics **349**, 589–603 (2017).
- ¹²³F. Fiúza, M. Marti, R. A. Fonseca, L. O. Silva, J. Tonge, J. May, and W. B. Mori, “Efficient modeling of laser–plasma interactions in high energy density scenarios”, Plasma Physics and Controlled Fusion **53**, 074004 (2011).
- ¹²⁴J. Derouillat, A. Beck, F. Pérez, T. Vinci, M. Chiaramello, A. Grassi, M. Flé, G. Bouchard, I. Plotnikov, N. Aunai, J. Dargent, C. Riconda, and M. Grech, “Smilei : A collaborative, open-source, multi-purpose particle-in-cell code for plasma simulation”, Computer Physics Communications **222**, 351–373 (2018).
- ¹²⁵T. G. Blackburn, A. A. Gonoskov, and M. Marklund, “Relativistically intense XUV radiation from laser-illuminated near-critical plasmas”, Physical Review A **98**, 023421 (2018).
- ¹²⁶M. R. Edwards and P. Michel, “Plasma transmission gratings for compression of high-intensity laser pulses”, Physical Review Applied **18**, 024026 (2022).
- ¹²⁷Y. Suzuki and A. Takeuchi, “X-ray microfocusing by combination of grazing-incidence spherical-concave mirrors”, Japanese Journal of Applied Physics **49**, 106701 (2010).
- ¹²⁸M. R. Edwards, N. M. Fasano, T. Bennett, A. Griffith, N. Turley, B. M. O’Brien, and J. M. Mikhailova, “A multi-terawatt two-color beam for high-power field-controlled nonlinear optics”, Optics Letters **45**, 6542–6545 (2020).
- ¹²⁹S. Akturk, M. Kimmel, P. O’Shea, and R. Trebino, “Extremely simple device for measuring 20-fs pulses”, Optics Letters **29**, 1025–1027 (2004).
- ¹³⁰R. Trebino, *Frequency-resolved optical gating: the measurement of ultrashort laser pulses: the measurement of ultrashort laser pulses* (2000).
- ¹³¹S. Akturk, M. Kimmel, P. O’Shea, and R. Trebino, “Measuring pulse-front tilt in ultrashort pulses using grenouille”, Optics Express **11**, 491–501 (2003).
- ¹³²S. Akturk, M. Kimmel, P. O’Shea, and R. Trebino, “Measuring spatial chirp in ultrashort pulses using single-shot frequency-resolved optical gating”, Optics Express **11**, 68–78 (2003).
- ¹³³A. Borot, A. Malvache, X. Chen, D. Douillet, G. Iaquaniello, T. Lefrou, P. Audebert, J.-P. Geindre, G. Mourou, F. Quéré, and R. Lopez-Martens, “High-harmonic generation from plasma mirrors at kilohertz repetition rate”, Optics Letters **36**, 1461–1463 (2011).

- ¹³⁴J. Yang, M. Guehr, T. Vecchione, M. S. Robinson, R. Li, N. Hartmann, X. Shen, R. Coffee, J. Corbett, A. Fry, et al., “Diffractive imaging of a rotational wavepacket in nitrogen molecules with femtosecond megaelectronvolt electron pulses”, *Nature communications* **7**, 1–9 (2016).
- ¹³⁵M. Durand, A. Jarnac, Y. Liu, B. Prade, A. Houard, V. Tikhonchuk, and A. Mysyrowicz, “Dynamics of plasma gratings in atomic and molecular gases”, *Physical Review E* **86**, 036405 (2012).
- ¹³⁶S. Mirzanejad and M. Salehi, “Two-color high-order-harmonic generation: Relativistic mirror effects and attosecond pulses”, *Physical Review A* **87**, 063815 (2013).
- ¹³⁷S. Tietze, M. Zepf, S. G. Rykov, and M. Yeung, “Propagation effects in multipass high harmonic generation from plasma surfaces”, *New Journal of Physics* **22**, 093048 (2020).
- ¹³⁸P. Heissler, E. Lugovoy, R. Hörlein, L. Waldecker, J. Wenz, M. Heigoldt, K. Khrennikov, S. Karsch, F. Krausz, B. Abel, and G. D. Tsakiris, “Using the third state of matter: high harmonic generation from liquid targets”, *New Journal of Physics* **16**, 113045 (2014).
- ¹³⁹B. Dromey, C. Bellei, D. C. Carroll, R. J. Clarke, J. S. Green, S. Kar, S. Kneip, K. Markey, S. R. Nagel, L. Willingale, P. McKenna, D. Neely, Z. Najmudin, K. Krushelnick, P. A. Norreys, and M. Zepf, “Third harmonic order imaging as a focal spot diagnostic for high intensity laser-solid interactions”, *Laser and Particle Beams* **27**, 243–248 (2009).
- ¹⁴⁰V. V. Kulagin, V. A. Cherepenin, M. S. Hur, and H. Suk, “Theoretical Investigation of Controlled Generation of a Dense Attosecond Relativistic Electron Bunch from the Interaction of an Ultrashort Laser Pulse with a Nanofilm”, *Physical Review Letters* **99**, 124801 (2007).
- ¹⁴¹D. Kiefer, A. Henig, D. Jung, D. C. Gautier, K. A. Flippo, S. A. Gaillard, S. Letzring, R. P. Johnson, R. C. Shah, T. Shimada, J. C. Fernández, V. K. Liechtenstein, J. Schreiber, B. M. Hegelich, and D. Habs, “First observation of quasi-monoenergetic electron bunches driven out of ultra-thin diamond-like carbon (DLC) foils”, *The European Physical Journal D* **55**, 427–432 (2009).
- ¹⁴²T. Kluge, M. Bussmann, S. A. Gaillard, K. A. Flippo, D. C. Gautier, B. Gall, T. Lockard, M. E. Lowenstern, J. E. Mucino, Y. Sentoku, K. Zeil, S. D. Kraft, U. Schramm, T. E. Cowan, and R. Sauvrebrey, “Low-Divergent, Energetic Electron Beams from Ultra-Thin Foils”, *AIP Conference Proceedings* **1209**, 51–54 (2010).
- ¹⁴³J. Braenzel, A. A. Andreev, K. Y. Platonov, L. Ehrentraut, and M. Schnürer, “Amplification of coherent synchrotron high harmonic emission from ultra-thin foils in relativistic light fields”, *Physics of Plasmas* **24**, 080704 (2017).
- ¹⁴⁴D. Neely, P. Foster, A. Robinson, F. Lindau, O. Lundh, A. Persson, C.-G. Wahlström, and P. McKenna, “Enhanced proton beams from ultrathin targets driven by high contrast laser pulses”, *Applied Physics Letters* **89**, 021502 (2006).
- ¹⁴⁵T. Ceccotti, A. Lévy, H. Popescu, F. Réau, P. D’Oliveira, P. Monot, J. P. Geindre, E. Lefebvre, and P. Martin, “Proton Acceleration with High-Intensity Ultrahigh-Contrast Laser Pulses”, *Physical Review Letters* **99**, 185002 (2007).
- ¹⁴⁶A. Macchi, S. Veghini, and F. Pegoraro, ““Light Sail” Acceleration Reexamined”, *Physical Review Letters* **103**, 085003 (2009).

- ¹⁴⁷L. Yin, B. J. Albright, K. J. Bowers, D. Jung, J. C. Fernández, and B. M. Hegelich, “Three-Dimensional Dynamics of Breakout Afterburner Ion Acceleration Using High-Contrast Short-Pulse Laser and Nanoscale Targets”, *Physical Review Letters* **107**, 045003 (2011).
- ¹⁴⁸B. M. Hegelich, I. Pomerantz, L. Yin, H. C. Wu, D. Jung, B. J. Albright, D. C. Gautier, S. Letzring, S. Palaniyappan, R. Shah, K. Allinger, R. Hörlein, J. Schreiber, D. Habs, J. Blakeney, G. Dyer, L. Fuller, E. Gaul, E. Mccary, A. R. Meadows, C. Wang, T. Ditmire, and J. C. Fernandez, “Laser-driven ion acceleration from relativistically transparent nanotargets”, *New Journal of Physics* **15**, 085015 (2013).
- ¹⁴⁹F. Wagner, “Maximum Proton Energy above 85 MeV from the Relativistic Interaction of Laser Pulses with Micrometer Thick ch2 targets”, *Physical Review Letters* **116** (2016).
- ¹⁵⁰A. Higginson, R. J. Gray, M. King, R. J. Dance, S. D. R. Williamson, N. M. H. Butler, R. Wilson, R. Capdessus, C. Armstrong, J. S. Green, S. J. Hawkes, P. Martin, W. Q. Wei, S. R. Mirfayzi, X. H. Yuan, S. Kar, M. Borghesi, R. J. Clarke, D. Neely, and P. McKenna, “Near-100 MeV protons via a laser-driven transparency-enhanced hybrid acceleration scheme”, *Nature Communications* **9**, 1–9 (2018).
- ¹⁵¹V. Kaymak, E. Aktan, M. Cerchez, B. Elkin, M. Papenheim, R. Prasad, A. Pukhov, H.-C. Scheer, A.-M. Schroer, O. Willi, and B. Aurand, “Boosted acceleration of protons by tailored ultra-thin foil targets”, *Scientific Reports* **9**, 1–10 (2019).
- ¹⁵²C. Scullion, “Polarization Dependence of Bulk Ion Acceleration from Ultrathin Foils Irradiated by High-Intensity Ultrashort Laser Pulses”, *Physical Review Letters* **119** (2017).
- ¹⁵³M. J. Duff, R. Wilson, M. King, B. Gonzalez-Izquierdo, A. Higginson, S. D. R. Williamson, Z. E. Davidson, R. Capdessus, N. Booth, S. Hawkes, D. Neely, R. J. Gray, and P. McKenna, “High order mode structure of intense light fields generated via a laser-driven relativistic plasma aperture”, *Scientific Reports* **10**, 105 (2020).
- ¹⁵⁴Y. M. Mikhailova, V. T. Platonenko, and S. G. Rykovanov, “Generation of an attosecond X-ray pulse in a thin film irradiated by an ultrashort ultrarelativistic laser pulse”, *Journal of Experimental and Theoretical Physics Letters* **81**, 571–574 (2005).
- ¹⁵⁵A. S. Pirozhkov, S. V. Bulanov, T. Z. Esirkepov, M. Mori, A. Sagisaka, and H. Daido, “Attosecond pulse generation in the relativistic regime of the laser-foil interaction: The sliding mirror model”, *Physics of Plasmas* **13**, 013107 (2006).
- ¹⁵⁶A. S. Pirozhkov, S. V. Bulanov, T. Z. Esirkepov, M. Mori, A. Sagisaka, and H. Daido, “Generation of high-energy attosecond pulses by the relativistic-irradiance short laser pulse interacting with a thin foil”, *Physics Letters A* **349**, 256–263 (2006).
- ¹⁵⁷K. Krushelnick, W. Rozmus, U. Wagner, F. N. Beg, S. G. Bochkarev, E. L. Clark, A. E. Dangor, R. G. Evans, A. Gopal, H. Habara, S. P. D. Mangles, P. A. Norreys, A. P. L. Robinson, M. Tatarakis, M. S. Wei, and M. Zepf, “Effect of Relativistic Plasma on Extreme-Ultraviolet Harmonic Emission from Intense Laser-Matter Interactions”, *Physical Review Letters* **100**, 125005 (2008).
- ¹⁵⁸H. George, F. Quéré, C. Thaury, G. Bonnaud, and P. Martin, “Mechanisms of forward laser harmonic emission from thin overdense plasmas”, *New Journal of Physics* **11**, 113028 (2009).

- ¹⁵⁹S. Palaniyappan, B. M. Hegelich, H.-C. Wu, D. Jung, D. C. Gautier, L. Yin, B. J. Albright, R. P. Johnson, T. Shimada, S. Letzring, D. T. Offermann, J. Ren, C. Huang, R. Hörlein, B. Dromey, J. C. Fernandez, and R. C. Shah, “Dynamics of relativistic transparency and optical shuttering in expanding overdense plasmas”, *Nature Physics* **8**, 763–769 (2012).
- ¹⁶⁰H.-C. Wu and J. Meyer-ter-Vehn, “Giant half-cycle attosecond pulses”, *Nature Photonics* **6**, 304–307 (2012).
- ¹⁶¹H.-C. Wu, J. Meyer-ter-Vehn, J. Fernández, and B. M. Hegelich, “Uniform Laser-Driven Relativistic Electron Layer for Coherent Thomson Scattering”, *Physical Review Letters* **104**, 234801 (2010).
- ¹⁶²V. A. Vshivkov, N. M. Naumova, F. Pegoraro, and S. V. Bulanov, “Nonlinear electrodynamics of the interaction of ultra-intense laser pulses with a thin foil”, *Physics of Plasmas* **5**, 2727–2741 (1998).
- ¹⁶³V. L. Bratman and S. V. Samsonov, “Radiation and radiative damping of a charged plane, oscillating with a relativistic velocity”, *Physics Letters A* **206**, 377–382 (1995).
- ¹⁶⁴R. A. Beth, “Mechanical Detection and Measurement of the Angular Momentum of Light”, *Physical Review* **50**, 115–125 (1936).
- ¹⁶⁵L. Allen, M. W. Beijersbergen, R. J. C. Spreeuw, and J. P. Woerdman, “Orbital angular momentum of light and the transformation of Laguerre-Gaussian laser modes”, *Physical Review A* **45**, 8185–8189 (1992).
- ¹⁶⁶A. E. Willner, H. Huang, Y. Yan, Y. Ren, N. Ahmed, G. Xie, C. Bao, L. Li, Y. Cao, Z. Zhao, J. Wang, M. P. J. Lavery, M. Tur, S. Ramachandran, A. F. Molisch, N. Ashrafi, and S. Ashrafi, “Optical communications using orbital angular momentum beams”, *EN, Advances in Optics and Photonics* **7**, 66–106 (2015).
- ¹⁶⁷J. Wang, J.-Y. Yang, I. M. Fazal, N. Ahmed, Y. Yan, H. Huang, Y. Ren, Y. Yue, S. Dolinar, M. Tur, and A. E. Willner, “Terabit free-space data transmission employing orbital angular momentum multiplexing”, *en, Nature Photonics* **6**, 488–496 (2012).
- ¹⁶⁸M. Padgett and R. Bowman, “Tweezers with a twist”, *en, Nature Photonics* **5**, 343–348 (2011).
- ¹⁶⁹C. Maurer, A. Jesacher, S. Bernet, and M. Ritsch-Marte, “What spatial light modulators can do for optical microscopy”, *en, Laser & Photonics Reviews* **5**, 81–101 (2011).
- ¹⁷⁰J. W. Wang, M. Zepf, and S. G. Rykovanov, “Intense attosecond pulses carrying orbital angular momentum using laser plasma interactions”, *Nature Communications* **10**, 5554 (2019).
- ¹⁷¹L. Yi, “High-Harmonic Generation and Spin-Orbit Interaction of Light in a Relativistic Oscillating Window”, *Physical Review Letters* **126**, 134801 (2021).
- ¹⁷²A. Borot, A. Malvache, X. Chen, A. Jullien, J.-P. Geindre, P. Audebert, G. Mourou, F. Quéré, and R. Lopez-Martens, “Attosecond control of collective electron motion in plasmas”, *Nature Physics* **8**, 416–421 (2012).
- ¹⁷³M. Behmke, D. an der Brügge, C. Rödel, M. Cerchez, D. Hemmers, M. Heyer, O. Jäckel, M. Kübel, G. G. Paulus, G. Pretzler, A. Pukhov, M. Toncian, T. Toncian, and O. Willi, “Controlling the Spacing of Attosecond Pulse Trains from Relativistic Surface Plasmas”, *Physical Review Letters* **106**, 185002 (2011).

- ¹⁷⁴P. Heissler, R. Hörlein, M. Stafe, J. M. Mikhailova, Y. Nomura, D. Herrmann, R. Tautz, S. G. Rykovanov, I. B. Földes, K. Varjú, F. Tavella, A. Marcinkevicius, F. Krausz, L. Veisz, and G. D. Tsakiris, “Toward single attosecond pulses using harmonic emission from solid-density plasmas”, *Applied Physics B* **101**, 511–521 (2010).
- ¹⁷⁵A. Gonoskov, E. Wallin, A. Polovinkin, and I. Meyerov, “Employing machine learning for theory validation and identification of experimental conditions in laser-plasma physics”, *Scientific Reports* **9**, 1–15 (2019).
- ¹⁷⁶Z.-Y. Chen and A. Pukhov, “Bright high-order harmonic generation with controllable polarization from a relativistic plasma mirror”, *Nature Communications* **7**, 12515 (2016).
- ¹⁷⁷J. Wang, S. V. Bulanov, M. Chen, B. Lei, Y. Zhang, R. Zagidullin, V. Zorina, W. Yu, Y. Leng, R. Li, M. Zepf, and S. G. Rykovanov, “Relativistic slingshot: A source for single circularly polarized attosecond x-ray pulses”, *Physical Review E* **102**, 061201 (2020).
- ¹⁷⁸G. Ma, W. Yu, M. Y. Yu, B. Shen, and L. Veisz, “Intense circularly polarized attosecond pulse generation from relativistic laser plasmas using few-cycle laser pulses”, *Optics Express* **24**, 10057–10065 (2016).
- ¹⁷⁹M. Blanco, M. T. Flores-Arias, and A. Gonoskov, “Controlling the ellipticity of attosecond pulses produced by laser irradiation of overdense plasmas”, *Physics of Plasmas* **25**, 093114 (2018).
- ¹⁸⁰H. Vincenti and F. Quéré, “Attosecond Lighthouses: How To Use Spatiotemporally Coupled Light Fields To Generate Isolated Attosecond Pulses”, *Physical Review Letters* **108**, 113904 (2012).
- ¹⁸¹J. A. Wheeler, A. Borot, S. Monchocé, H. Vincenti, A. Ricci, A. Malvache, R. Lopez-Martens, and F. Quéré, “Attosecond lighthouses from plasma mirrors”, *Nature Photonics* **6**, 829–833 (2012).
- ¹⁸²Y. Jiang, Q. Wang, L. Cao, Z. Liu, C. Zheng, X. He, Y. Chao, and R. Xie, “Enhancement of brightness of high-order harmonics with elliptical polarization from near-critical density plasmas irradiated by an ultraintense laser pulse”, *Physics of Plasmas* **27**, 083101 (2020).
- ¹⁸³D. Xie, Y. Yin, T. Yu, H. Zhou, Z. Chen, and H. Zhup, “High harmonic generation driven by two-color relativistic circularly polarized laser pulses at various frequency ratios”, *Plasma Science and Technology* **23**, 045502 (2021).
- ¹⁸⁴C. L. Zhong, Y. Zhang, X. B. Li, J. Wang, C. T. Zhou, S. P. Zhu, X. T. He, and B. Qiao, “Emissions of brilliant attosecond pulse in circular polarization by using inclined lasers”, *Physics of Plasmas* **28**, 093105 (2021).
- ¹⁸⁵C. L. Zhong, B. Qiao, X. R. Xu, Y. X. Zhang, X. B. Li, Y. Zhang, C. T. Zhou, S. P. Zhu, and X. T. He, “Intense circularly polarized attosecond pulse generation from solid targets irradiated with a two-color linearly polarized laser”, *Physical Review A* **101**, 053814 (2020).
- ¹⁸⁶C. Zhong, B. Qiao, Y. Zhang, Y. Zhang, X. Li, J. Wang, C. Zhou, S. Zhu, and X. He, “Production of intense isolated attosecond pulses with circular polarization by using counter-propagating relativistic lasers”, *New Journal of Physics* **23**, 063080 (2021).

- ¹⁸⁷Q. Li, X. Xu, X. Xu, Y. Wu, Y. Yin, D. Zou, T. Yu, and T. Yu, “Efficient high-order harmonics generation from overdense plasma irradiated by a two-color co-rotating circularly polarized laser pulse”, *Optics Express* **30**, 15470–15481 (2022).
- ¹⁸⁸M. Born and E. Wolf, *Principles of Optics: Electromagnetic Theory of Propagation, Interference and Diffraction of Light* (Cambridge University Press, Oct. 1999).
- ¹⁸⁹Z. M. Chitgar, R. Adam, C. Greb, A. Lehrach, M. Büscher, and P. Gibbon, “Theory of circularly polarized harmonic generation using bi-colour lasers in underdense plasmas”, *Plasma Physics and Controlled Fusion* **63**, 035023 (2021).
- ¹⁹⁰D. Jang, R. M. Schwartz, D. Woodbury, J. Griff-McMahon, A. H. Younis, H. M. Milchberg, and K.-Y. Kim, “Efficient terahertz and Brunel harmonic generation from air plasma via mid-infrared coherent control”, *Optica* **6**, 1338–1341 (2019).
- ¹⁹¹I. H. Malitson, “Interspecimen Comparison of the Refractive Index of Fused Silica^{*,†}”, *JOSA* **55**, 1205–1209 (1965).

Appendix A

List of Abbreviations

| Abbreviation | Description |
|--------------|--------------------------------|
| AOM | Acousto-Optic Modulator |
| C | Collisions |
| CCD | Charge Coupled Device |
| CEP | Carrier Envelope Phase |
| CP | Circular Polarization |
| CPA | Chirped Pulse Amplification |
| CSE | Coherent Synchrotron Emission |
| CWE | Coherent Wake Emission |
| deg | degree |
| FF | Far Field |
| FWHM | Full Width Half Maximum |
| GDD | Group Delay Dispersion |
| GVD | Group Velocity Dispersion |
| HG | Hermite-Gauss |
| HHG | High-Order harmonic generation |
| inc | incident |
| IR | Infrared |
| LG | Laguerre-Gauss |
| LP | Linear Polarization |
| NC | No Collisions |
| nD | n-Dimensional |
| NF | Near field |
| Norm | Normalized |
| OAM | Orbital Angular Momentum |
| OAP | Off-Axis-Parabola |
| OMM | Oscillating Mirror Model |
| PIC | Particle-In-Cell |
| PM | Plasma Mirror |

| Abbreviation | Description |
|---------------------|---------------------------------------|
| ref | reflected |
| ROM | Relativistic Oscillating Mirror |
| RHHG | Relativistic High Harmonic Generation |
| SAM | Spin Angular Momentum |
| SM | Spherical Mirror |
| UV | Ultraviolet |
| XUV | Extreme Ultraviolet |

Appendix B

List of Symbols

| Symbol | Description |
|--|---|
| \vec{a} | Acceleration |
| \vec{A} | Vector potential |
| a_0 | Normalized vector potential |
| Ai' | Derivative of the Airy function of the first kind |
| c | Speed of light in vacuum |
| C | Courant-Friedrichs-Lowy number |
| d | Plasma thickness in real units |
| D | Plasma thickness normalized to the laser's central wavelength |
| δ_b | Electron bunch width |
| δ_h | Harmonic full-width-half-maximum |
| Δt | Simulation time step size |
| $\Delta x, \Delta y, \Delta z$ | Simulation cell size in the x, y, and z directions, respectively |
| ΔY_{12} | Spatial walk-off |
| e | Electron's charge |
| \vec{E} | Electric field |
| E_a | Attosecond pulse electric field |
| $\eta_{atto}^{[\omega_{LF}, \omega_{UF}]}$ | Maximum attosecond pulse intensity normalized to the incident laser intensity where the attosecond pulse is formed using frequencies in the range $\omega_{LF} < \omega/\omega_L < \omega_{UF}$ |
| E_L | Peak electric field strength of the incident laser |
| E_p | P-polarized component of the electric field |
| $\eta_{spec}^{[\omega_{LF}, \omega_{UF}]}$ | Spectral energy in the range $\omega_{LF} < \omega/\omega_L < \omega_{UF}$ |
| E_s | S-polarized component of the electric field |
| $\tilde{f}(\omega)$ | Electron bunch shape factor |
| f | Focal length |
| γ | Relativistic Lorentz factor |
| h | Planck's constant |
| \hbar | Reduced Planck's constant |
| I | Intensity |
| I_a | Attosecond pulse intensity |
| I_L | Peak intensity of the laser |
| $I(\omega)$ | Spectral intensity |
| I_p | Intensity of the p-polarized component of the laser |
| I_s | Intensity of the s-polarized component of the laser |

| Symbol | Description |
|--------------------------------|--|
| \vec{J} | Current density |
| k | Wave number |
| k_b | Boltzmann constant |
| KE | Kinetic Energy |
| k_L | Laser's wave number |
| L | Pre-plasma scale length |
| λ_L | Laser's central wavelength |
| Λ | Coulomb logarithm |
| L_l^q | Laguerre-Gauss modes where l is the azimuthal index and q is the radial index |
| m_e | Electron's rest mass |
| μ_0 | Vacuum magnetic permeability |
| N | Electron density normalized to the plasma critical density |
| n | index of refraction |
| n_c | Electron critical density |
| n_e | Electron number density in real units |
| N_e | Spatial distribution of the electron number density |
| n_i | Ion number density |
| N_0 | Electron density normalized to the plasma critical density |
| $n\omega = \omega_n$ | n^{th} n^{th} harmonic order of the driving laser |
| N_{peak} | Peak value of the electron number density |
| ν_{ei} | Electron-ion collision frequency |
| ϕ_1 | Phase of the fundamental beam |
| ϕ_2 | Phase of the second harmonic beam |
| ϕ_{12} | Relative phase between the 1ω and 2ω beams |
| ϕ_{CEP} | Carrier envelope phase |
| ϕ_{sp} | Phase difference between the s and p polarized components |
| ρ | Charge density distribution |
| p | Exponent of the spectral power-law |
| $\text{particles}/\text{cell}$ | Number of particles per cell at the start of the simulation |
| $S = N/a_o$ | Normalized relativistic similarity parameter |
| σ | Surface charge density |
| t | Time coordinate |
| τ_{FWHM} | Full-width-half maximum of the driving laser |
| t_a | Advanced time frame coordinate |
| $T_{Emission}$ | Time when the attosecond pulse is emitted |
| θ | Laser angle of incidence |
| T_L | Laser period |
| $T_{MaxDisp}$ | Time when the electron bunch has its maximum displacement from the initial plasma-vacuum interface |
| U | Particle energy |
| $U_{n\omega}$ | Energy of the n^{th} harmonic order |
| \vec{V} | Velocity |
| W_o | Laser spot size |
| ω | Angular frequency coordinate |
| ω_b | Spectral cut-off predicted by the electron bunch shape factor |

| Symbol | Description |
|------------------------|--|
| ω_γ | Spectral cut-off predicted by the peak value of the emitting electron's Lorentz factor |
| ω_L | Laser's central frequency |
| $\omega_n = n\omega_L$ | n^{th} harmonic order of the driving laser |
| ω_p | Plasma frequency |
| \vec{X} | Displacement |
| x, y, z | Spatial coordinates in the laboratory frame |
| x', y', z' | Spatial coordinates in the simulation (Bourdier) frame |
| x_1, y_1, z_1 | Spatial coordinates along the direction of specular reflection |

Appendix C

Coordinate Frames Used in Simulations

In this appendix we discuss the three different coordinate axes used for all simulations throughout this text and how to transform between the different frames of reference. The three different coordinate axes are summarized in figure C.1. In the laboratory frame [figure C.1(a)], the laser is obliquely incident on a stationary plasma. The angle of incidence is determined by the angle between the x-axis and the laser's wavevector. The $x - y$ plane defines the plane of incidence, where the plasma's normal vector points along the negative x-direction.

Through a Lorentz transformation to the x' - y' plane, which is defined by an observer who is traveling at a velocity of $c \sin(\theta)$ in y-direction with respect to the x-y laboratory frame, this problem can be recast as one in which the laser is normally incident on a streaming plasma [figure C.1(b)]. A detailed discussion of how to convert all variables between the x' - y' and x-y frame is given in reference [118]. By doing this transformation, we have effectively reduced a two-dimensional problem to just one-dimension, so oblique incidence interactions can be treated in the same way as normal incidence interactions. This transformation is common for theory calculations [43, 44] and particle-in-cell simulations [38]. It allows for huge computational savings as two-dimensional simulations require enormous computational resources, which often limits their applicability to low-

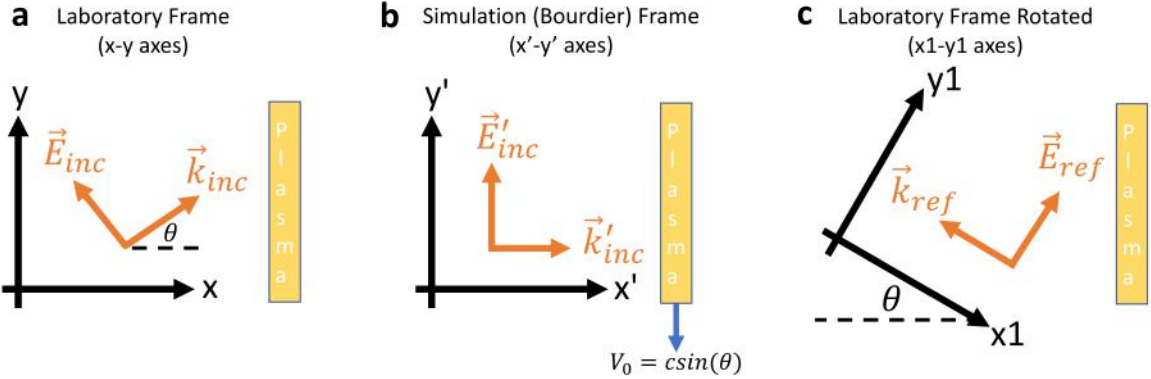


Figure C.1: Common coordinate systems used throughout this thesis to model laser–solid interactions. (a) Laboratory frame: The laser is obliquely incident at an angle θ onto a stationary plasma. (b) Simulation (Bourdier [117]) Frame: The laser is normally incident onto a plasma which streams in the $-y$ direction at a speed of $V_0 = c \sin(\theta)$. (c) Rotated Laboratory frame: Same as (a) except the coordinate axis has been rotated by an angle θ so that $x1$ is parallel to the direction of specular reflection.

order harmonics and course parameter scans. Note that in a one-dimensional particle-in-cell simulation, only one spatial dimension is modeled but all three velocity and field components are retained, allowing for the plasma to stream in the y -direction. Working in a one-dimensional does restrict the physics of the problem to modeling only specular direction reflections, so any spurious reflections will not be captured by our simulations. Furthermore, a one-dimensional simulation assumes that the interaction is infinite in the transverse directions, which means effects of finite spot-sizes will be ignored.

After reflection from the plasma surface, the laser propagates in the specular direction in the laboratory frame. In some instances, it is useful to plot the particle dynamics or electric and magnetic fields in a coordinate frame which is parallel and perpendicular to the direction of specular direction [figure C.1(c)]. For example, at the time of attosecond pulse emission, the electron’s velocity is entirely along the $x1$ axis and the electron’s acceleration is entirely along the $y1$ axis. Transformation of any vector, \vec{V} , from the $x - y$ to the $x1 - y1$ is done with the following equations:

$$V_{x1} = V_x \cos \theta - V_y \sin \theta \quad (\text{C.1})$$

$$V_{y1} = V_x \sin \theta + V_y \cos \theta \quad (\text{C.2})$$

$$V_{z1} = V_z \quad (\text{C.3})$$

Appendix D

Dispersion Calculations for a Two-Color Laser Propagating Through Glass

In this appendix we discuss the changes to a two-color laser's waveform and spatial overlap after propagating through a dispersive element (e.g. a piece of glass). The equations derived here were used to estimate the phase difference between the two colors of the laser used for experiments in chapter 4.

The equations for relative phase delay ($\Delta\phi_{12}$), relative group delay ($\Delta\tau_{12}$), and spatial walk-off (Δy_{12}) between the two-colors are expressed in equations D.1 through D.3, respectively. The equation for pulse broadening is also given by equation D.4. These relations were derived using the geometry presented in Fig. D.1, which was adapted from reference [190]. In equation D.2, $n' = dn/d\lambda$ and the relation between group velocity and index of refraction was used ($v_g = c / (n - \lambda \frac{dn}{d\lambda})$). In equation D.4, GVD is the group velocity dispersion term calculated from the index of refraction and L is the propagation distance of the light inside the wafer.

In figure D.2, the relative phase delay [D.2(a)] and relative group delay [D.2(b)] is plotted as a function of the wafer angle. The calculation assumes a wafer thickness of $100\mu m$ thick and that the wafer is composed of fused silica, for which the index of

refraction as a function of wavelength can be found from reference [191]. For a $100\mu m$ thick fused silica wafer at a 25° angle of incidence (the conditions used in the experiments of chapter 4), $\Delta\phi_{12} = -135^\circ$, $\Delta\tau_{12} = 16\text{fs}$, $\Delta y_{12} = 0.35\mu m$, and the pulse broadening is less than 0.1fs .

$$\Delta\phi_{12} = 2\phi_{1\omega} - \phi_{2\omega} = 2\pi t \left[\frac{2n_{1\omega}}{\lambda_{1\omega}\cos(\theta_{1\omega})} - \frac{n_{2\omega}}{\lambda_{2\omega}\cos(\theta_{2\omega})} - \frac{\sin(\theta) (\tan(\theta_{1\omega}) - \tan(\theta_{2\omega}))}{\lambda_{2\omega}} \right] \quad (\text{D.1})$$

$$\Delta\tau_{12} = \tau_{2\omega} - \tau_{1\omega} = \frac{t}{c} \left[\frac{n_{2\omega} - \lambda_{2\omega}n'_{2\omega}}{\cos(\theta_{2\omega})} + \sin(\theta) (\tan(\theta_{1\omega}) - \tan(\theta_{2\omega})) - \frac{n_{1\omega} - \lambda_{1\omega}n'_{1\omega}}{\cos(\theta_{1\omega})} \right] \quad (\text{D.2})$$

$$\Delta y_{12} = y_{2\omega} - y_{1\omega} = t\cos(\theta) (\tan(\theta_{1\omega}) - \tan(\theta_{2\omega})) \quad (\text{D.3})$$

$$\frac{\tau_{out}}{\tau_{inc}} = \sqrt{1 + \left(\frac{4\ln(2)GVDL}{\tau_{inc}^2} \right)^2} \quad (\text{D.4})$$

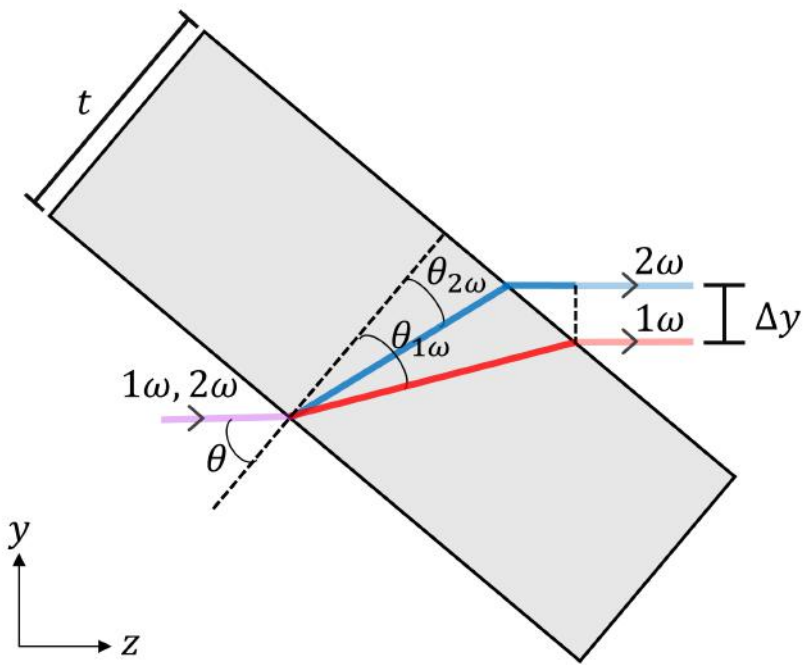


Figure D.1: Geometry of the fused silica wafer used to control the waveform of the two-color laser after PM2. t is the wafer thickness. θ is the laser angle of incidence. θ_1 and θ_2 are the refraction angle given by Snell's law for the fundamental (1ω) and second harmonic (2ω) beams, respectively. Δy is the spatial walk-off between the two colors after propagating through the wafer. This image was adapted from the supplementary material of reference [190].

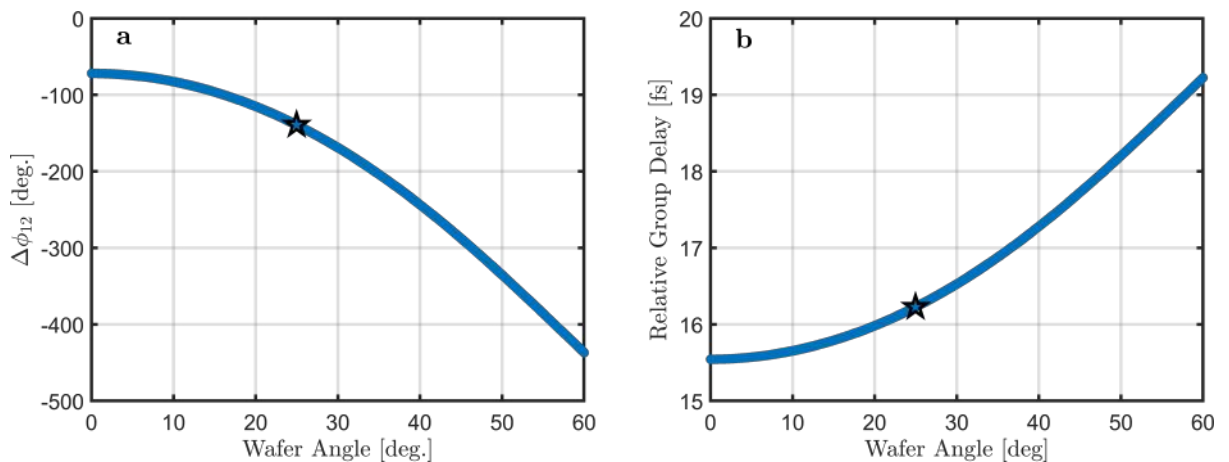


Figure D.2: (a) Calculated relative phase delay and (b) relative group delay between the fundamental and second harmonic as a function of the wafer angle. The star marks the angle of the wafer when the two-color interactions enhanced the reflected third and fourth harmonic energy (25°). The calculations used a thickness of $t = 100\mu m$.